DISCUSSION OF INDUCTION MOTOR EFFECT ON ROTORDYNAMICS

A Dissertation

by

XU HAN

Submitted to the Office of Graduate and Professional Studies of
Texas A&M University
in partial fulfillment of the requirements for the degree of

DOCTOR OF PHILOSOPHY

Chair of Committee,	Alan Palazzolo
Committee Members,	Won-jong Kim
	Steve Suh
	Hamid Toliyat
Head of Department,	Andreas Polycarpou

May 2015

Major Subject: Mechanical Engineering

ABSTRACT

In this dissertation, the influence of using induction motor in machinery train on rotordynamics is discussed. Two areas are considered – the use of variable frequency drives (VFDs), which control and drive the induction motor; and the unstable forces due motor eccentricity, which is resulted from motor rotor lateral motion.

VFDs – The dissertation documents fatigue related mechanical failures in VFD motor machinery due to mechanical vibrations excited by drive torque harmonics which are created by PWM switching. Present effort models the coupled system with full electrical system including DC bus, inverter, motor, and an industrial mechanical system including flexible couplings, gearboxes and multiple inertias. The approach extends failure prediction beyond simple occurrence of resonance, to fatigue life evaluation based on Rain-flow algorithm, which is suitable for both steady state and transient startup mechanical response. The use of multilevel inverters is demonstrated having the possibility actually exacerbate resonance and fatigue failure. The model is also compared to an industrial test case, which provides good agreement.

Motor eccentricity – In this dissertation, a MEC modeling method is proposed to calculate both the radial and tangential motor eccentric force. The proposed model is also coupled with the motor electric circuit model to provide capability of transient simulation. FEM (Ansys Maxwell) is used to verify the proposed model. Parametric study is performed on the motor radial and tangential eccentric forces. Also a Jeffcott rotor model is used to study the influence of the motor eccentric force on mechanical

stability. A stability criteria of the bearing damping is calculated. The motor radial and tangential eccentric forces are all curved fitted to catch their nonlinearity, which are used in time domain simulation. Nonlinear motions are observed, including limit cycle and jumping phenomena.

The results of this dissertation show that both the use of VFDs and the motor lateral motion (motor eccentricity) can cause severe mechanical vibration problem in a rotating machinery train. Both of these two problems need to be carefully concerned in design stage.

DEDICATION

To my parents, my husband and my daughter.

To my Lord.

ACKNOWLEDGEMENTS

I would like to thank my committee chair, Dr. Palazzolo, and my committee members, Dr. Kim, Dr. Toliyat and Dr. Suh, for their guidance and support throughout the course of this research.

Thanks also go to my friends and colleagues and the department faculty and staff for making my time at Texas A&M University a great experience.

Finally, thanks to my mother and father for their support during my study and to my husband for his patience and love.

TABLE OF CONTENTS

Page

LIST OF FIGURES

Page

LIST OF TABLES

Page

CHAPTER I

INTRODUCTION*

1.1 Problem Statement

Nowadays, a lot of mechanical systems are driven by induction motors (asynchronous motors). For easy speed control in wide speed range and energy efficiency, most induction motors are controlled by Variable Frequency Drives (VFDs). However, the drives and induction motor itself can bring new stability problem to the driven mechanical systems, which are discussed below.

1.1.1 VFDs

VFDs are electrical drives using power electronics devices. The induction motor and its VFD compose the electrical drive system. Thus for a complete motion train, the electrical and mechanical systems are coupled together.

However, in practice, some mechanical trains driven by VFD-motor systems have encountered torsional vibration problem. Form the paper written by Feese (Engineering Dynamics Incorporated) and Maxfield (Tesoro Refining & Marketing Company) [1], these torsional vibration problems are identified as the result of using VFDs.

---

*Part of the data reported in this chapter is reprinted with permission from "VFD Machinery Vibration Fatigue Life and Multi-Level Inverter Effect" by Xu Han and Alan Palazzolo, 2013, *IEEE Transactions on Industry Application*, Volume 49, Issue 6, pp. 2562-2575, Copyright [2013] by IEEE.

VFDs introduce voltage/current harmonics in motor windings, which results in electromagnetic torque harmonics. The time varying motor driven torque brings torsional vibration to the mechanical system. When the motor torque harmonic frequency coincides with the natural frequency of the mechanical system, resonance may occur. Resonance causes large mechanical vibrations and put the mechanical components under excessive stress load, which may cause great damage, like failure of coupling or shaft. Fig. 1 and Fig. 2 show the damaged motor shaft and coupling due to VFD induced harmonics.

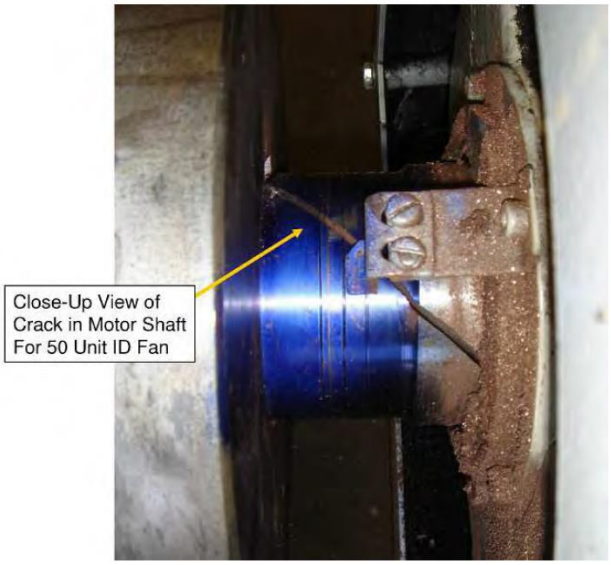

Fig. 1 Damaged motor shaft [1]

Fig. 2 Broken coupling [2]

1.1.2 Motor Eccentricity

In a motor-machinery train, the torsional vibration can be coupled with the lateral vibration, i.e. due to gear teeth flexibility. In this case, the motor rotor can also have lateral motion inside its stator. While the motor rotor is eccentric from the stator center (Fig. 3), a radial force and a tangential force are generated because of the electromagnetic interaction.

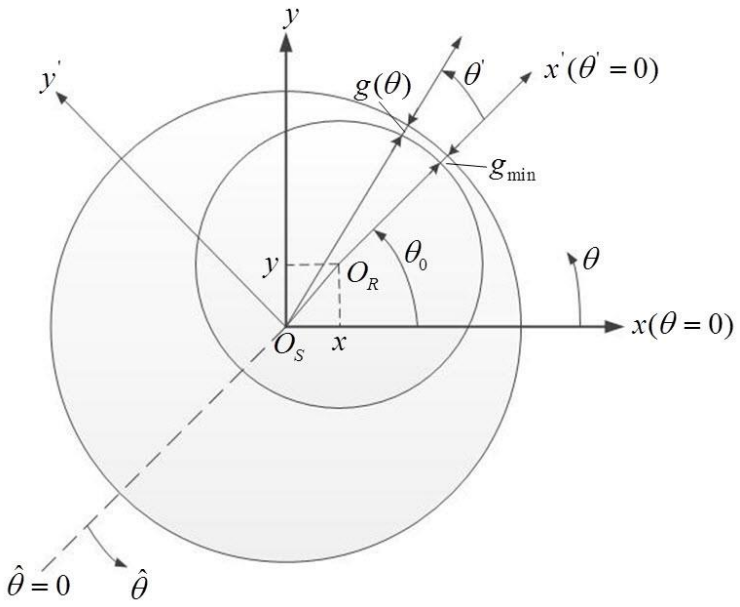

Fig. 3 Induction motor with rotor eccentricity

It is shown in [3] that the eccentricity caused air gap asymmetry could induce forces larger than the weight of the rotor by simulating two motors. In [4], a generator rotor eccentricity case was studied using finite element method (FEM). The author concluded that

"the stability of the rotor is affected significantly, as are the eigenfrequencies of the rotor".

Thus for a full motor-machinery train with coupled torsional and lateral vibrations, the magnetic force due to the rotor eccentricity should be considered and the effects should be analyzed.

1.2 Originality and Novelty

In traditional industry applications, electric drive-motor system and the mechanical system are designed separately. However, due to the complexity of these two systems, simple analysis of either electrical system or mechanical system alone is not enough to investigate the stability and reliability of the coupled system. The proposed modeling methods combine the two fields together and are capable for stability and failure analysis.

1.2.1 VFDs

Torsional vibration problem can bring great damage to mechanical components. The vibration can induce big stress on shafts and couplings, and reduce the lifetime of these mechanical parts. Far before the designed lifetime, the mechanical train may encounter failures. Avoiding torsional vibration is very import in mechanical system design. In a pure mechanical system, designer can design and set the rotational natural frequency of the mechanical train far away from the potential excitation frequency [5]. However, for system driven by VFD induction motor system, the excitation frequency, which is always the harmonic frequency of the electromagnetic torque, is difficult to tell. Since the modulated electrical signal contains lots of harmonics, and their magnitude and frequency depend on the control method. On the other hand, when varying the motor speed, the harmonic frequency of electromagnetic torque varies. For example, during start up, the coupled system may be excited by time varying harmonics.

Thus, due to the difficulty of determining the excitation frequency of electrical drives, designers are suggested to use estimated or experience values. For example, one can concern the harmonic frequency of electromagnetic torque as 6×, 12×, 18×… times the motor operating frequency with amplitude from manufacture [5]. This method does not take all the possible exciting harmonics into consideration. From this point, it is very important to model and simulate the entire coupled electrical and mechanical system at the same time.

However, a search of the literature did not reveal prior coupling of electrical and mechanical systems to analyze VFD machinery trains for torsional vibration modeling. In the proposed work, these two areas will be coupled together. A stand-alone code written with Matlab is developed with user-friendly Excel interface. The simulation of coupled system can help to identify the operation points where the train suffers torsional vibration. Avoiding these operation points can protect mechanical components.

1.2.2 Motor Eccentricity

Motors are important components in machinery drive train system. It converts the electrical power to mechanical power. Though motors always have stiff bearings, it can still have lateral motions, in which cases the rotors move away from the stator center. The asymmetry of the motor results in nonlinear lateral forces, both in radial direction and tangential direction. These forces tend to destabilize the mechanical system, because they are in the same direction as the eccentricity (negative stiffness).

It is very important to include the motor negative stiffness in machinery train design stage. However it is very different to get their values. Some studies use commercial finite element software (Ansys Maxwell) to model the motor and move the rotor position with different eccentricity, and calculate a stiffness value, which is used in machinery train analysis [4]. This is only able to calculate the static eccentric force. In practice, the motor rotor may have a complex whirling motion and the load may also be time varying. These all causes the eccentric force changing with time.

It is also important to count for the magnetic field distribution in the stator core area. The magnetic field distributed in stator core cannot be ignored since the forces are induced due to the magnetic field asymmetry in the motor air gap. A small change in the air gap flux density can result in big force changes. There are researches using simple motor model to get an analytical solution for the radial forces with ignoring the MMF drop in stator core. This results in overestimated eccentric force and overqualified bearing/shaft if used in mechanical design.

Also considering the two forces, the negative tangential stiffness is more dangerous. However, most research related to this is for synchronous motor only (especially for salient pole motor). Induction motors are always considered with radial force. However, even a small tangential force can make machinery train go unstable and get big damage.

The proposed model models the induction motor with equivalent magnetic circuit and can predict the negative stiffness for both radial direction and tangential direction. The influence of the eccentric forces on rotordynamics is studied via a Jeffcott rotor

model. Nonlinear behavior is observed. Also the proposed model is capable to be easily connected with complex mechanical system with coupled torsional-lateral motion and perform dynamic simulations with time varying load.

CHAPTER II

LITERATURE REVIEW*

2.1 VFDs

The literature on vibration control and life prediction in non-VFD torsional vibration machinery trains is quite extensive. For instance, the transitory, torsional resonance of a conventional drive, synchronous motor machinery train due to a dynamic torque at twice the slip frequency is discussed in [6-8]. VFD related torque harmonics and their causes have been analyzed in several references [9][10]. Reference [9] provides theoretical expressions for the torque harmonic frequencies as a function of the PWM switching frequency. Inverter control induced torque harmonics, including the first, second and six torque harmonics are analyzed in [10]. This reference also considers the dc component of phase current, asymmetric dead time voltage and magnetic saturation, which play important roles in generating torque harmonics.

Torsional machinery vibration problems related to the usage of VFD's were reported as early as the 1980's [11]. The case history in [1] verified the earlier predictions with actual test field operations measurements. This was followed by a series of papers documenting failures that occurred in industrial VFD machinery trains [2][12]-[16]. The measurements in [1] showed that incorporation of the VFD resulted in a

---

* Part of the data reported in this chapter is reprinted with permission from "VFD Machinery Vibration Fatigue Life and Multi-Level Inverter Effect" by Xu Han and Alan Palazzolo, 2013, *IEEE Transactions on Industry Application*, Volume 49, Issue 6, pp. 2562-2575, Copyright [2013] by IEEE.

significant increase in torsional vibration. Accurate prediction of the VFD related torque harmonics at the design stage was a formidable task, in part due to their dependence on power switch type, control law, measurement sensor, electrical and mechanical system interactions, etc. This caused a high uncertainty in reliability prior to actual operation of the machinery.

Some VFD related research shows that reduction of the total harmonic distortion (THD) is possible by implementing higher level inverter schemes [17][18]. Although this is true and also beneficial from the standpoint of reducing EMI and ohmic losses, it does not guarantee that all components of torque are reduced, and as shown by our example certain harmonics may actually increase as the inverter level increases and further exacerbate a high cycle fatigue problem. A recent publication [19] provides formulas for the torque harmonic frequencies and the relationships between torque and current harmonic frequencies, which are verified by both simulations and tests. Theses authors develop a particularly clever approach for eliminating entire series of torque harmonics by implementing a PWM carrier frequency interleaving on a four-thread VFD. A possible drawback to this approach is an increase in hardware cost and lower reliability. The example presented here demonstrates alternative approaches for mitigating the effects of a problematic torque harmonic by increasing the damping in the machinery couplings, or by changing the PWM switching frequency or the electrical frequency.

Although the above references provide excellent treatment for determination of VFD related dynamic torques they lack a means for predicting vibrations and life of a

complete machinery train that has significant coupling between its mechanical and electrical subsystems. This task is addressed by the present approach that includes a high fidelity total system model and analysis that extends from the three phase power input source of the DC bus to the torsional stresses and fatigue life of all mechanical components. This enables one to optimize the design of a torsional machinery system by selecting parameter values, from a parameter space which includes mechanical parameters such as moments of inertias, coupling stiffness, etc. and electrical parameters such as IGBT's, motor stator inductances and resistances, etc., in order to extend life. The prediction of life is based on a Rain-flow, stress cycle counting process that is applicable to transient phenomena such as startups, or steady state harmonic, near-resonance vibration.

2.2 Motor Eccentricity

The motor eccentricity problem has been studied by many researches. As early as in 1987, the radial eccentric force for two pole induction machines was calculated in [20] and the homopolar flux was investigated. In the calculation, the stator and rotor iron core were assumed to have infinite permeability, which resulted in magnetomotive force (MMF) drop only in the air gap. Also, the MMF along the air gap was assumed to be sinusoidally distributed, which meant only the fundamental component was considered. They wrote the non-linear air gap permeance in Fourier series expansion. Then the energy method was used to get the radial eccentric force. Similar assumptions and motor modeling method was used in [21] – [25]. In [21], an analytical solution was derived for

the radial eccentric force using Maxwell stress tensor and the author concluded that the radial force included a constant component and an oscillatory component. A Jeffcott rotor was modeled to analysis the effect of the radial eccentric force. A more accurate expression for the air gap length under eccentricity was derived in [22]. A generator was modeled with 153 beam elements to study the dynamical behavior due to the radial eccentric force. In [23], the model was improved by including the tangential flux density which was ignored in the papers above. The average tangential stress was calculated from motor torque and used that in obtaining the tangential flux density. The radial eccentric force was calculated using Maxwell stress tensor at no load condition. A four poles turbo generator was modeled to show the nonlinear effect of the radial eccentric force. The mass unbalance was included in [24] in a Jeffcott rotor based on the results of [21]. The electrical and mechanical equations were combined in [25] by using Lagrange's equation with generalized force for a brushless DC (BLDC) motor. All these papers were only focused on the radial eccentric force. Besides, the two assumptions mentioned above make the model less accurate. The first assumption (infinite iron core permeability) results in a bigger force than its actual value since the air gap MMF drop was over-estimated and the machine saturation was not taken into account.

[26] modeled a cage induction motor by using winding analysis and the radial eccentric force was studied. The distributed stator windings were written in Fourier series expansion and used to calculate the machine impedances. Radial eccentric force was obtained using Maxwell stress tensor method. The authors in [27][28] continued the study for paralleled winding and compared their results with experiments. The winding

analysis method was improved in [29] by developing a modified winding function which counted the influence of eccentricity on MMF distribution. The characteristic of motor torque was investigated, which helped identifying the motor fault of eccentricity. The motor model with winding analysis included all the MMF space harmonics due to winding distribution. However, machine saturation was still not included in the model.

[30] used the basic method of [31] for a two pole turbogenerator and included rotor eddy current effects. In the model, an eccentric motor was transformed into a concentric case by coordinates mapping. Both radial and tangential flux density were calculated and used in Maxwell stress tensor calculation. Similar as the literatures mentioned above, this method still follows the same assumptions. [32] analyzed the radial eccentric force of bearingless switched reluctance motors (BSRM) based on turn angle of rotor. Magnetic inductance of air gap was calculated using equivalent magnetic path. Equivalent system stiffness was also derived.

Finite element method (FEM) is also used for the motor eccentricity problem. [32] calculated the radial eccentric force of a synchronous generator and did the noise analysis. The motor eccentric force – both radial and tangential – was studied in [33] when the motor rotor was in a whirling motion. [34] investigated the radial Maxwell stress tensor and wrote it in double Fourier series expansion of induction motors. Then the vibration pattern due to radial eccentric force was identified under rotor whirling. FEM can be considered having high accuracy. However, it is very time consuming to mesh the machine and solve the Maxwell equations, especially for dynamic eccentric simulation.

With the methods of calculating the motor eccentric force, mechanical system stability was studied and its considerable influence was pointed out by researches. [35] derived the equation of motion (EOM) of a Jeffcott rotor model with unbalanced mass and radial eccentric force. The radial eccentric force was calculated using energy method under same assumptions as [21]-[25]. System instability of free vibration and forced vibration due to mass unbalance excitation were investigated. Their results showed the effect of the motor air gap flux density on the system natural frequency. Also jumping phenomenon was observed in the whirling amplitude-frequency relationship for forced vibration. The influence of radial eccentric force on hydropower generator was studied in [36]. The expression of the constant component of the radial eccentric force was used. A mechanical system with four degrees of freedom (DOF) was modeled. The results indicated the system could become unstable in certain operating condition. Same mechanical system was modeled in [4] with both radial and tangential eccentric forces. FEM was used to calculate the forces for no-load and full-load conditions. The results showed the eccentric force affected both system damped natural frequencies and stability significantly. In [37], the authors further extended the hydropower generator model with importing the radial and tangential eccentric forces under whirling condition. Bifurcation was observed besides jumping phenomenon in [36].

Since the motor eccentric force has significant influence in mechanical system, a calculation method capable for both radial and tangential eccentric force is required, which should also balance the model accuracy and computation time. By searching through the literatures, magnetic equivalent circuit method (MEC) can be a suitable way

to analyze the eccentric motor field. It models an electric motor as a reluctance network and calculates the magnetic fields in the entire machine without loss important magnetic characteristics. But the computation time is fairly short. Thus, it can give relatively accurate results when requiring less modeling effort and shorter computation time compared to finite element method.

MEC is used in different types of motor/generator modeling and transient simulation [38]-[45]. In [46], the capability of MEC for machine modeling and design was investigated by summarizing the results of literatures. From limited comparison of MEC with FEM and experiments, they concluded MEC can be a promised tool for modeling and design. [47] used MEC for induction machine fault modeling, which provided a good agreement with experiments and FEM.

MEC is also used to analysis the motor eccentric problem. In [48], the squirrel-cage induction motor was modeled and the radial eccentric force was calculated by energy method. And vibrations and acoustic noise were also analyzed by structural FEM analysis. In [49], cage induction motors were modeled with rotor misalignment and eccentricity in 3D. However, both of these two papers did not count for the tangential eccentric force, which is very important for mechanical system stability as mentioned in [4].

To calculate both the radial and tangential force, the tangential flux density is required to be obtained. To achieve this, a more complex MEC network is needed. [50] provided a detailed modeling way for machine modeling in MEC. Permeance expressions were presented for different flux tube shapes. Coupling of electric and

magnetic circuits was detailed explained Also transient and static simulation steps were illustrated. The MEC was further improved by [51] and [52]. In [51], a MEC element with two direction flux flow was introduced. This made the calculation of air gap tangential flux density feasible. In [52], 3D model of induction machine was used as design tool. The MEC was done with 3D elements in which flux flow in three directions as in FEM. The model accuracy was obtained by refining element meshes and compared to FEM and experiments. Also the author pointed out FEM did not predict well when the machine had saturation.

In this dissertation, a simplified MEC model in 2D is proposed based on [52] for faster computation time, in which the main characteristics of the motor flux distribution are kept and machine saturation is also included. Both the radial and tangential eccentric forces will be calculated using Maxwell stress tensor. The proposed MEC will be coupled with the motor electric model for transient simulation, which is also capable for dynamic eccentric case. The proposed model will also be compared with FEM (Ansys Maxwell) for verification. The radial and tangential eccentric forces will be used to obtain the equivalent negative stiffness and used in mechanical system stability analysis with a Jeffcott rotor model. The nonlinear motion of the mechanical model introduced by the motor eccentric forces will also be studied.

CHAPTER III

VFD MACHINERY TRAIN MODELING THEORY*

A complete VFD machinery system can be divided into two major sub systems – electrical and mechanical as shown in Fig. 4.

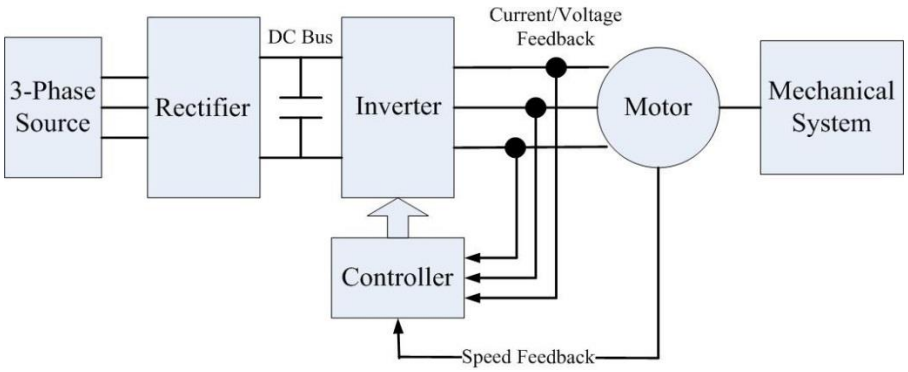

Fig. 4 VFD machinery train with voltage source inverter VSI

3.1 Electrical System

The electrical-mechanical sub systems interface is the electrical motor. The electromagnetic torque is generated inside the motor due to electromagnetic interactions, and the motor rotor is part of the mechanical system. The mathematical model of an

* Reprinted with permission from "VFD Machinery Vibration Fatigue Life and Multi-Level Inverter Effect" by Xu Han and Alan Palazzolo, 2013, *IEEE Transactions on Industry Application*, Volume 49, Issue 6, pp. 2562-2575, Copyright [2013] by IEEE.

induction motor shown below employs the q-d frame [53] approach, which is obtained by coordinate transformation from a 3-phase a-b-c frame.

Kirchoff's Voltage Balance Equations:

$$v_{ds} = r_s i_{ds} + \frac{d}{dt}\lambda_{ds} - \omega\lambda_{qs} \tag{1}$$

$$v_{qs} = r_s i_{qs} + \frac{d}{dt}\lambda_{qs} + \omega\lambda_{ds} \tag{2}$$

$$v'_{dr} = r'_r i'_{dr} + \frac{d}{dt}\lambda'_{dr} - (\omega - \omega_r)\lambda'_{qr} \tag{3}$$

$$v'_{qr} = r'_r i'_{qr} + \frac{d}{dt}\lambda'_{qr} + (\omega - \omega_r)\lambda'_{dr} \tag{4}$$

Flux Current Relation Equations:

$$\lambda_{ds} = L_{ls} i_{ds} + L_m (i_{ds} + i'_{dr}) \tag{5}$$

$$\lambda_{qs} = L_{ls} i_{qs} + L_m (i_{qs} + i'_{qr}) \tag{6}$$

$$\lambda'_{dr} = L_{ls} i'_{dr} + L_m (i_{ds} + i'_{dr}) \tag{7}$$

$$\lambda'_{qr} = L_{ls} i'_{qr} + L_m (i_{qs} + i'_{qr}) \tag{8}$$

Torque Current Relation Equations:

$$T_e = \frac{3}{2}\frac{P}{2} L_m (i_{qs} i'_{dr} - i_{ds} i'_{qr}) \tag{9}$$

where v and i represent voltage and current qualities, respectively; r, L and λ represent resistance, inductance and flux qualities, respectively; Subscripts q and d indicate q and d axis components, respectively; Subscripts s and r indicate stator and rotor components;

Subscript *m* indicates magnetizing component; Superscript " ' " indicates turn ratio transformation; ω_r is the rotor angular velocity in rad/s; T_e is the electromagnetic torque; *P* is the number of pole pairs.

The three-phase AC voltage source provides electric power to the entire system. This voltage is applied to the input of a rectifier stage which converts the AC power to DC. Capacitors/inductors and filters are implemented on the DC bus to smooth the voltage/current by filtering harmonics. The controller plays an important role in the drive system, which determines the trigger sequence and time intervals of the power switches. For the open-loop control there is no speed feedback from the motor. The controller utilizes a constant Volts/Hertz ratio for obtaining different operating speeds. A slip frequency compensator can be used to get the motor running close to the target speed. For closed-loop control, the speed sensor feeds back the motor rotor speed into the speed regulator, which is commonly a PI controller with acceleration rate bounds and outputs the reference torque. The torque and flux is estimated by the observer according to measured currents and voltages, based on equivalent q-d circuits. The torque and flux control depends on specific vector control algorithm, such as field-oriented control (FOC) and direct torque control (DTC) for induction motors. The vector control gives the reference three phase currents, which can be used to determine switch sequences for the current source inverter (CSI) or go through the current regulator in order to give the switch control for the voltage source inverter (VSI).

The inverter converts DC voltage/current into AC with the desired amplitude and frequency, by utilizing PWM techniques controlled by switching signals from the controller.

The conventional type of PWM inverter is a two-level inverter, which has two voltage levels and six switches for three arms (Fig. 5). The output is a square waveform as shown in Fig. 6(a) with one high voltage level and one low voltage level. The approach for avoiding some of the harmonics of the two-level inverter is to employ a multilevel PWM inverter, which has multiple voltage levels, and more accurately approximates a sine wave as illustrated in Fig. 6(b). There are mainly three topologies for multilevel inverters – cascaded H-bridges, diode-clamped multilevel inverter and flying-capacitor multilevel inverter [15]. Many algorithms have been developed to generate the multilevel PWM signal. The total harmonic distortion (THD) is reduced by using multilevel inverters [14][15], where THD is ratio of the sum of all higher harmonic amplitude to the fundamental frequency power amplitude when the input is an ideal sine wave.

$$THD = \frac{\sqrt{V_2^2 + V_3^2 + \cdots + V_n^2}}{V_1} \tag{10}$$

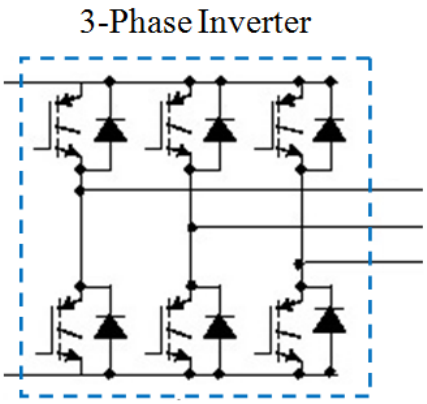

Fig. 5 Two-level inverter topology

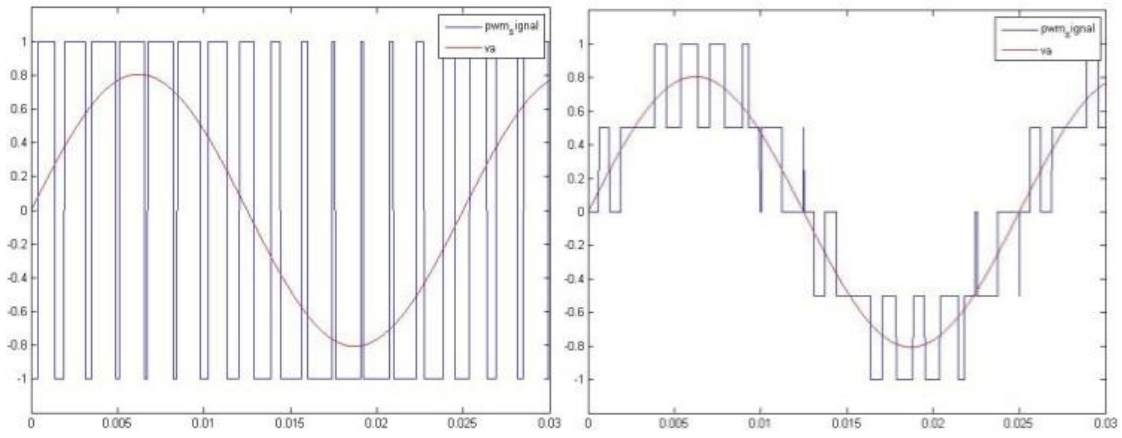

(a) Two-Level (b) Five-Level

Fig. 6 PWM signals for two-level and five-level inverters

Both the two-level and multilevel inverters "chop" the input DC voltage at a high-frequency. The chopped voltage/current signal contains many high frequency harmonics which interact with the motor fundamental frequency, resulting in relatively low frequency torque harmonics as given in [19].

(11)

Where *m* and *n* are integers such that

The frequencies provide by these formulas appear in the numerical example's torques provided later in this paper. A resonance is said to occur if one of these torque frequencies coincides with a mechanical natural frequency. The torsional motion and stress amplitudes at resonance depends on the amplitude of the corresponding torque harmonic, its proximity to the natural frequency and the damping of the vibration mode in resonance. Severe vibration and possible failure may result even if the torque harmonic amplitude at the resonance frequency is low when the damping is very light, so users and manufacturers employ couplings that add damping.

For sake of illustration and because of their widespread usage, only VSI with open-loop Volts/Hertz method are considered here. In addition to the torque harmonic due to the PWM, other torque harmonics induced by VSI are discussed in [10], including the effect of dead time compensation based on current measurement, asymmetric dead time voltage and magnetic saturation.

3.2 Mechanical System

A mechanical system is composed with inertias, shafts, couplings, bearings, gears etc. In this paper, the machinery train is modeled with lumped masses at *n* nodes and with *n-1* beam elements that connect the nodes. Each element between two neighboring nodes is modeled with a stiffness and a damping. The gears are considered as rigid teeth for torsional motion model. There is only one degree of freedom (DOF) θ_i on each node if only torsional motion is considered, where *i* indicates the node number.

The inertia matrix for a *n* node model without gears is

$$I = \begin{bmatrix} I_1 & & & 0 \\ & I_2 & & \\ & & \ddots & \\ 0 & & & I_n \end{bmatrix} \tag{12}$$

where I_i is the lumped inertia at the *i*th node.

The shaft element stiffness matrix and damping matrix connecting two nodes are given by

$$K_{i,i+1} = \begin{bmatrix} k_{i,i+1} & -k_{i,i+1} \\ -k_{i,i+1} & k_{i,i+1} \end{bmatrix} \tag{13}$$

$$C_{i,i+1} = \begin{bmatrix} c_{i,i+1} & -c_{i,i+1} \\ -c_{i,i+1} & c_{i,i+1} \end{bmatrix} \tag{14}$$

where $k_{i,i+1}$ and $c_{i,i+1}$ are the stiffness and damping between node *i* and *i+1*, respectively.

The shaft element stiffness connecting nodes *i* and *i+1* is

$$k_{i,i+1} = \frac{G_{i,i+1} J_{i,i+1}}{L_{i,i+1}} \tag{15}$$

where G is the shear modulus of the element; L is the length of the element; J is the torsion constant.

The system stiffness and damping matrix is assembled from $k_{i,i+1}$, $c_{i,i+1}$ and bearing damping at each node.

$$\underset{n\times n}{\underline{K}} = \begin{bmatrix} k_{1,2} & -k_{1,2} & 0 & \cdots & 0 \\ -k_{1,2} & k_{1,2}+k_{2,3} & -k_{2,3} & & \\ 0 & -k_{2,3} & k_{2,3}+k_{3,4} & & \\ \vdots & & & \ddots & \vdots \\ 0 & & & \cdots & k_{n-1,n} \end{bmatrix} \tag{16}$$

$$\underset{n\times n}{\underline{C}_s} = \begin{bmatrix} c_{1,2} & -c_{1,2} & 0 & \cdots & 0 \\ -c_{1,2} & c_{1,2}+c_{2,3} & -c_{2,3} & & \\ 0 & -c_{2,3} & c_{2,3}+c_{3,4} & & \\ \vdots & & & \ddots & \vdots \\ 0 & & & \cdots & c_{n-1,n} \end{bmatrix} \tag{17}$$

$$\underset{n\times n}{\underline{C}} = \begin{bmatrix} c_1^b & 0 & 0 & \cdots & 0 \\ 0 & c_2^b & 0 & & \\ 0 & 0 & c_3^b & & \\ \vdots & & & \ddots & \vdots \\ 0 & & & \cdots & c_n^b \end{bmatrix} \tag{18}$$

where c_i^b is bearing damping of node i.

The external torque applied to the system is

$$\underset{n\times 1}{\underline{T}} = \begin{bmatrix} T_1 \\ \vdots \\ T_n \end{bmatrix} \tag{19}$$

The complete mechanical system equation of motion is

$$\underset{n\times n}{\underline{I}}\ \underset{n\times 1}{\ddot{\underline{\theta}}}+\left(\underset{n\times n}{\underline{C}_s}+\underset{n\times n}{\underline{C}_b}\right)\underset{n\times 1}{\dot{\underline{\theta}}}+\underset{n\times n}{\underline{K}}\ \underset{n\times 1}{\underline{\theta}}=\underset{n\times 1}{\underline{T}} \tag{20}$$

For a system with n nodes and m set of gears, the system has *n-m* DOFs since a gear set adds a motion constraint between the driver gear and the follower. The system state mass, stiffness and damping matrices can be easily derived with a gear ratio transform. Details are provided in [54].

3.3 Torsional Fatigue and Life Prediction

3.3.1 The S-N Curve

The cyclic stress-life relation for ductile materials undergoing cyclic, constant amplitude stress is typically described by an S-N curve [55], as shown in Fig. 7.

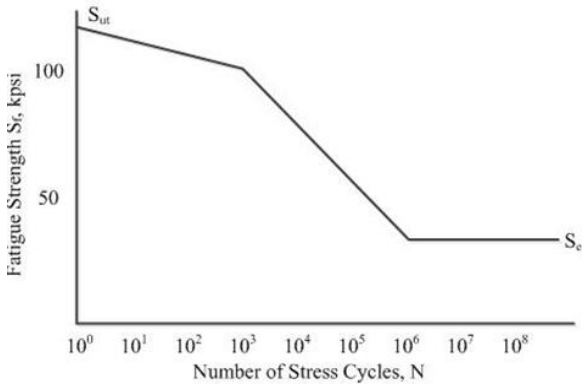

Fig. 7 Typical S-N curve

The S-N curve is typically expressed by the following form where S_f is the cyclic stress amplitude; N is number of cycles to failure; The constants a and b are typically defined from the $N=10^3$ and $N=10^4$ points as

$$a = \frac{\left(fS_{ut}\right)^2}{S_e} \tag{21}$$

$$b = -\frac{1}{3}\log\left(\frac{fS_{ut}}{S_e}\right) \tag{22}$$

where f is the fatigue strength fraction; S_{ut} is the ultimate stress; S_e is the endurance limit.

Then the number of cycles to failure can be calculated from

$$N = \left(\frac{\sigma_a}{a}\right)^{\frac{1}{b}} \tag{23}$$

where σ_a is the alternating stress amplitude.

3.3.2 Effective Shear Stress

The combination of mean and alternating stress requires the definition of an effective stress for determining fatigue life by using the S-N curves. The shear stress in a shaft or coupling due to pure torsional loading is given by

$$\tau = \frac{T \cdot r_{outer}}{J} \tag{24}$$

$$J = \frac{\pi\left(r_{outer}^4 - r_{inner}^4\right)}{2} \tag{25}$$

where τ is the shear stress; T is the transmitted torque through the coupling/shaft; r_{outer} is the outer radius of the coupling/shaft; r_{inner} is the inner radius of the coupling/shaft; J is the torsion constant.

[55] states that

"Experimental results tend to show that the value of the mean shear stress has no influence on the fatigue life of a ductile structural component subjected to cyclic torsional loading as long as the maximum stress is less than the yield strength of the material. Shigley and Mitchell stated 'up to a certain point, torsional mean stress has no effect on the torsional endurance limit'. Hence, the plot of the alternating shear stress τ_a *versus mean shear stress* τ_m *bound by a horizontal line with* $\tau_a = \tau_e$ *and a 45 deg yield line."*

This criteria is illustrated in Fig. 8. Loss of life occurs for a fluctuating pure torsional load with τ_m and τ_a, when either

$$\tau_m < \tau_y - \tau_e \text{ and } \tau_a > \tau_e$$

$$\Rightarrow \tau_{eff} = \tau_a \text{ (mean stress has no influence)}$$

or

$$\tau_m > \tau_y - \tau_e \text{ and } \tau_a > \tau_y - \tau_m$$

$$\Rightarrow \tau_{eff} = \frac{\tau_a}{\left(\frac{\tau_y - \tau_m}{\tau_e}\right)} \text{ (mean stress has influence)}$$

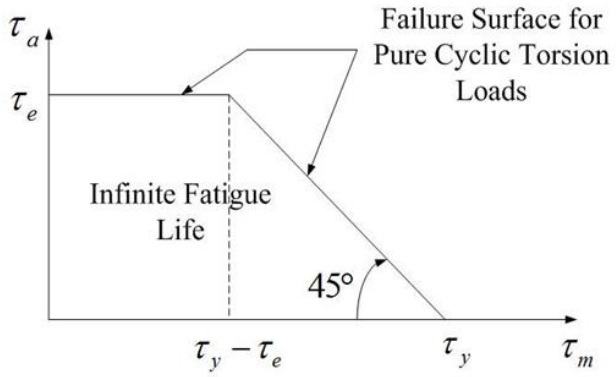

Fig. 8 Pure torsion load criterion, where τ_e is the endurance limit, τ_y is the torsional yield strength, τ_m is the mean stress, and τ_a is the alternating stress

Endurance limit τ_e values provided in the reference literature typically correspond to highly polished "ideal" specimens. The reduction in endurance limit due to manufacturing, installation, loading and environmental conditions is accounted for by multiplying the ideal endurance limit by so called Marin factors [56], as expressed by

$$\tau_e' = \tau_e \times k_a \times k_b \times k_c \times k_d \times k_e \times k_f \tag{26}$$

where k_a=1.58×$S_{ut}^{-0.086}$, surface factor, using ground finish (S_{ut} in MPa); k_b=1.24×$d^{-0.107}$(2.79<d<51) or 1.51×$d^{-0.157}$ (51<d<254), size factor; d is shaft diameter in mm; k_c=0.577, loading factor for torsion; k_d=1, temperature factor for 20 ℃; k_e=0.897, reliability factor for 90% reliability; k_f=1, miscellaneous effects factor.

The effective shear stress should be multiplied by a stress concentration factor if geometric discontinuities, such as keyways, occur along the shaft [56].

3.3.3 Varying Fluctuating Stress and Rain-Flow Algorithm

Usage of the above approaches assumes constant values for the mean stress τ_m and alternating stress τ_a. The Rain-flow algorithm is utilized for the case that τ_m and τ_a vary with time, e.g. during a machinery train startup.

The rain-flow algorithm decomposes a varying fluctuating stress load into a series of simple stress load reversals, which have constant τ_m and τ_a (for details, please refer to [57] and [58]). Then the accumulated damage *D* can be derived by Miner's rule by obtaining the number of cycles for each simple stress level.

$$D = \sum \frac{n_i}{N_i} \tag{27}$$

where n_i is the number of cycles obtained from the Rain-flow algorithm for the *i*th stress amplitude reversal level; N_i is the number of cycles to failure for *i*th stress reversal obtained from a S-N curve.

Failure is estimated to occur when *D* exceeds 1, so 1/*D* indicates how many times the original stress load can be applied before failure.

CHAPTER IV

INFLUENCE OF VFDS ON ROTORDYNAMICS*

A stand-alone code is developed for the analysis of coupled electrical and mechanical systems (Fig. 9). It has capability to model the both the electric and mechanical systems, including inverter, motor, controller and mechanical components.

For simplicity, the three-phase AC voltage source and the DC bus capacitors are not included in the model. Because the motor torque harmonics are due to the PWM switching. Also the DC bus voltage is smoothed by the large capacitor and nearly kept a constant. Thus a model with a constant DC bus and inverter is capable to catch the characteristic of the motor torque harmonics due to PWM, which is important to study the influence of VFDs on mechanical vibrations.

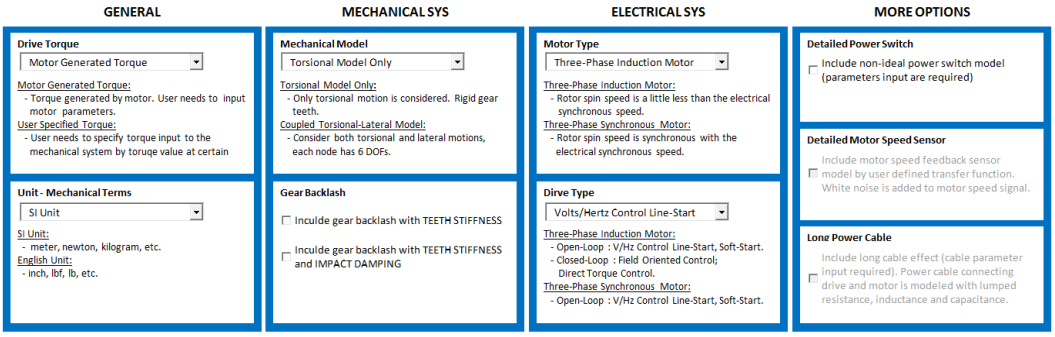

Fig. 9 Stand-alone code excel interface

* Part of the data reported in this chapter is reprinted with permission from "VFD Machinery Vibration Fatigue Life and Multi-Level Inverter Effect" by Xu Han and Alan Palazzolo, 2013, *IEEE Transactions on Industry Application*, Volume 49, Issue 6, pp. 2562-2575, Copyright [2013] by IEEE.

4.1 System Description

A simple mechanical machinery train with two inertias is simulated to illustrate resonance vibration due to VFD. The system is includes a simple open-loop Volts/Hertz control method and only pure torsional motions. The prediction of system life for the case of resonance response is considered. The entire system is illustrated in Fig. 10.

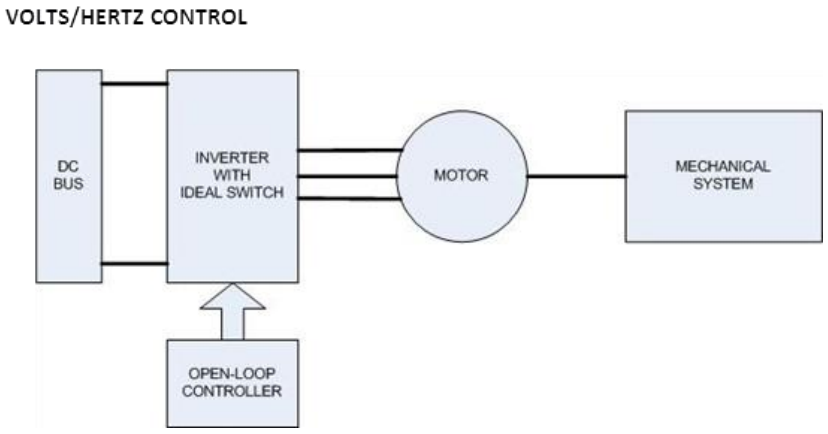

Fig. 10 Simple mechanical machinery train with open-loop control

4.1.1 Electrical System

The power electronics system shown in Fig. 11 includes a constant DC bus voltage, and a three-arm, two-level inverter composed by six IGBTs.

The switching signal is generated by a carrier-based PWM, which compares the triangular carrier signal with the sinusoidal modulation signal. The magnitude of the

sinusoidal modulation signal is proportional to the electrical frequency, to keep a constant Volts/Hertz ratio. For simplicity, all the power switches are considered as ideal.

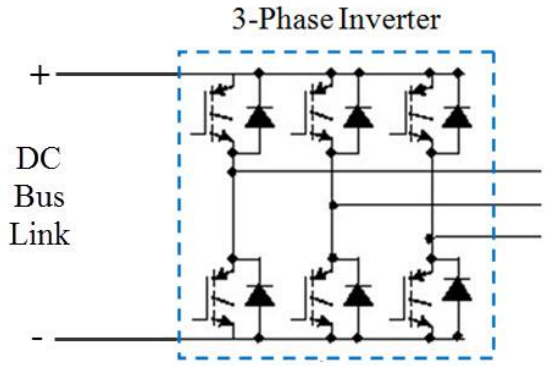

Fig. 11 Example electrical system

4.1.2 Mechanical System

The mechanical system shown in Fig. 12 represents a simple two-mass system with a compressor driven by a motor. The motor electrical parameters and system mechanical parameters are listed in Tab. 1 and Tab. 2, respectively. The system's undamped natural frequency is 37.24 Hz, and the damped natural frequency is 37.23 Hz. The constant load acting on the compressor is 800 N.m. and the mean coupling shear stress is about 9.032e7 N/m^2.

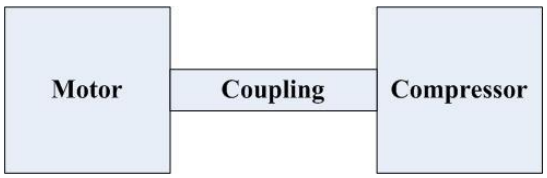

Fig. 12 Example mechanical system

Tab. 1 Motor electrical parameters

Nominal Power	200 HP (149 kW)
Nominal Voltage	460 V
Nominal Frequency	60 Hz
Stator Resistance	0.01818 ohm
Stator Leakage Inductance	0.00019 H
Rotor Resistance	0.009956 ohm
Rotor Leakage Inductance	0.00019 H
Mutual Inductance	0.009415 H
Number of Poles	4

Tab. 2 System mechanical parameters

Motor Inertia	2.6 $kg.m^2$
Motor Bearing Damping	0.04789 N.m/(rad/s)
Compressor Inertia	2.5 $kg.m^2$
Compressor Bearing Damping	0 N.m/(rad/s)
Coupling Stiffness	6.9781e4 N.m/rad
Coupling Damping	10 N.m/(rad/s)
Coupling Length	0.2667 m
Coupling Radius (outer/inner)	0.0254 m / 0.02286 m
Coupling Shear Modulus	8.27e10 N/m^2

4.2 Torque Harmonic Verification

The motor input voltage frequency is set to 60 Hz (electrical frequency), which determines the mechanical spin speed which is approximately 30 Hz. The PWM carrier frequency is held constant at 1080 Hz. The resultant motor speed, electromagnetic

torque spectrums, shear stress and shear stress spectrums are shown in Fig. 13. The harmonic frequencies match the theoretical formula described in [16]. For the 60 Hz case, f_e=60 Hz and f_{pwm}=1080 Hz. By (12), f_T = 180,360,540…Hz.

Fig. 14 shows an interference plot with the torque harmonics based on (12) with f_{pwm} =1080 Hz. The horizontal axis indicates the electrical frequency, while the vertical axis presents the torque harmonic frequency. The horizontal line indicates the system natural frequency 37.24 Hz. The intersecting points are possible resonance points where the torque harmonic coincides with the system natural frequency.

Fig. 15 shows responses for an electrical frequency of 53.2 Hz, at which clearly indicates a resonance condition. The torque spectrum shows a harmonic component at 37.2 Hz which is very close to the system natural frequency 37.23 Hz. The shear stress zero-peak alternating component is approximately 1.004e7 N/m^2 at steady state, which far exceeds its counterpart stress at the electrical frequencies of 60 Hz, indicating occurrence of a resonance. Clearly the magnitude (6.067 N.m., zero-peak) of the 37.2 Hz torque harmonic in Fig. 15 (b) is smaller than other ones, i.e. at 320 Hz (22.48 N.m., zero-peak). However, the shear stress spectrum in Fig. 15 (d) shows a strong dominance of the 37.2 Hz component, supporting the evidence of resonance. This supports the assertion in [16], that the frequency of a torque harmonic has much greater importance than its magnitude.

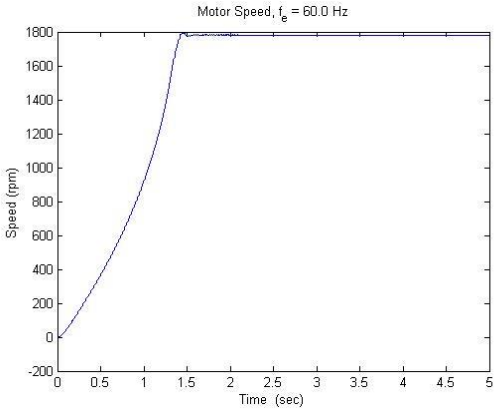

(a) Motor speed

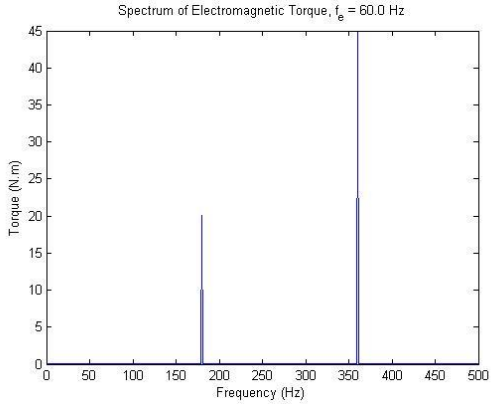

(b) Torque spectrum

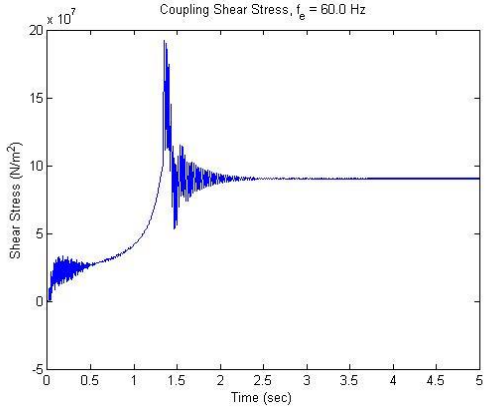

(c) Coupling shear stress

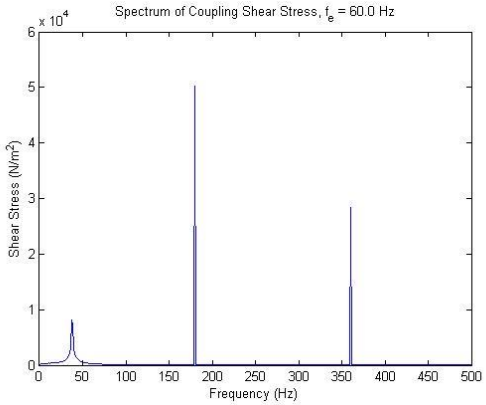

(d) Shear stress spectrum

Fig. 13 f_e = 60 Hz simulation results

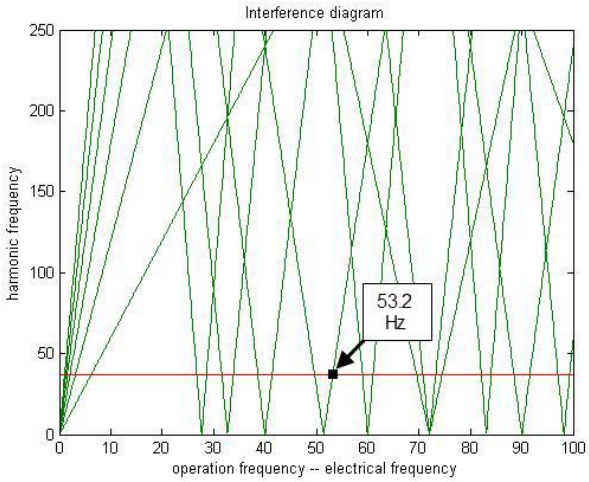

Fig. 14 Interference diagram for f_{pwm} = 1080 Hz

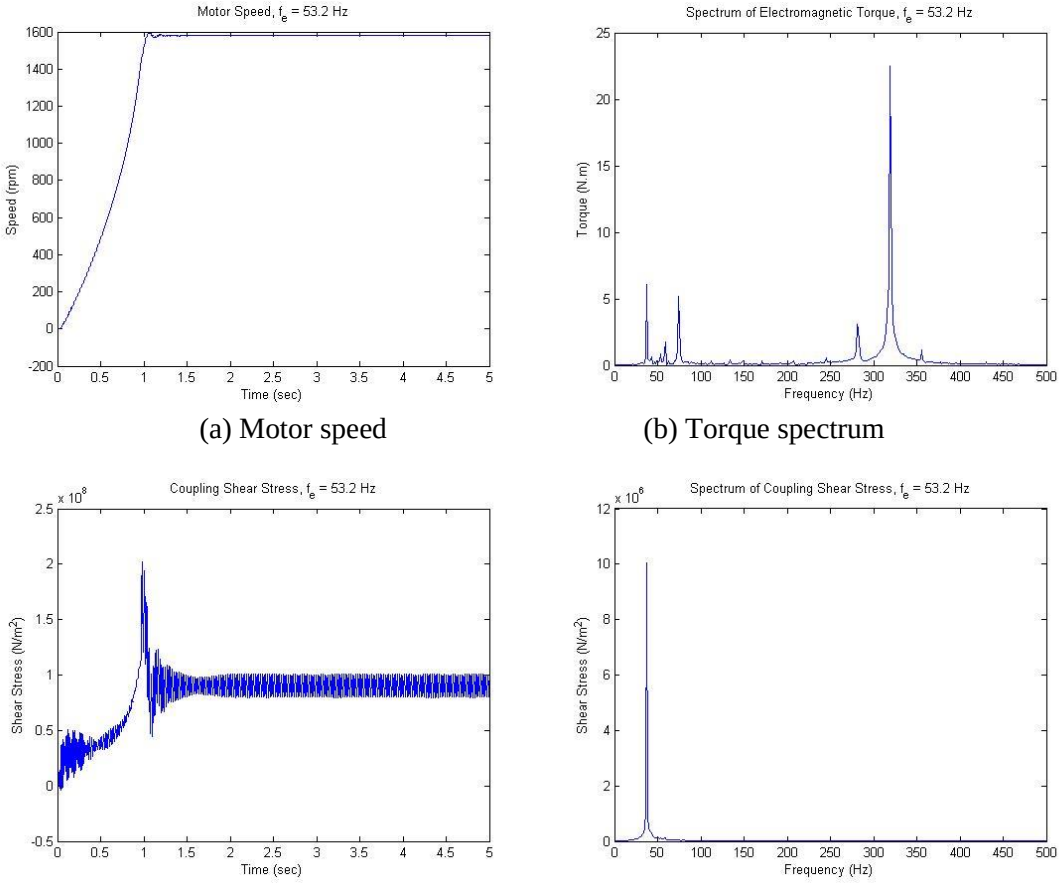

(a) Motor speed (b) Torque spectrum

(c) Coupling shear stress (d) Shear stress spectrum

Fig. 15 f_e=53.2 Hz simulation results

4.3 Life Prediction

Large shear stresses that result from resonant operation of machinery may significantly reduce shaft or coupling life even after a relatively short duration. The S-N curve and Rain-flow algorithm are employed to provide a quantitative estimate of the life reduction and estimated time to failure, as discussed above. The coupling material specifications are listed in Tab. 3 for this example.

Tab. 3 Coupling tensile specification

Coupling Tensile Ultimate Strength S_{ut}	1.11e9 N/m^2
Coupling Tensile Yield Strength S_y	71e7 N/m^2
Coupling Fatigue Strength Exponent b	-0.091
Surface Factor k_a	0.87
Size Factor k_b	0.8162
Loading Factor k_c	0.577
Temperature Factor k_d	1
Reliability Factor k_e	0.897
Miscellaneous Effects Factor k_f	1
Keyway Concentration Factor	3

The torsional stress specifications are obtained from the following equations [5][59] relating tensile and torsional strength.

$$\text{Torsional endurance limit } \tau_e = \frac{S_{ut}}{25} \tag{28}$$

$$\text{Torsional yield strength } \tau_y = 0.55 S_y \tag{29}$$

Resonance life prediction is based on the shear stress record between t = 4 and t = 5 seconds in Fig. 15(c). Failure is predicted to occur after 46.05 repetitions of this operation cycle, which in this case is a very short duration: 46.05 sec.

Fig. 16 and Tab. 4 show the effect of varying the electrical frequency on alternating shear stress and life, with the PWM switching frequency maintained at 1080 Hz. for all cases. Fig. 16 should not be interpreted as a standard frequency response plot as utilized in controls modeling or resonance studies, since the electrical frequency is not

the excitation frequency, but instead changes the excitation frequency according with (12) and Fig. 14.

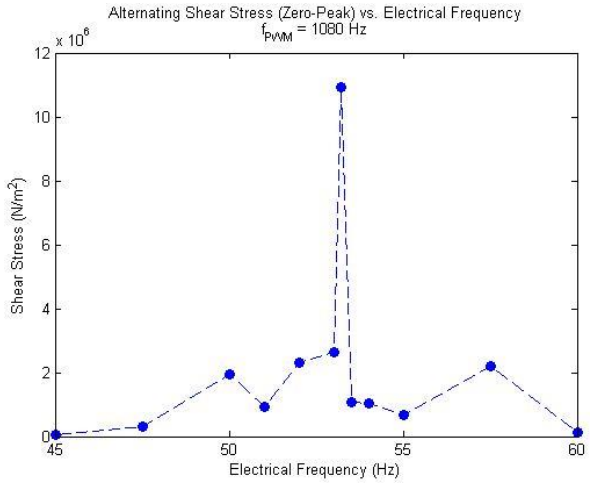

Fig. 16 Alternating shear stress vs. electrical frequency with f_{pwm} = 1080 Hz, f_e = 45~60 Hz

Tab. 4 Alternating shear stress and predicted life vs. electrical frequency with f_{pwm}=1080 Hz and mean shear stress of 9.032e7 N/m^2

Electrical Frequency f_e (Hz)	Alternating Steady State Shear Stress Zero-Peak (N/m^2)	Steady State Operation Time before Failure (sec)
45	0.71e5	Inf
50	19.37e5	Inf
53	26.27e5	Inf
53.2	100.4e5	46.0505
53.5	10.57e5	Inf
55	6.79e5	Inf
60	1.36e5	Inf

Fig. 17 and Tab. 5 show the effect of coupling damping on alternating shear stress and coupling life. The shear stress is seen to be significantly reduced and life significantly increased with increased coupling damping. This represents a common remedy for torsional shear stress induced high cycle fatigue failures in machinery.

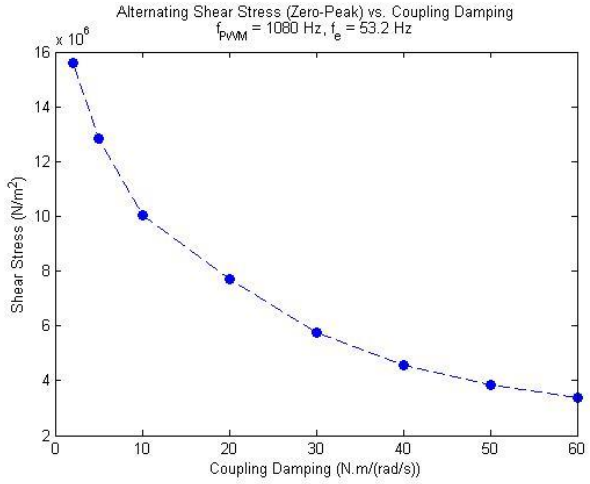

Fig. 17 Alternating shear stress vs. coupling damping with f_e = 53.2 Hz, f_{pwm}= 1080 Hz

Tab. 5 Alternating shear stress and predicted life vs. electrical frequency with f_e = 53.2 Hz, f_{pwm} = 1080 Hz

Coupling Damping (N.m.s)	Alternating Steady State Shear Stress Zero-Peak (N/m^2)	Steady State Operation Time before Failure (sec)
2	15.6e6	2.8048
5	12.8e6	4.9824
10	10.04e6	46.0505
20	7.72e6	1.7631e3
30	5.74e6	5.6029e5
40	4.58e6	Inf
60	3.36e6	Inf

4.4 Simulation with Multilevel Inverters

A comparison between the three-level and five-level inverter approaches is made for the resonance case, where f_e = 53.2 Hz. The simulation results are shown in Fig. 18 and Fig. 19 for three-level and five-level inverters approaches, respectively. The five-level inverter shear stress responses are smaller than the three-level but are still significant at resonance.

A comparison of the steady-state torque, resonance alternating shear stress component and steady state operation time before failure between two-level, three-level and five-level inverter system is shown in Tab. 6. The mean shear stress is approximately 9.032e7 N/m^2. Note that although the overall peak-peak steady state torque pulsation magnitude decreases as the number of inverter level increases, the torque component near the resonance frequency may increase. This explains why the three level inverter shear stress is much larger than the two-level inverter shear stress. The five-level inverter shear stress is less than the three-level inverter shear stress, but is larger than the two level inverter shear stress.

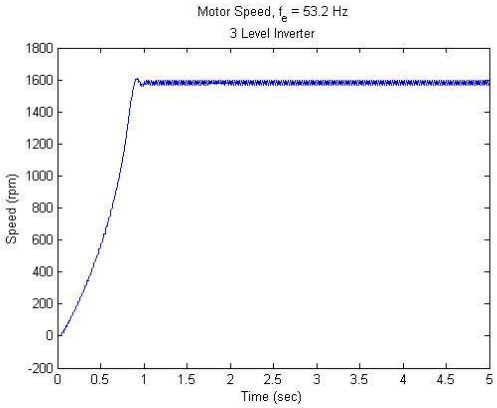

(a) Motor speed

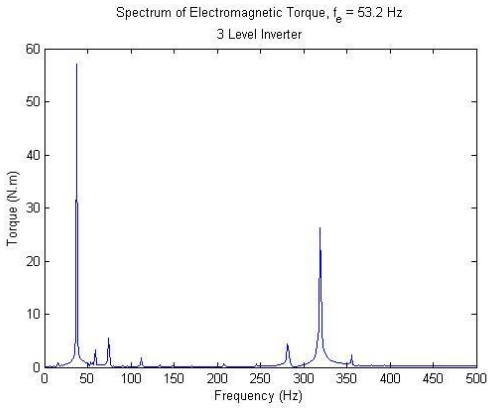

(b) Torque spectrum

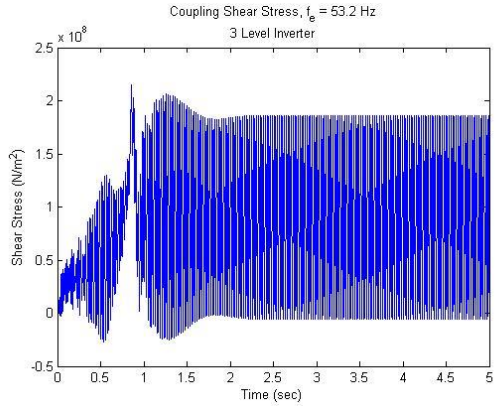

(c) Coupling shear stress

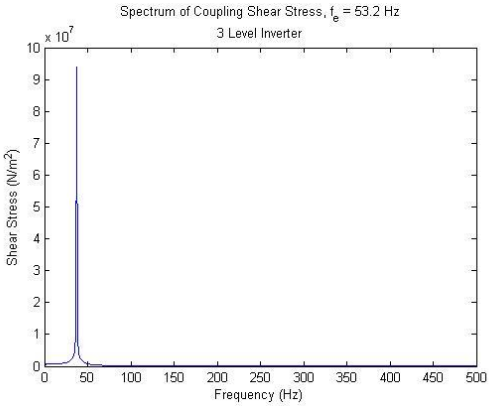

(d) Shear stress spectrum

Fig. 18 f_e = 53.2 Hz, three-level inverter simulation results

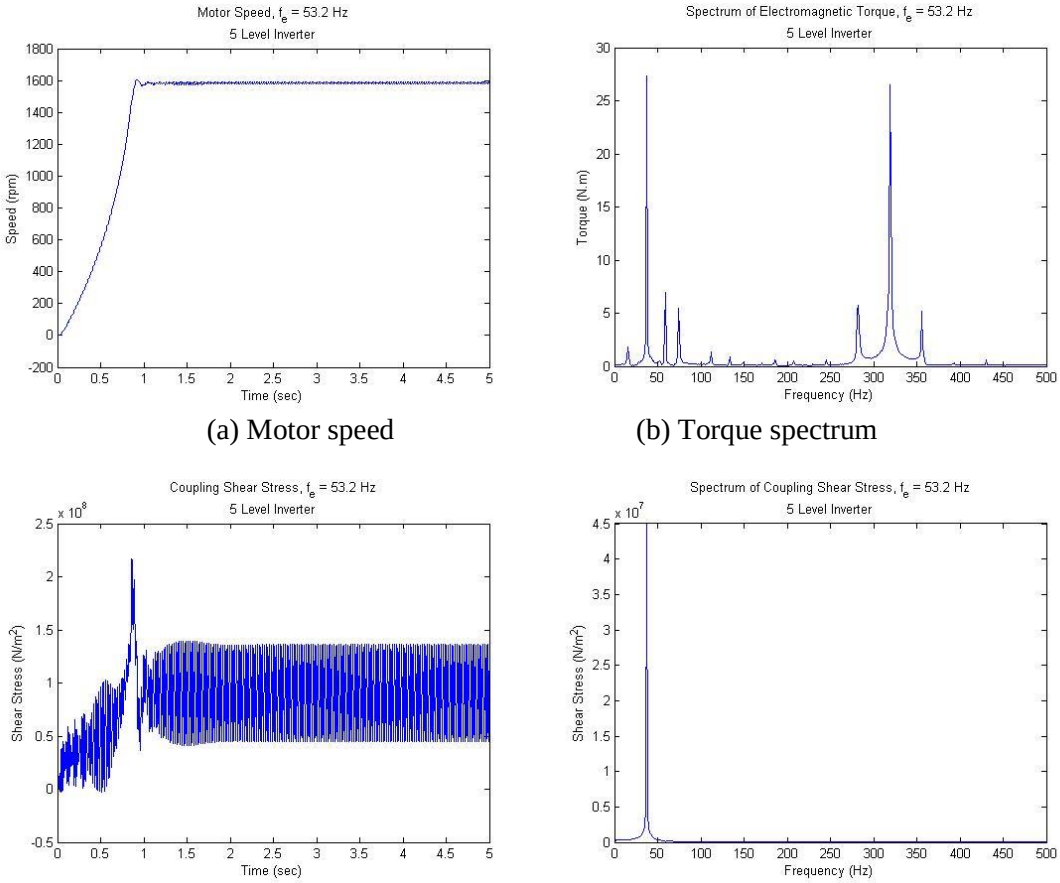

(a) Motor speed (b) Torque spectrum

(c) Coupling shear stress (d) Shear stress spectrum

Fig. 19 f_e = 53.2 Hz, five-level inverter simulation results

Tab. 6 Comparison of steady-state alternating shear stress for two-level, three-level and five-level inverters with f_e = 53.2 Hz

No. of Inverter Levels	Motor Input Voltage THD Phase-Neutral (%)	Alternating Motor Torque zero-peak (N.m)	Motor Torque at Resonance Freq. zero-peak (N.m)	Alternating Shear Stress at Resonance Freq. zero-peak (N/m^2)	Steady State Operation Time before Failure (sec)
2-level	63.42	251.8	6.067	1.004e7	46.0505
3-level	32.65	246.7	57.14	9.406e7	<1
5-level	16.41	134.7	27.36	4.497e7	<1

The reason for this is explained based on the torque-current relationship developed in [19] with the assumption that in rotating coordinates the stator and rotator currents are all dominated by large DC components. As stated in [19], the torque harmonic frequencies and current harmonic frequencies can be written as

(30)

(31)

where ,

The resonance frequency is 37.2 Hz, where f_{pwm} = 1080 Hz and f_e = 53.2 Hz. The corresponding m and n values for f_T = 37.2 Hz are

$$m = 1,\ n = 21 \tag{32}$$

The current harmonics that the cause the resonance inducing torque harmonic at 37.2 Hz, are those at 16.0 Hz, 90.4 Hz, 2144 Hz and 2250.4 Hz and are calculated by

$$x = 1,\ y = 21 \pm 1 = \begin{cases} 20 \\ 22 \end{cases} \tag{33}$$

$$f_c = | x \cdot f_{PWM} \pm y \cdot f_e | = \begin{cases} | 1 \cdot f_{PWM} \pm 20 \cdot f_e | \\ | 1 \cdot f_{PWM} \pm 22 \cdot f_e | \end{cases} \tag{34}$$

$$(3) \begin{cases} m = 2i + 1, \forall i = 0, 1, 2, \ldots \\ n = 3(2j + 1), \forall j = 0, 1, 2, \ldots \end{cases}$$

Vibrations and stresses are caused by torques which are in turn caused by currents. The currents result from voltages and therefore the cause of the vibration may be understood by considering voltages. The voltage harmonics at 16.0 Hz, 90.4 Hz, 2144 Hz and 2250.4 Hz are compared for the two-level, three-level and five-level inverter cases, as shown in Fig. 20.

The spectrum clearly shows the voltage harmonic magnitudes at 16.0 Hz, 90.4 Hz, 2144 Hz and 2250.4 Hz increase as the inverter level changes from two, to five, to three. The bigger the voltage harmonic, the bigger the current harmonic, and the bigger the corresponding torque harmonic component at 37.2 Hz. Thus the torque harmonic at 37.2 Hz increases as the inverter level changes from two, to five, to three. This and the presence of the mechanical natural frequency at 37.2 Hz explains why the vibration and stress increase as the inverter level changes from two, to five, to three. This result is consistent with the theory presented in [19] which provides formulae for related current and torque harmonic frequencies.

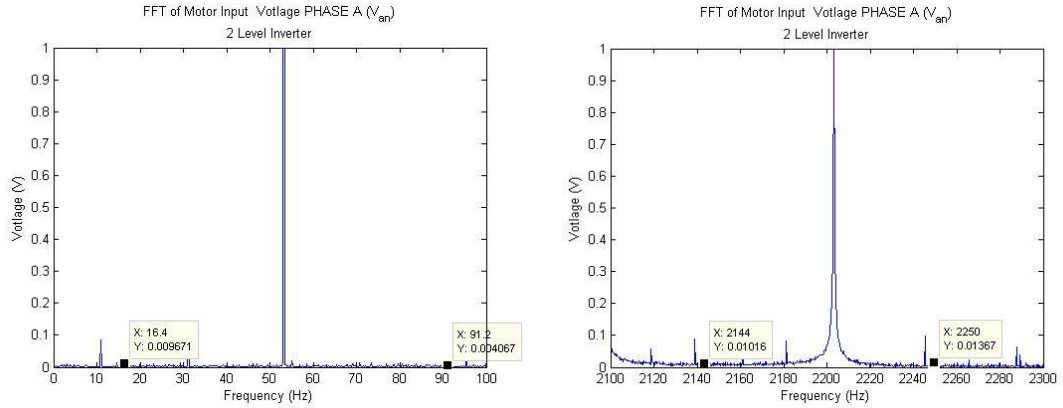

(a) Two-level inverter

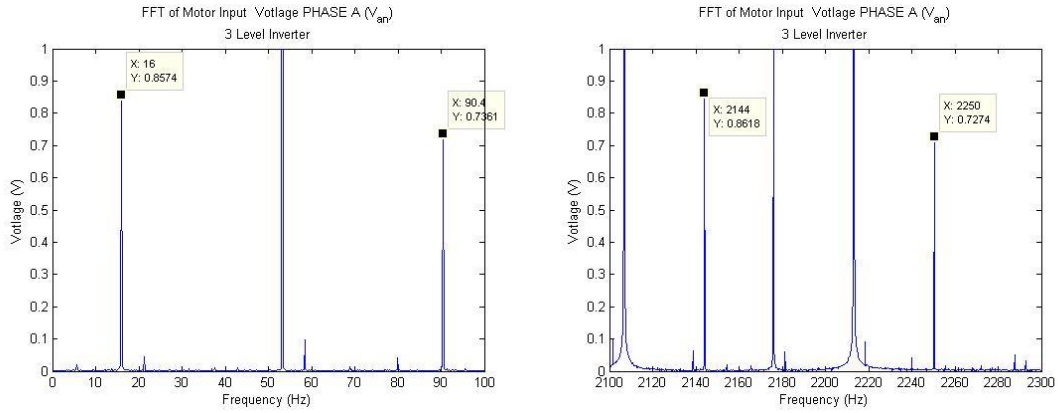

(b) Three-level inverter

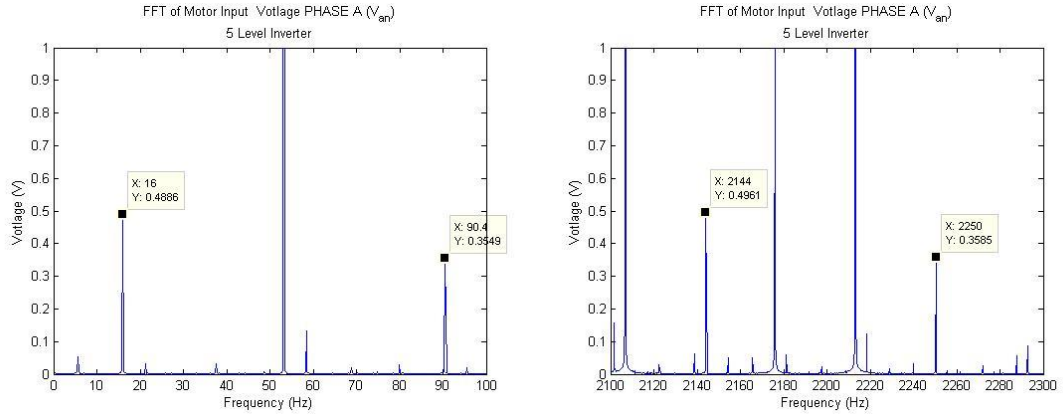

(c) Five-level inverter

Fig. 20 Comparison of voltage harmonics at 16.0 Hz, 90.4 Hz, 2144 Hz and 2250.4 Hz with f_e=53.2 Hz and f_{pwm}=1080 Hz

The resonance shear stress can be significantly reduced by changing the PWM switching frequency as illustrated for the case shown in Fig. 21 where the five level inverter f_{pwm} is increased from 1080 Hz to 1090 Hz, while maintaining the electrical frequency f_e = 53.2 Hz. This causes the alternating shear stress to reduce from 4.497e7 N/m^2 zero-peak to 2.997e6 N/m^2. And the steady state operation time before failure increases from less than 1 sec to infinity. Care should be taken in using this approach since the new f_{pwm} may produce torque harmonics that cause resonance at some other f_e.

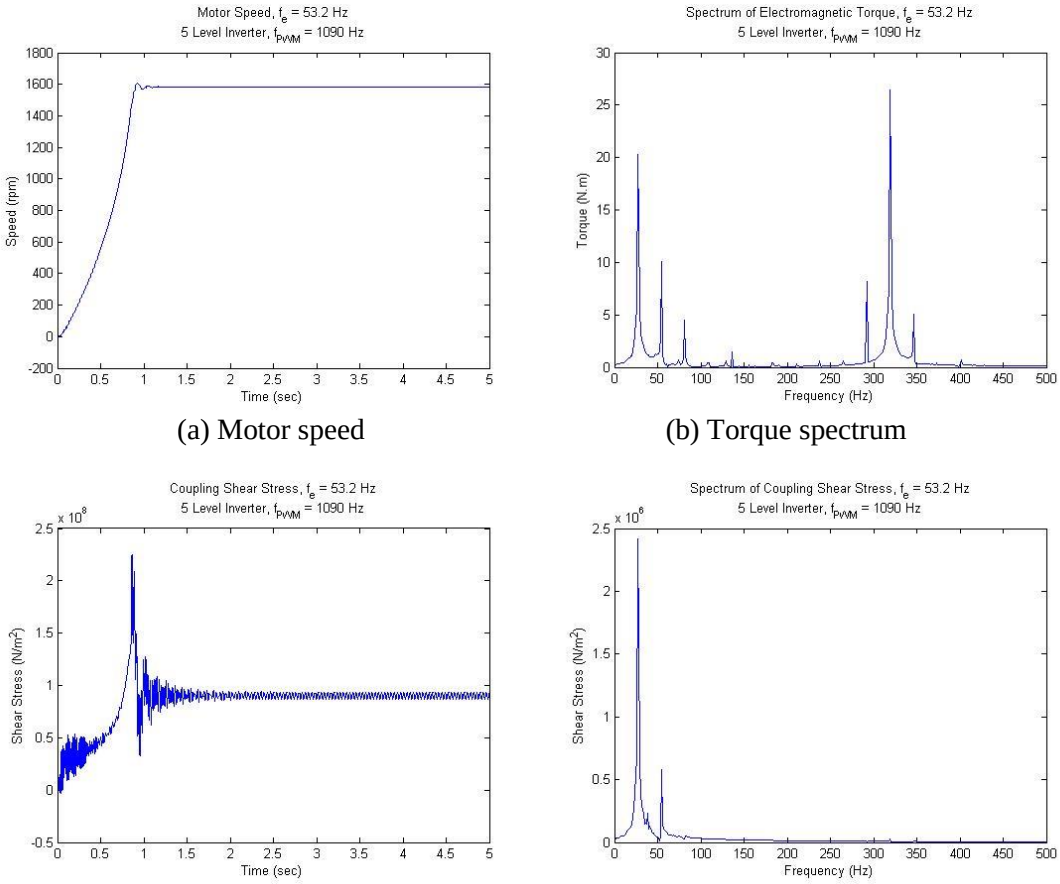

(a) Motor speed (b) Torque spectrum

(c) Coupling shear stress (d) Shear stress spectrum

Fig. 21 Simulation results for five-level inverter with f_e=53.2 Hz, f_{pwm}=1090 Hz

4.5 Comparing with Industry Field Test Data

A company has a machinery train driven by VFD suffering torsional vibration problem, which is shown in Fig. 22. The machinery train had a recurring failure on a VFD motor-fan train system, with broken mechanical coupling as shown in Fig. 23. The comparison to an actual train experiencing a VFD induced failure provides a good opportunity to validate the model. The predicted and measured responses showed important similarities and recommendations were made to add more coupling damping or lower the fan to motor weight ratio.

Fig. 22 Machinery train driven by VFD

Fig. 23 Broken coupling hub

4.5.1 System Description

The system block diagram is shown in Fig. 24. The motor and fan are connected by a coupling. The mechanical equipment is far away from the drive, which uses a 190 meter (623 feet) long cable to connect the motor and the drive. To avoid the high dv/dt ratio, a dv/dt filter is placed at the motor side.

The main components of the VFD are diode rectifier, DC bus link with brake chopper and capacitor (not shown in Fig. 24) , IGBT inverter, controller and current sensor measurements.

During the operation of this machinery train, the VFD is working at the constant Volts/Hertz ratio control method, which is commonly used for fan systems. Thus, the

current sensor only feeds back the measured current signals for protection and not for a closed-loop control. The PWM frequency is set to 1000 Hz.

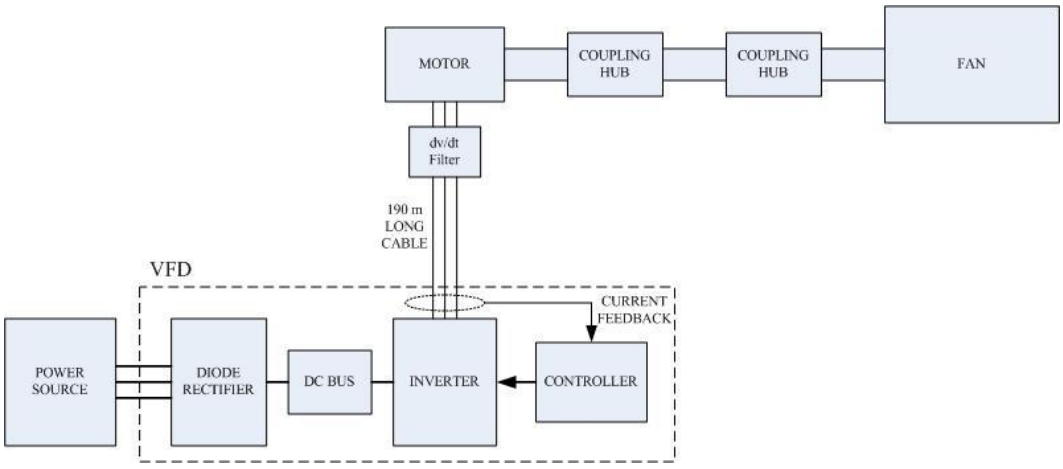

Fig. 24 Mechanical system block diagram

4.5.2 Mechanical System Modeling

The mechanical system is modeled with lumped masses and springs as Fig. 25. The motor is modeled as three masses connected with stiff springs. The parameters are shown in Tab. 7.

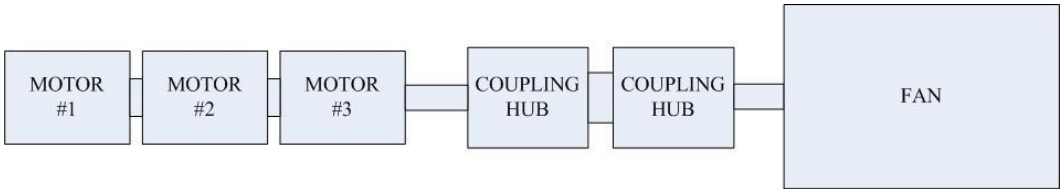

Fig. 25 Mechanical system modeling

Tab. 7 Mechanical parameters

Station	Motor Rotor	Motor Rotor	Motor Rotor	Coupling Hub	Coupling Hub	Fan
Station #	1	2	3	4	5	6
Inertia (in-lbf-s^2)	2.33	4.35	2.33	0.48	0.49	325.53
Stiffness 1e6 (in-lbf/rad)	247.29	247.29	12.85	2.24	2.83	

With these information, the mechanical system can be modeled as a linear differential equations with state space presentation. The torsional natural frequency (TNF) and corresponding mode shapes are calculated. The five natural frequencies are list in Tab. 8. Note except the first TNF, all the other TNFs are at very high frequency. Thus the first TNF is the most important one to be studied for a resonance.

Tab. 8 Torsional natural frequencies

No.	Torsional Natural Frequency (Hz)
1	55.9
2	490.9
3	905.8
4	1668.0
5	2368.2

The mode shape for the first TNF is shown in Fig. 26. By inspection of the system parameters, the stiffness between motor cores is very stiff, which indicates these three motor core stations are acting as a rigid body. Meanwhile, the fan's inertia is more

than 36 times of the motor, which indicates the biggest vibration on the motor side in the mode shape of the first TNF.

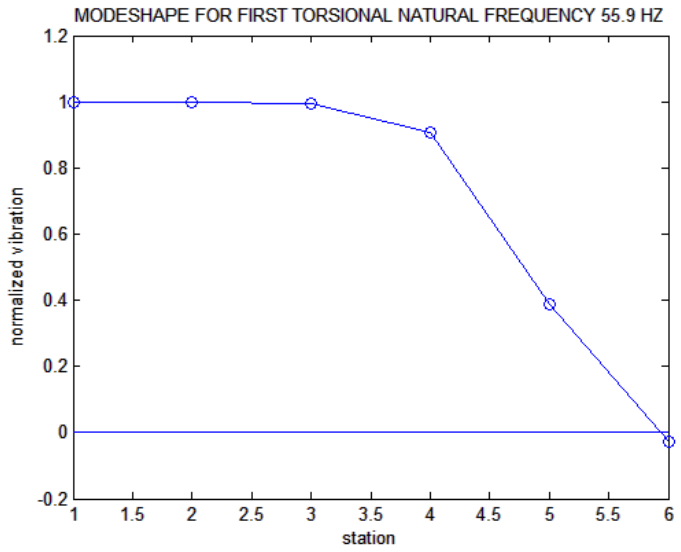

Fig. 26 Mode shape for 1st TNF 55.9 Hz

According to the experimental test, the amplification factor (AF) of the first TNF is 180. In the model, a damping of 0.001 is applied between the motor and the coupling hub.

4.5.3 Electrical System Modeling

The electrical system is model with DC bus, IGBT inverter, induction motor, controller and PWM generator. The block diagram is shown in Fig. 27.

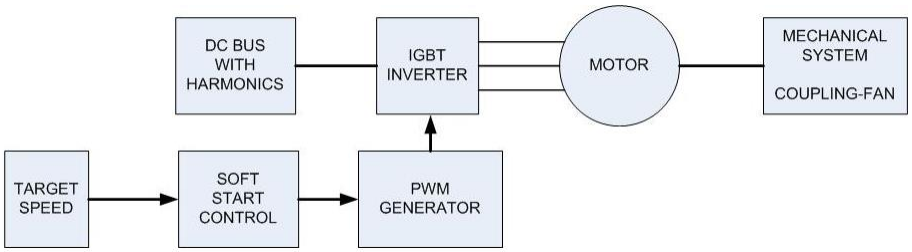

Fig. 27 Electrical system modeling

4.5.3.1 DC Bus Link

Since the DC bus link capacitor value is unknown (inside the drive), when modeling the system, the power source and rectifier are not modeled and a DC bus voltage is supplied to the inverter as an electrical source.

From the experimental test, the DC bus link has several harmonics at both positive and negative line, as shown in Fig. 28. The main harmonic is 75 V at 180 Hz. However, by observing the DC bus voltage signals in time domain, the harmonics on the positive and negative lines have the same phase. That means, if a measurement is performed between the two DC bus lines, the measured DC bus link voltage is nearly a constant (800 V).

Thus, in the model, the DC bus voltage is a 800 V constant with harmonics whose magnitude is read from the experimental test figure. The main harmonic in DC bus positive and negative line of 75 V (RMS) 180 Hz is added to the constant voltage. Other harmonics are also picked in different simulations to show the influence of these harmonics. The results indicate these harmonics on both positive and negative lines have

no influence. Fig. 29 shows the DC bus link voltage of both the positive and negative lines.

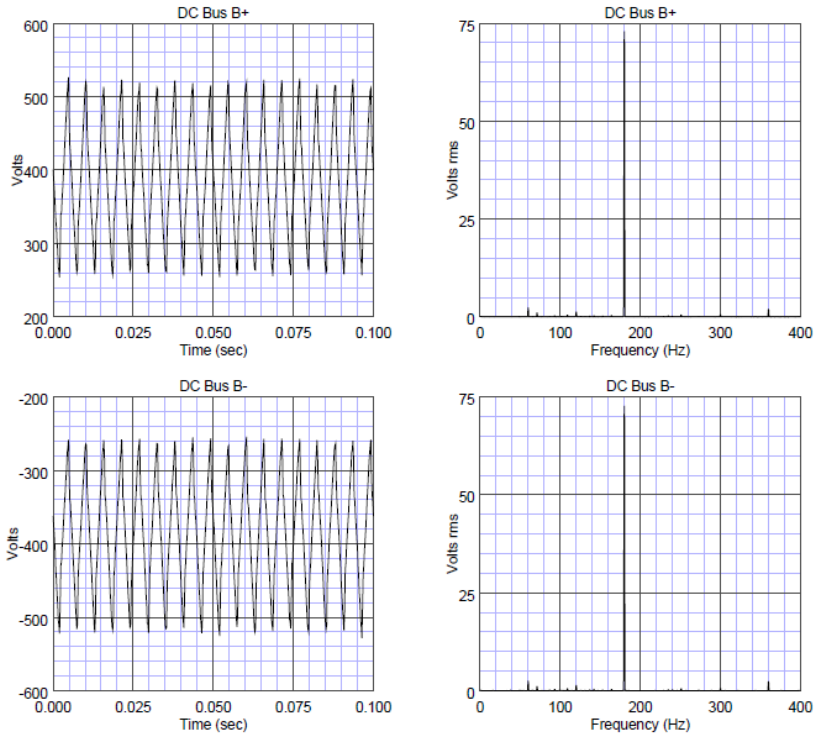

Fig. 28 DC bus link from experimental test

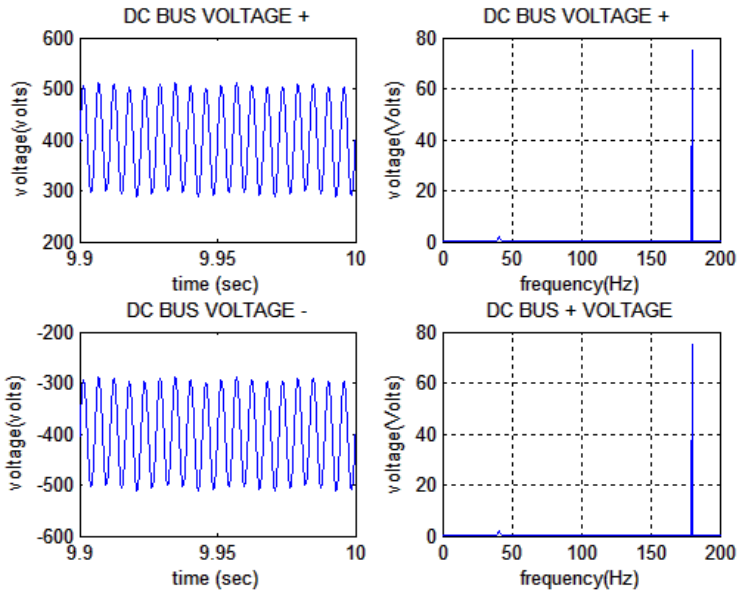

Fig. 29 DC bus link in simulation

4.5.3.2 Inverter

The inverter is modeled with ideal switches, since the fast switching IGBTs have little effect on the system vibrations.

4.5.3.3 Induction Motor

The induction motor is modeled with approximated parameters based on the information provided in the name plate [60]. The name plate values and approximated parameters are shown in Tab. 9 and Tab. 10.

Tab. 9 Induction motor name plate value

Output Power (hp)	25
Rated Speed (rpm)	1783
Rated Voltage (V)	460
Rated Efficiency	0.95
Rated Power Factor	0.65
Poles	4
NEMA Design Type	B
NEMA kva Code Letter	G

Tab. 10 Induction motor approximated per phase parameters

Stator Resistance (ohm)	0.0068
Stator Leakage Inductance (H)	0.00025108
Rotor Resistance (ohm)	0.0078
Rotor Leakage Inductance (H)	0.00037662
Magnetizing Inductance (H)	0.0058

4.5.3.4 Controller

In the model, the induction motor is controlled by simple open-loop Volts/Hertz method, the same as the VFD setting in the real machinery train. Soft start is implemented during simulation for transient.

4.5.3.5 PWM Generation

Carrier-based PWM generation is used in the modeling, which compares the triangular carrier signal (PWM frequency) and the sinusoidal modulation signal (electrical frequency). The PWM frequency is set to 1000 Hz as that in the drive.

4.5.4 1962 rpm Test

Note in the real machinery test, the test time is realtively too long for a simulation. Thus all simulated time periods are shortened compared with the actural test. For example, the start up time in a real machine test is 120 sec. But in the simulation, the start up time is set to be 15 sec due to the CPU speed and storage limit.

Fig. 30 shows the motor shaft torque time history as the motor runs up to 1962 rpm. The experimental test shows some motor shaft torque peaks at around 300 rpm, 950 rpm, 1700 rpm and final speed 1962 rpm as indicated in the figure. The simulation model is set to 1962 rpm. The results are shown in Fig. 31.

As indicated in Fig. 31, there are simillar peaks in the motor shaft torque around these 4 frequencies (but the magnitudes does not match).

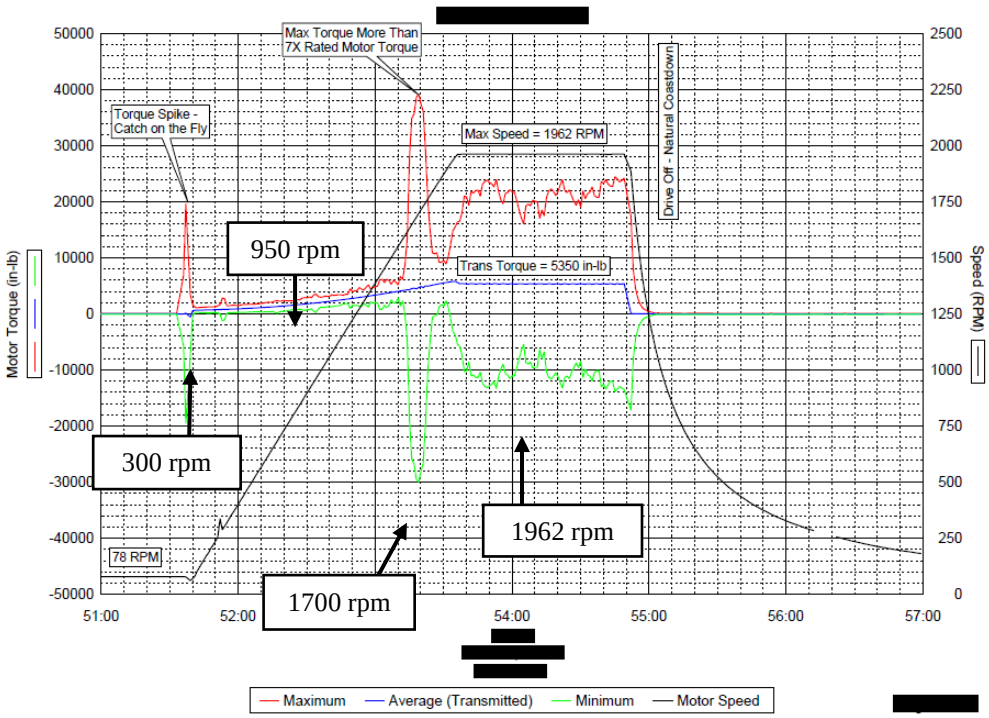

Fig. 30 1962 rpm test data

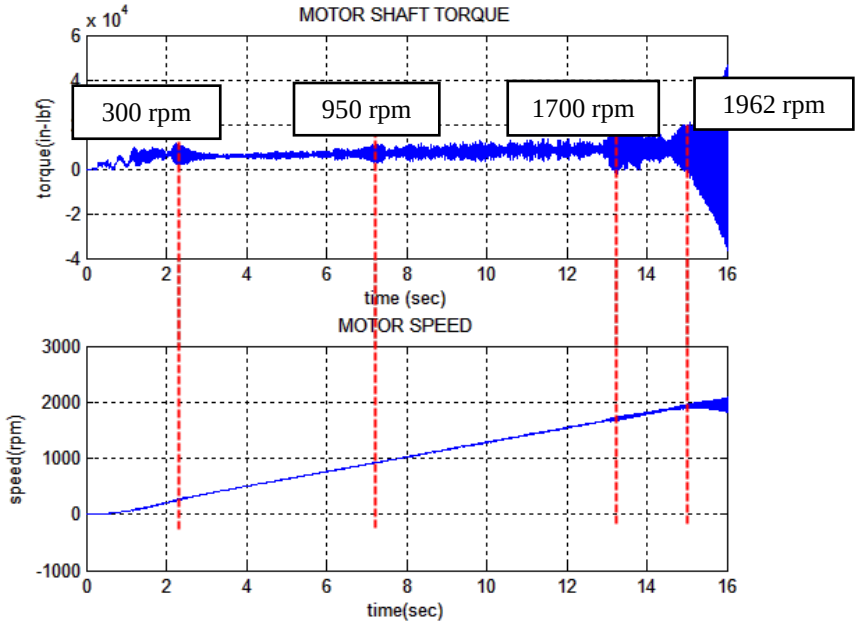

Fig. 31 1962 rpm simulation result

4.5.5 1700 rpm Test

Next the system is simulated to 1700 rpm. The test data in Fig. 32 shows the big motor shaft torque at around 1700 rpm. The simulation result (Fig. 33) also shows the peaks during transient and the resonance happened at 1700 rpm.

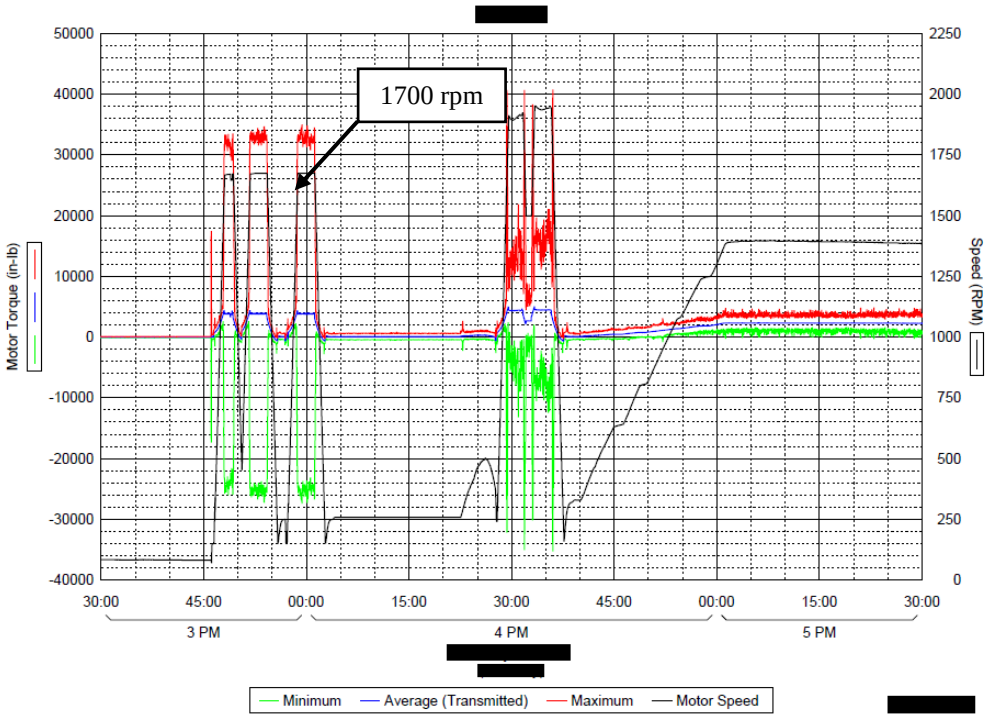

Fig. 32 1700 rpm test data

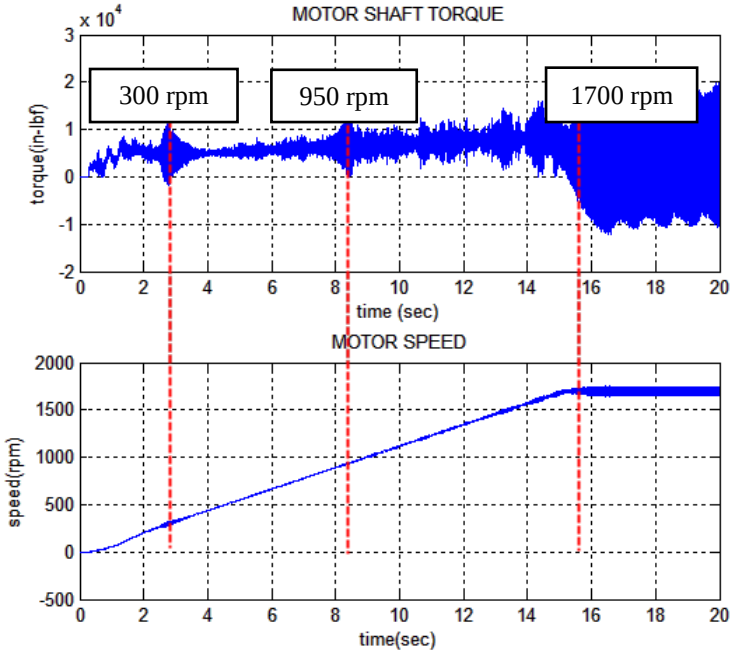

Fig. 33 1700 rpm simulation result

4.5.6 1700 – 1962 rpm Transient Test

Fig. 34 shows the machine is run up to 1700 rpm, then slows down and runs up to 1962 rpm. The model is set to 1700 rpm target speed. Than decrease its speed to 500 rpm and run up to 1962 rpm again. The results are shown in Fig. 35.

In Fig. 35, the two steady state at 1700 rpm and 1962 rpm are indicated in the red spuares. It is clear that at these two speed, the motor shaft torque alternating component is much bigger than at the other speed.

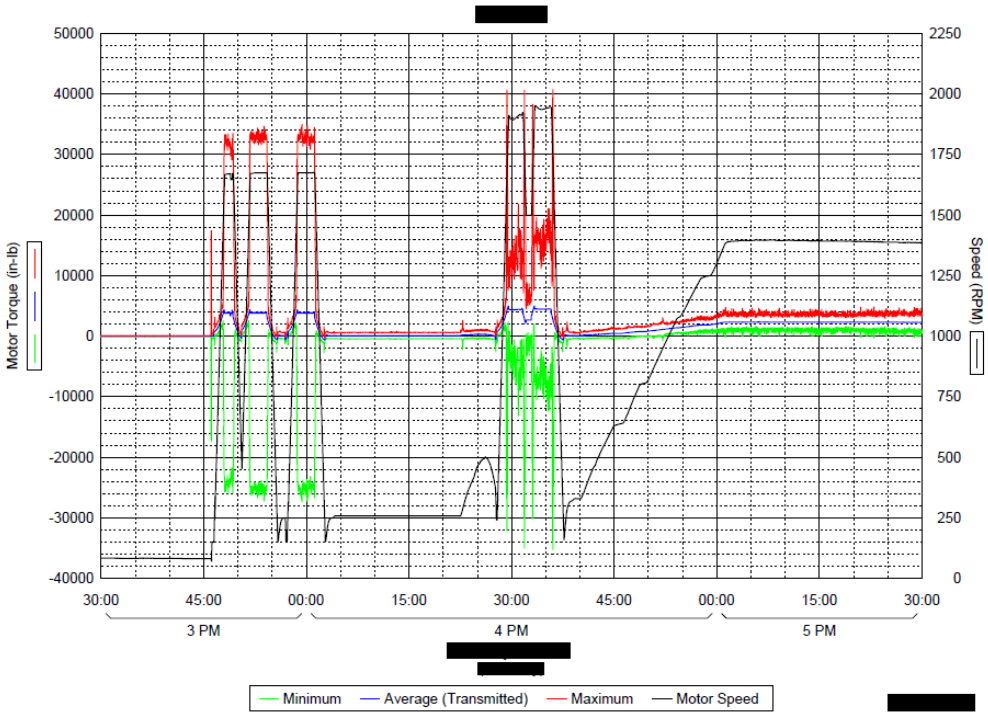

Fig. 34 1700-1962 rpm test data

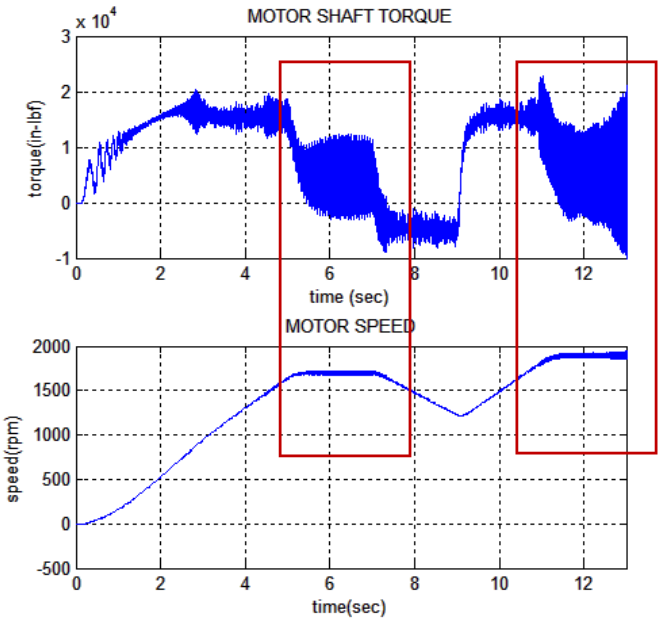

Fig. 35 1700-1962 rpm simulation result

4.5.7 Waterfall Plot for Current Spectrum

Fig. 36 shows the waterfall plot of the current spectrum from test data. It indicates current harmonic and sidebands separated by 41 Hz.

The waterfall plot from simulation is shown in Fig. 37 (2D) and Fig. 38 (3D) (200 rpm – 1700 rpm). Note there are sidebands of 41 Hz, 82 Hz, 124 Hz and 165 Hz, though not very obvious. But it presents the same pattern as the test data.

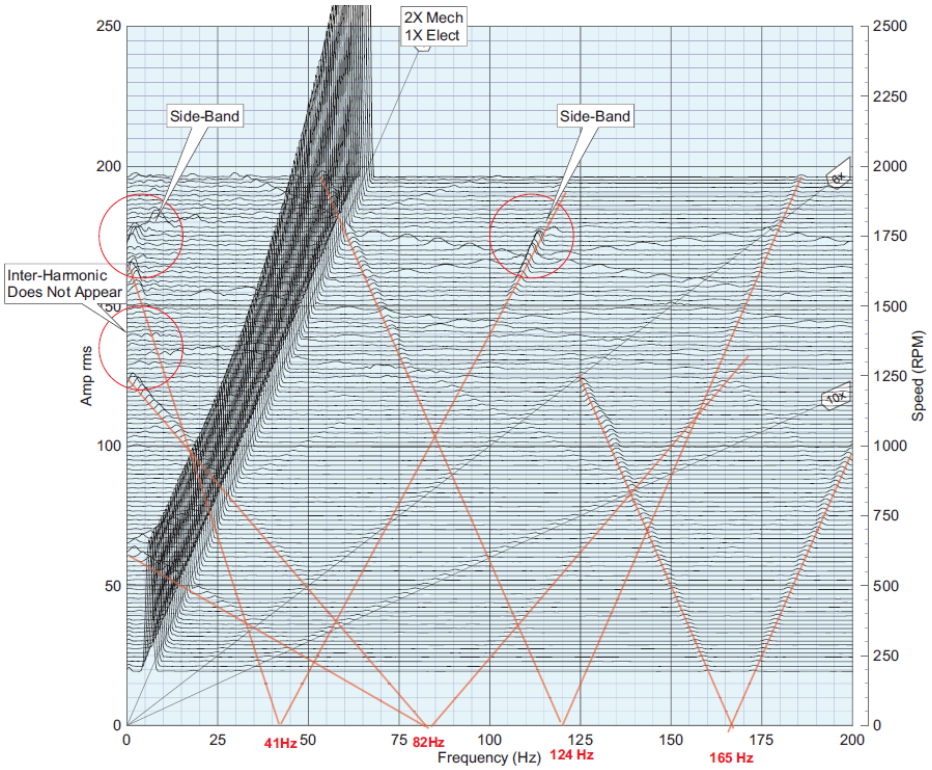

Fig. 36 Current spectrum test data

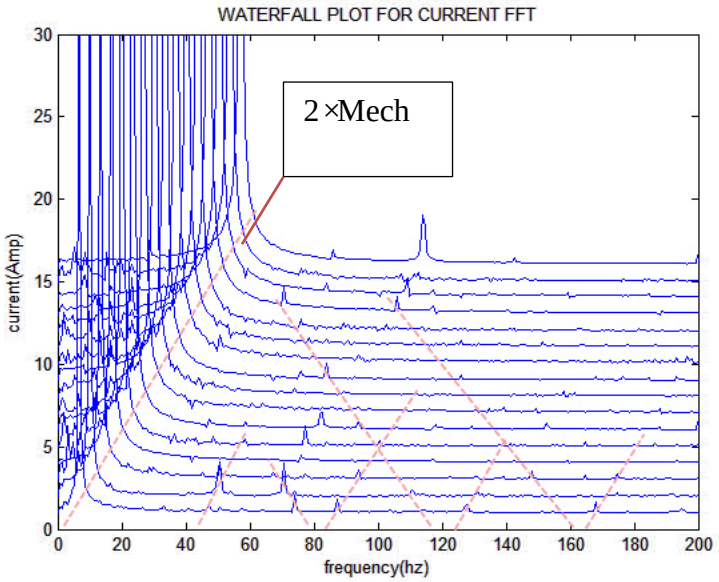

Fig. 37 Current spectrum simulation result - 2D

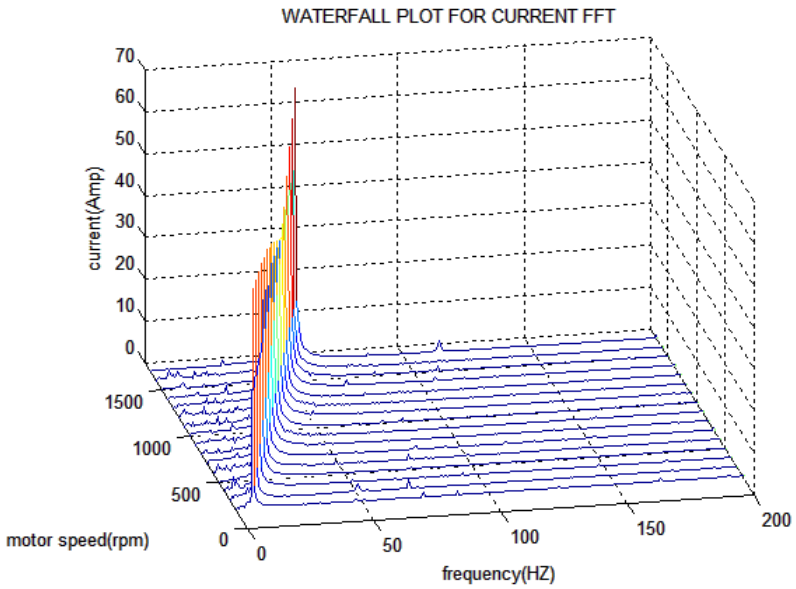

Fig. 38 Current spectrum simulation result – 3D

4.5.8 Harmonic Analysis and Identification

With PWM switching, the torque and current harmonics are related to the PWM frequency and electrical frequency as

$$\text{Torque harmonic} \quad f_T = | m \cdot f_{PWM} \pm n \cdot f_e | \tag{35}$$

$$\text{Current harmonic} \quad f_c = | x \cdot f_{PWM} \pm y \cdot f_e | \tag{36}$$

where $x = m,\ y = n \pm 1$

$$(1)\begin{cases} m = 0 \\ n = 6j, \forall j = 1,2,3,... \end{cases}$$

$$(2)\begin{cases} m = 2i, \forall i = 1,2,3,... \\ n = 3(2j), \forall j = 0,1,2,... \end{cases}$$

$$(3)\begin{cases} m = 2i+1, \forall i = 0,1,2,... \\ n = 3(2j+1), \forall j = 0,1,2,... \end{cases}$$

In the simulation, PWM frequency is 1000 Hz. For 300 rpm, 950 rpm, 1700rpm and 1962 rpm, the possible electromagnetic torque harmonics that induced torsional resonance are calculated based on the formula above and listed in

Tab. 11. Here $i < 3$ and $j < 10$. Since generally speaking, the higher m and n, the smaller the harmonics (too small to induce resonance). Note it is hard to tell which harmonic actually induced the resonance since the magnitudes of these harmonics are unknown and hard to predict.

Then compare the current frequencies with the waterfall plot. For 300 rpm case, the current spectrum is the second line from the bottom. There are clear peaks around 50 Hz and 70 Hz.

For 1700 rpm case, the current spectrum is the top first line. The peak near 110 Hz is easy to see.

Tab. 11 Electromagnetic torque harmonic

PWM Freqency 1000 Hz				
Operation Speed (rpm)	300	950	1700	1962
Electrical Freq (Hz)	10.1	31.9	57.2	66.0
m	0	1	2	6
n	6	33	36	90
Electromagnetic Torque Freq (Hz)	60.5	55.0	59.4	57.88
Current	50.5	23.0	2.2	8.1
Freq (Hz)	70.7	86.9	116.6	123.9

These harmonics are induced by the use of VFD. If an ideal source is used instead of the PWM-IGBT switching source, the steady state motor shaft torque is a constant, as presented in Fig. 39.This implies that a torque harmonic created by the switching supply is the source of the resonance.

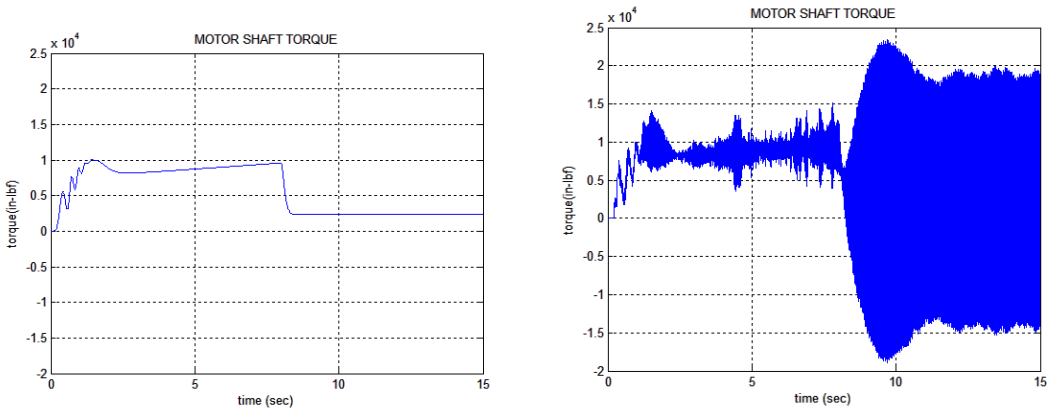

(a) Ideal source (b) VFD with PWM

Fig. 39 1700 rpm ideal source & VFD with PWM

4.5.9 Increase Damping

The system damping is increased from zeta = 0.001 to 0.75. Operating at 1700 rpm, the simulation result shows a big improve on vibration compared with that in Fig. 33.

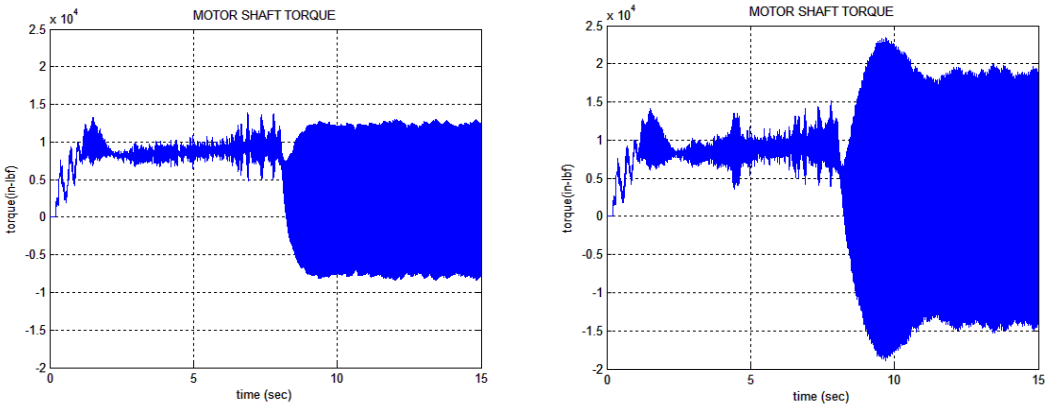

(a) zeta = 0.75 (b) zeta = 0.001

Fig. 40 1700 rpm simulation result with increased damping

CHAPTER V

MOTOR ECCENTRICITY MODELING THEORY

5.1 Magnetic Equivalent Circuit (MEC)

Equivalent magnetic circuit model models the motor with flux tubes. A flux tube is also an element in MEC, similar as in FEM. In each element, the flux has predefined flow directions and stays as a constant in that direction all through the tube. Analogues to the voltage in electric circuit, magnetic circuit are driven by magnetomotive force (MMF). The flux flow through the element has the following relationship with the MMF across the element in the defined direction.

$$MMFdrop = R\phi = \frac{1}{G}\phi \tag{37}$$

where R is the magnetic reluctance and G is the magnetic permeance. The permeance is the inverse of the reluctance.

The magnetic reluctance depends on both the material property and the element geometry. (38) presents the reluctance calculation for a simple flux tube shown in Fig. 41.

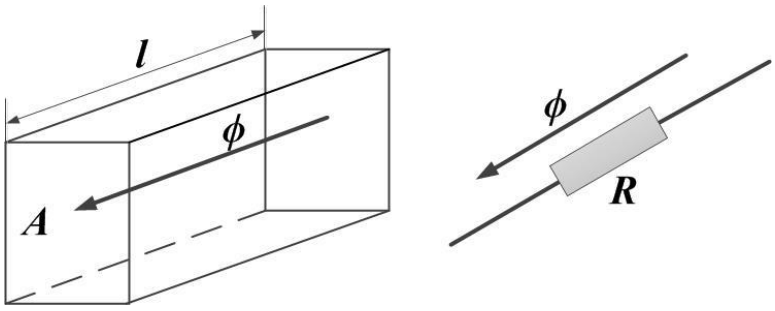

Fig. 41 Flux tube and MEC element

$$R = \frac{l}{\mu_0 \mu_r A} \tag{38}$$

where A is the area of the element cross section perpendicular to the flux flow direction; *l* is length of the element which is the distance the flux goes through.

In 2D motor modeling [52], the flux is defined to flow in two orthogonal directions, such that one direction presents radial and the other one presents tangential. Fig. 42 presents an element in x-y coordinate. The center gray blocks indicates the reluctances. Each black node has a MMF value, which is similar as the node voltage in electric circuit. The flux can flow in both vertical (y) direction and horizontal (x) direction through the element. If the MMFs on the nodes and the reluctances are known, it is very easy to calculate the flux flowing through each reluctance. Each reluctance equals half of the total reluctance of the element in corresponding direction. For the simple square element in Fig. 42, the four reluctances are given by (39) and (40).

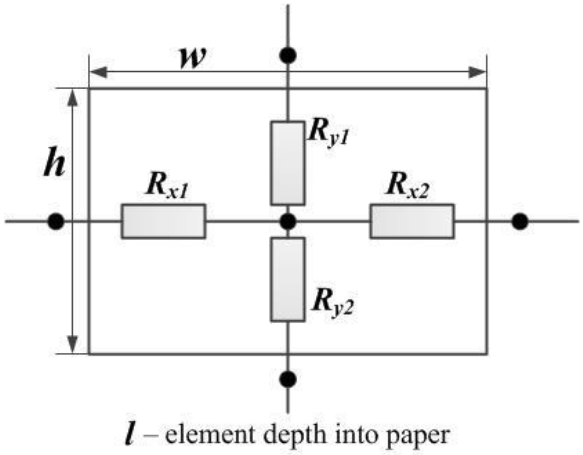

Fig. 42 A MEC element with two direction flux flow

$$R_x = \frac{w}{\mu_0 \mu_r hl} \qquad R_y = \frac{h}{\mu_0 \mu_r wl} \tag{39}$$

$$R_{x1} = R_{x2} = \frac{1}{2} R_x \qquad R_{y1} = R_{y2} = \frac{1}{2} R_y \tag{40}$$

Sometimes, the flux tube element does not have a rectangular shape, which requires additional calculations. The reluctances of common shapes of flux tubes in motor model are listed in the following figure, based on results of [39] [40]. The dark gray arrow in each flux tube indicates the flux flow direction. These equations are very useful in the motor model.

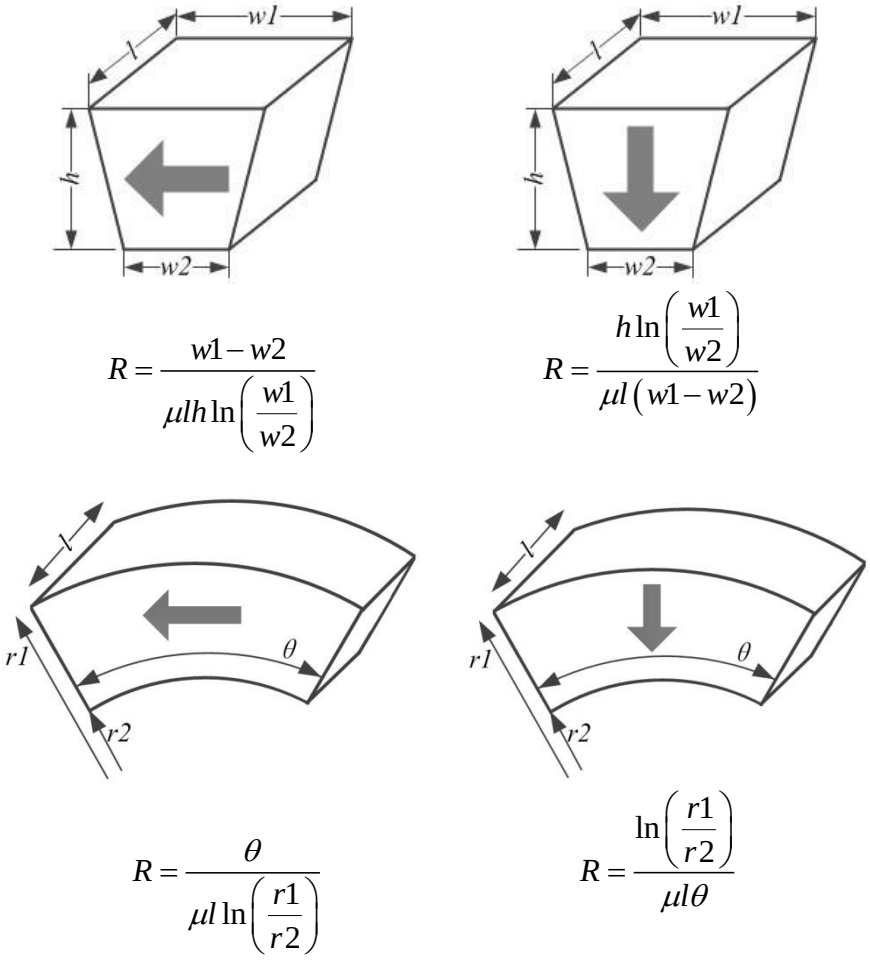

$$R = \frac{w1 - w2}{\mu l h \ln\left(\frac{w1}{w2}\right)}$$

$$R = \frac{h \ln\left(\frac{w1}{w2}\right)}{\mu l \left(w1 - w2\right)}$$

$$R = \frac{\theta}{\mu l \ln\left(\frac{r1}{r2}\right)}$$

$$R = \frac{\ln\left(\frac{r1}{r2}\right)}{\mu l \theta}$$

Fig. 43 Flux tubes with irregular shapes

However, for the stator/rotor core material (such as steel), it is not easy to just calculate reluctances since its permeability changes with the flux density inside it. This nonlinear property is usually presented as B-H curve in Fig. 44. Based on Ampere's law for magnetic field, the MMF drop across an element can also be presented by (43) for a simple element as in Fig. 41. Thus for a nonlinear flux tube element, the MMF drop is a nonlinear function of the flux.

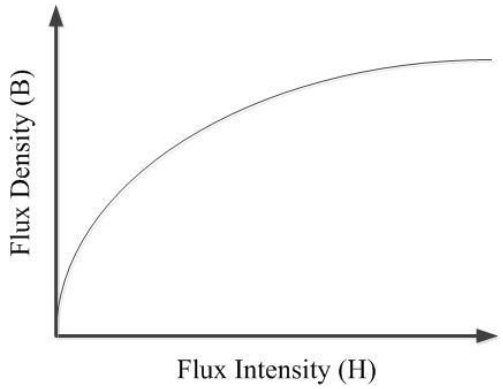

Fig. 44 Nonlinear B-H curve

$$MMFdrop = H \bullet l = f\left(B\right) \bullet l = f\left(\frac{\phi}{A}\right) \bullet l \tag{41}$$

The source of the MEC network is current. By Ampere's Law, the total MMF drop around a closed curve equals the total current enclosed in the curve. In Fig. 45, a stator slot with wires carrying current is shown. The number of wires inside the slot is ***N***, while each wire carries current ***I*** flowing into the paper. The closed loop $\mathscr{C}$ is shown in red. Then the total current enclosed in loop $\mathscr{C}$ is $N \bullet I$. Thus the Ampere's Law is expressed as (42). With (37) and (41), the term $\oint_c H \bullet dl$ can be replaced by the sum of MMF drop in the stator core elements and air gap elements.

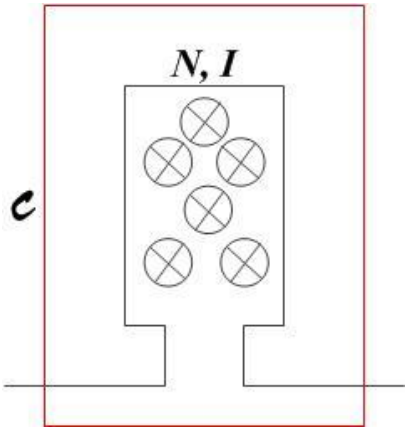

Fig. 45 Slot with current-carrying wires

$$\oint_c H \bullet dl = N \bullet I \tag{42}$$

The power source generated by current in MEC can be modeled similar as the voltage in electric circuit. It can be added to the elements next to the slot. Fig. 46 illustrates the power source added to the top (a) and side (b). Note the flux generated has a positive direction defined by right hand rule, indicated by the arrow inside the circle.

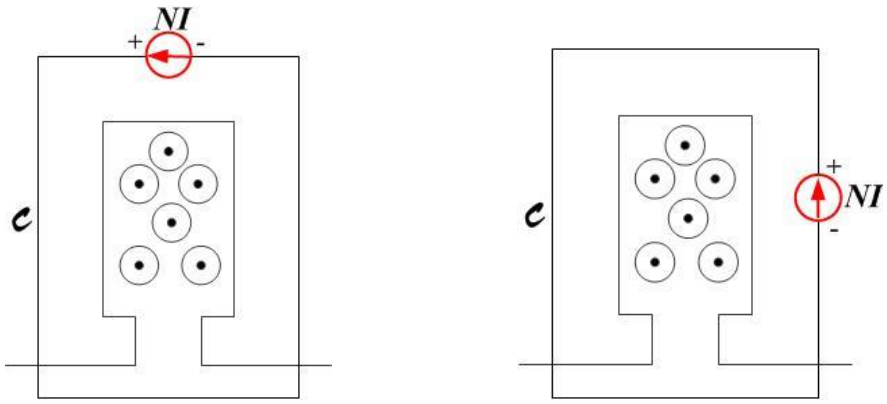

(a) (b)

Fig. 46 Placement of MMF in MEC

5.2 Induction Motor MEC Model

In [52], the motor is modeled with refined flux tube elements, which provides good results for simulating motor current, torque and etc. Just like FEM, the more elements the motor has, the more accurate the results. However, there is a tradeoff between accuracy and computation time. Thus in this paper, the number of flux tubes is reduced to be just enough to cover the main magnetic characteristics in both the stator/rotor core and air gap. The main idea of [52] is used here.

The proposed MEC element mesh is shown in Fig. 47. The dashed line indicates the boundary between elements. The air gap area is divided into two layers with same air gap length. One is attached to stator and kept stationary with time. The other one is attached to the rotor and rotates with rotor. The center line in the air gap is the boundary between stationary elements and moving elements. The interaction between the two layers will be illustrated in the next section.

To keep the model simple, only the shaded area was modeled. By the natural of magnetic fields, flux tends to go through a path with minimum reluctance. The slot area with windings has a relative big reluctance compared to the adjacent core area, which means few flux lines go pass through the slots area. Thus these slot area are not modeled for simplicity. However, the slot opening area is modeled for flux leakage and fringing, which also helps on define the air gap radial and tangential flux.

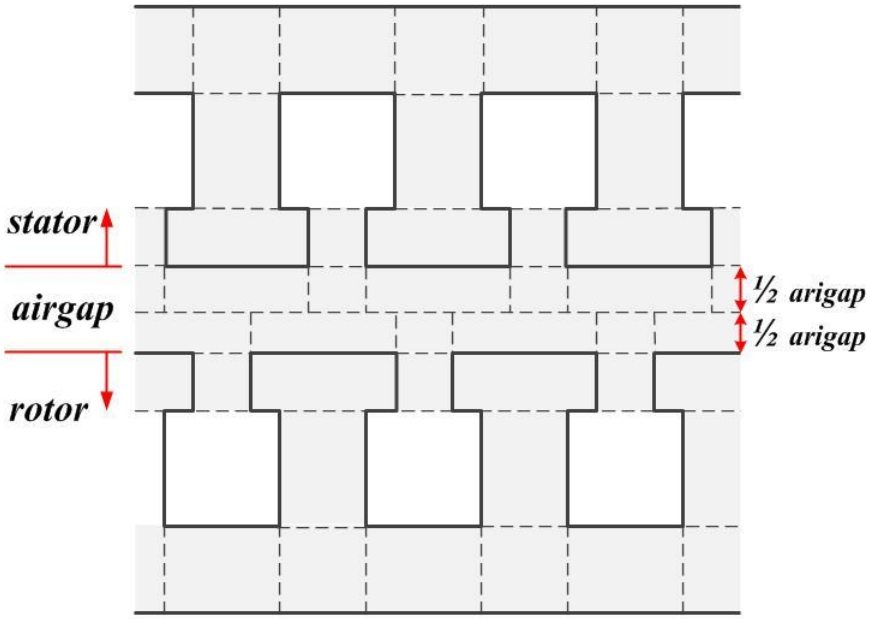

Fig. 47 Proposed MEC meshes

The final MEC model is presented in Fig. 48. Model variables and their positive directions are also defined. The black blocks indicate nonlinear reluctance in the core material, while the white ones indicate linear reluctance in air gap. The gray ones are

reluctances in air gap connecting the stationary and moving parts, which change with time. The calculation of these time changing reluctances is illustrated in the next section. Note the linear reluctances (white blocks) near the rotor side also changes with rotor position. This is because the rotor is eccentric. For a different rotor position, the air gap length is different.

The reluctance in horizontal direction indicates the radial component in motor, while the reluctance in vertical direction indicates the tangential component in motor. Now, the air gap contains both radial and tangential reluctance, which means the flux flow in both directions can be found.

In stator and rotor core material, fluxes are used as state variables due to the nonlinear B-H curve and permeability. In the air gap region, magnetic scalar potential are used as variables. The relative scalar potential between two nodes gives the MMF drop across the reluctance connecting these two nodes. The subscript definitions are listed below.

s – stator side variable

r (first) – rotor side variable

y – yoke area variable

t – teeth area variable

p – variable under pole area

g – airgap area variable

r (second) – radial component

t – tangential component

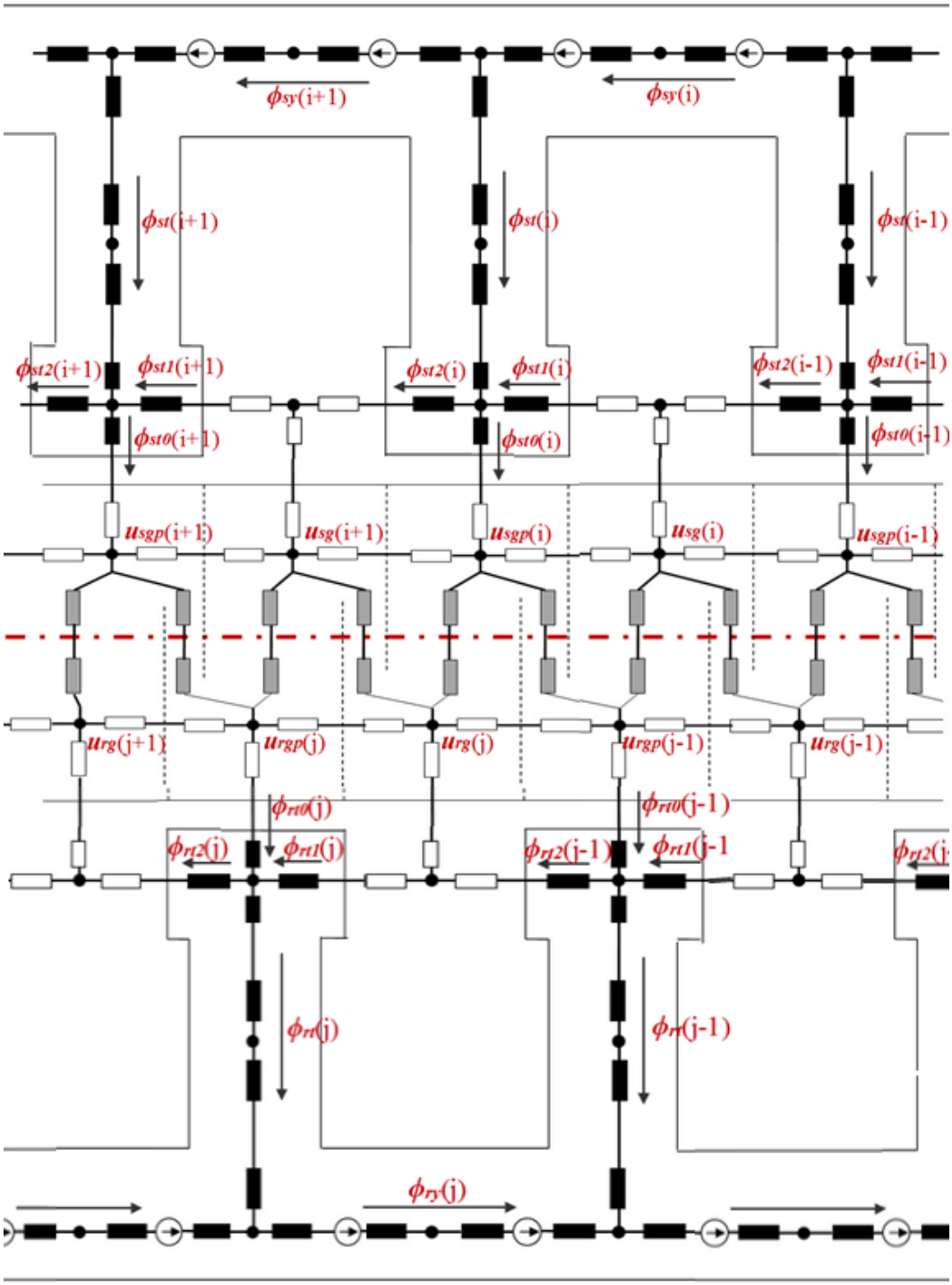

Fig. 48 MEC model

5.3 Air Gap Reluctance Calculation

The original meshed elements for air gap at a certain time point are shown in Fig. 49. To connect the stator side air gap and rotor side air gap, each reluctance around the boundary is divided into two parallel parts, according to the area overlapped with adjacent rotor side air gap elements [52]. Fig. 50 illustrates an example for the *i*th stator side air gap element under the pole area. The original reluctance $R_{sgpr}(i)$ becomes two parts, $R_{sgpr1}(i)$ and $R_{sgpr2}(i)$, which have overlaps with the *j*th rotor side air gap element under slot opening area and the *j-1*th rotor side air gap element under pole area, respectively. Note according to (38), reluctances are proportional to the inverse of the element cross area.

$$\begin{cases} R_{sgpr}(i) = \dfrac{R_{sgpr1}(i) R_{sgpr2}(i)}{R_{sgpr1}(i) + R_{sgpr2}(i)} \\ \dfrac{R_{sgpr1}(i)}{R_{sgpr2}(i)} = \dfrac{w_{s2}}{w_{s1}} \end{cases} \tag{43}$$

Do the same to the *j*th rotor side air gap element under slot opening area as in Fig. 51.

$$\begin{cases} R_{rgr}(j) = \dfrac{R_{rgr1}(j) R_{rgr2}(j)}{R_{rgr1}(j) + R_{rgr2}(j)} \\ \dfrac{R_{rgr1}(j)}{R_{rgr2}(j)} = \dfrac{w_{r2}}{w_{r1}} \end{cases} \tag{44}$$

Then the total reluctance connects the *i*th stator side air gap element under pole area and *j*th rotor side air gap element under slot opening area is given by

$$R_{sgprg}(i,j) = R_{sgpr1}(i) + R_{rgr2}(j) \tag{45}$$

Then connect all the reluctances near the moving boundary. Now in Fig. 52 all the elements in gray are defined, which are changing with rotor position and time.

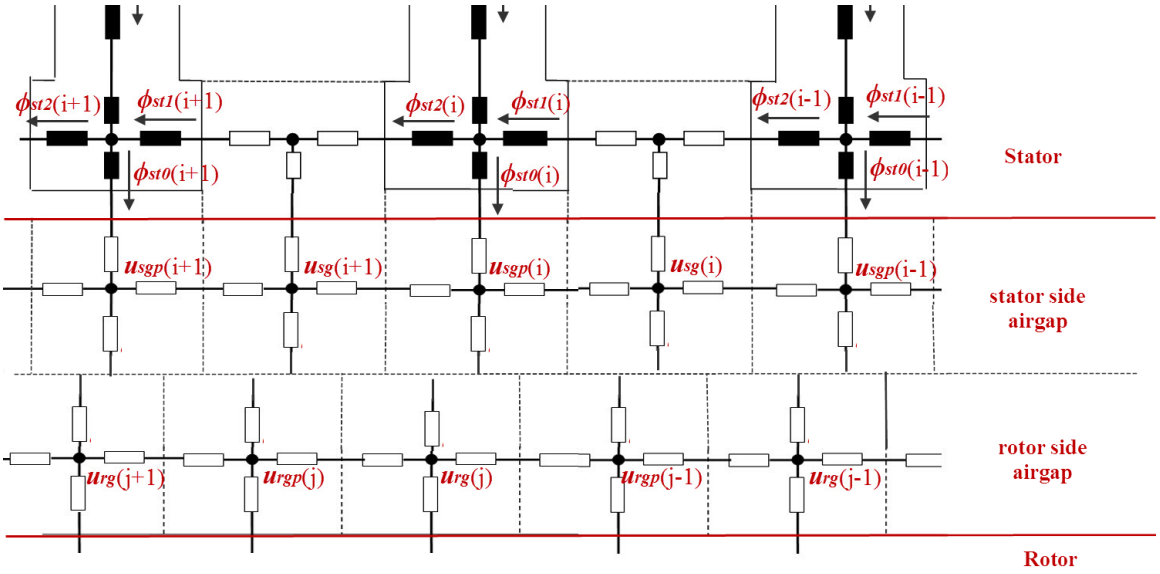

Fig. 49 Air gap original meshed elements

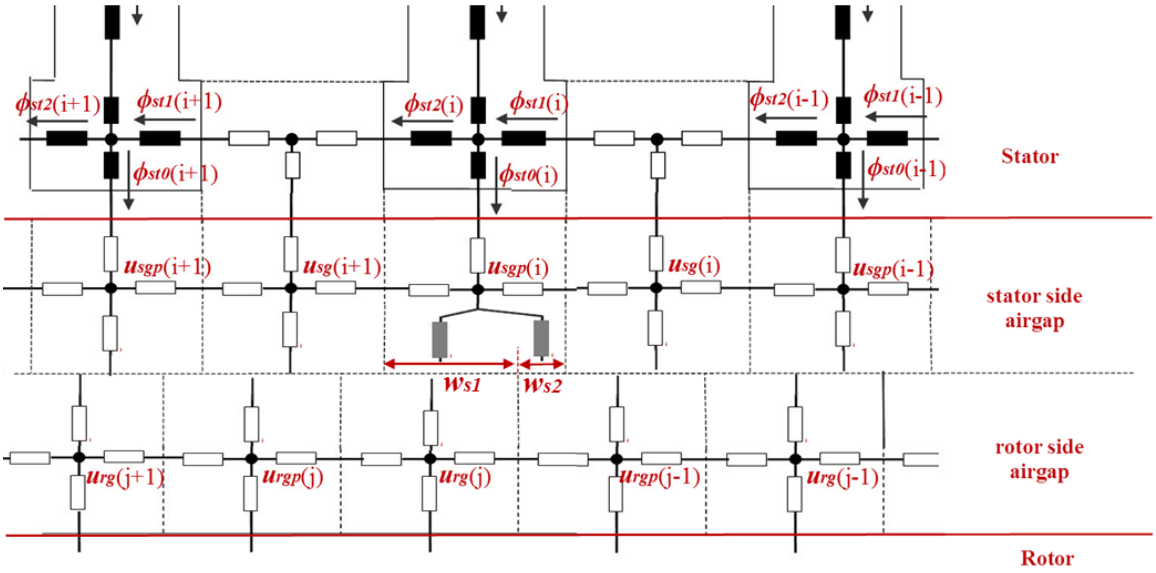

Fig. 50 *i*th stator side air gap element under the pole area

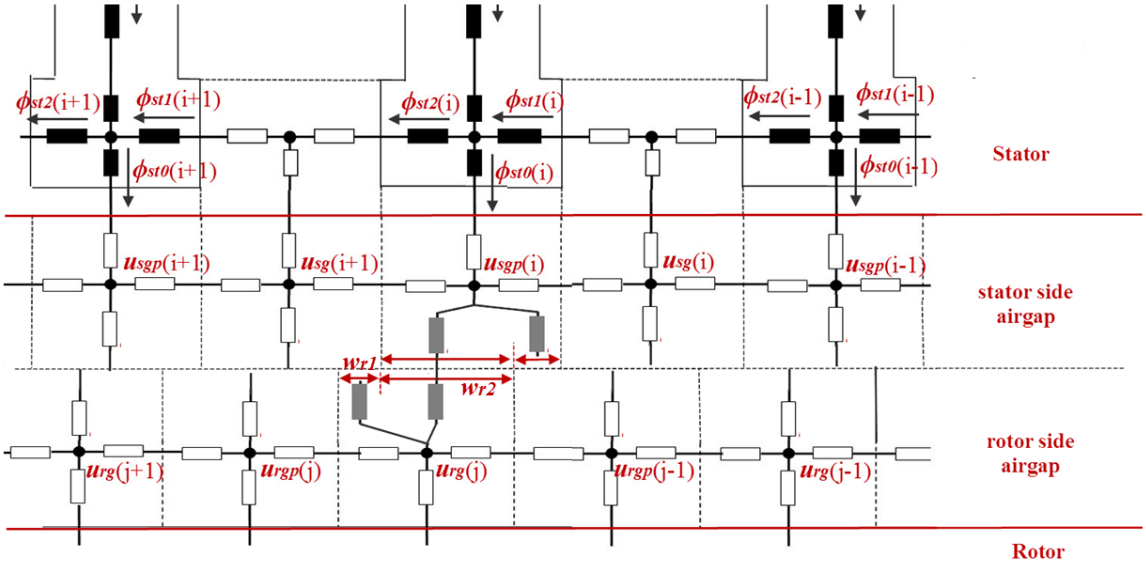

Fig. 51 *j*th rotor side air gap element under the slot area

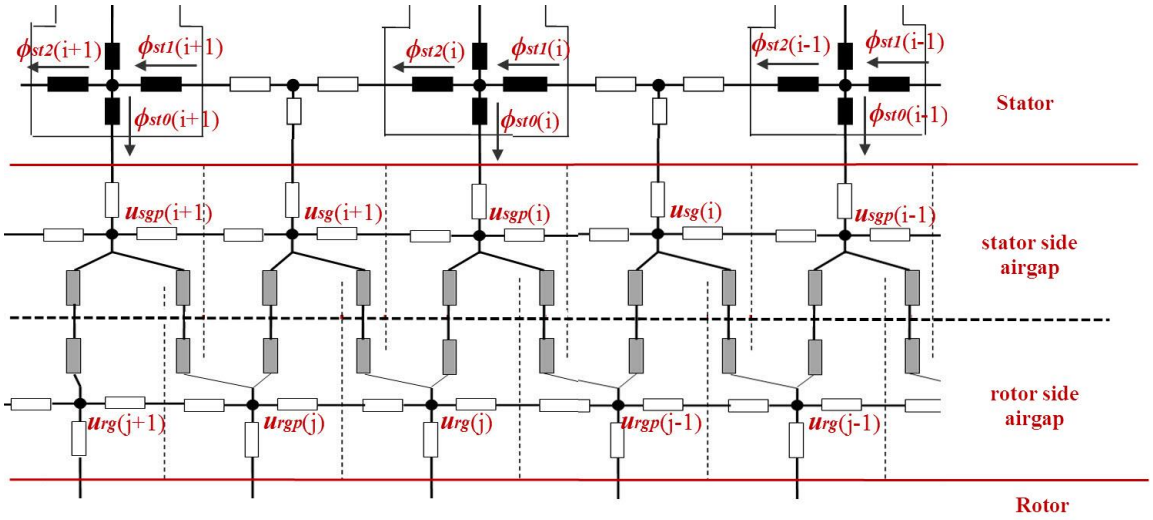

Fig. 52 Air gap reluctance on the moving boundary

5.4 MEC Model Equations

5.4.1 Stator Equations

Based on the model above, it is easy to write the equations for the MEC network. For stator region, by Kirchoff's current law in magnetic fields, write the equation for each node.

$$\phi_{st}(i)=\phi_{sy}(i)-\phi_{sy}(i+1) \tag{46}$$

$$\phi_{st}(i)+\phi_{st1}(i)=\phi_{st2}(i)+\phi_{st0}(i) \tag{47}$$

$$\phi_{sg}(i)=\phi_{st2}(i-1)-\phi_{st1}(i) \tag{48}$$

$$\phi_{st0}(i)+\frac{u_{sg}(i)-u_{sgp}(i)}{\frac{R_{sg\phi}(i)}{2}+\frac{R_{sgp\phi}(i)}{2}}+\frac{u_{sg}(i+1)-u_{sgp}(i)}{\frac{R_{sg\phi}(i+1)}{2}+\frac{R_{sgp\phi}(i)}{2}}+\sum_{j=1}^{nr}\frac{u_{rg}(j)-u_{sgp}(i)}{R_{sgprg}(i,j)}+\sum_{j=1}^{nr}\frac{u_{rgp}(j)-u_{sgp}(i)}{R_{sgprgp}(i,j)}=0 \tag{49}$$

$$\phi_{sg}(i)+\frac{u_{sgp}(i)-u_{sg}(i)}{\frac{R_{sg\phi}(i)}{2}+\frac{R_{sgp\phi}(i)}{2}}+\frac{u_{sgp}(i-1)-u_{sg}(i)}{\frac{R_{sg\phi}(i)}{2}+\frac{R_{sgp\phi}(i-1)}{2}}+\sum_{j=1}^{nr}\frac{u_{rg}(j)-u_{sg}(i)}{R_{sgrg}(i,j)}+\sum_{j=1}^{nr}\frac{u_{rgp}(j)-u_{sg}(i)}{R_{sgrgp}(i,j)}=0 \tag{50}$$

Than by Ampere's law in magnetic fields, write the equations for each loop.

$$l_{sy}H_{sy}(i)+l_{st}H_{st}(i)+l_{st00}H_{st00}(i)-l_{st}H_{st}(i-1)-l_{st00}H_{st00}(i-1)-l_{st1}H_{st1}(i)-l_{st2}H_{st2}(i-1)-\frac{R_{so\phi}}{2}\phi_{st1}(i)-\frac{R_{so\phi}}{2}\phi_{st2}(i-1)=mmfs(i) \tag{51}$$

$$u_{sg}(i)-u_{sgp}(i)+\left(R_{sor}+\frac{R_{sgr}(i)}{2}\right)\phi_{sg}(i)-\frac{R_{so\phi}}{2}\phi_{st1}(i)-l_{st1}H_{st1}(i)-l_{st0}H_{st0}(i)-\frac{R_{sgpr}(i)}{2}\phi_{st0}(i)=0 \tag{52}$$

$$u_{sg}(i)-u_{sgp}(i-1)+\left(R_{sor}+\frac{R_{sgr}(i)}{2}\right)\phi_{sg}(i)+\frac{R_{so\phi}}{2}\phi_{st2}(i-1)+l_{st2}H_{st2}(i-1)-l_{st0}H_{st0}(i-1)-\frac{R_{sgpr}(i-1)}{2}\phi_{st0}(i-1)=0 \tag{53}$$

Write the equations in matrix form.

$$\{\phi_{st}\}-\left([I_{ns}]-[A_{s0}]^T\right)\{\phi_{sy}\}=0 \tag{54}$$

$$\{\phi_{st}\}+\{\phi_{st1}\}-\{\phi_{st2}\}-\{\phi_{st0}\}=0 \tag{55}$$

$$-\{\phi_{st1}\}+[A_{s0}]\{\phi_{st2}\}-\{\phi_{sg}\}=0 \tag{56}$$

$$\{\phi_{st0}\}+\left[G_{sg1}\right]\{u_{sg}\}-\left[G_{sgp}\right]\{u_{sgp}\}+\left[G_{sgprg}\right]\{u_{rg}\}+\left[G_{sgprgp}\right]\{u_{rgp}\}=0 \tag{57}$$

$$\{\phi_{sg}\}-\left[G_{sg}\right]\{u_{sg}\}+\left[G_{sgp1}\right]\{u_{sgp}\}+\left[G_{sgrg}\right]\{u_{rg}\}+\left[G_{sgrgp}\right]\{u_{rgp}\}=0 \tag{58}$$

$$\begin{aligned}-\frac{R_{so\phi}}{2}\{\phi_{st1}\}-\frac{R_{so\phi}}{2}\left[A_{s0}\right]\{\phi_{st2}\}+l_{sy}\{H_{sy}\}+l_{st}\left(\left[I_{ns}\right]-\left[A_{s0}\right]\right)\{H_{st}\}\\ +l_{st00}\left(\left[I_{ns}\right]-\left[A_{s0}\right]\right)\{H_{st00}\}-l_{st1}\{H_{st1}\}-l_{st2}\left[A_{s0}\right]\{H_{st2}\}-\{mmfs\}=0\end{aligned} \tag{59}$$

$$\begin{aligned}-\frac{R_{so\phi}}{2}\{\phi_{st1}\}-\left[R_{sgpr0}\right]\{\phi_{st0}\}+\left(R_{sor}\left[I_{ns}\right]+\left[R_{sgr0}\right]\right)\{\phi_{sg}\}+\{u_{sg}\}-\{u_{sgp}\}-l_{st1}\{H_{st1}\}\\ -l_{st0}\{H_{st0}\}=0\end{aligned} \tag{60}$$

$$\begin{aligned}\frac{R_{so\phi}}{2}\left[A_{s0}\right]\{\phi_{st2}\}-\left[A_{s0}\right]\left[R_{sgpr0}\right]\{\phi_{st0}\}+\left(R_{sor}\left[I_{ns}\right]+\left[R_{sgr0}\right]\right)\{\phi_{sg}\}+\{u_{sg}\}\\ -\left[A_{s0}\right]\{u_{sgp}\}+l_{st2}\left[A_{s0}\right]\{H_{st2}\}-l_{st0}\left[A_{s0}\right]\{H_{st0}\}=0\end{aligned} \tag{61}$$

where

$$\left[A_{s0}\right]=\begin{bmatrix}&&&&1\\1&&&&\\&1&&&\\&&1&&\\&&&1&\end{bmatrix}$$

$$G_{sg}(i,i)=\frac{1}{\frac{R_{sg\phi}(i)}{2}+\frac{R_{sgp\phi}(i)}{2}}+\frac{1}{\frac{R_{sg\phi}(i)}{2}+\frac{R_{sgp\phi}(i-1)}{2}}+\sum_{j=1}^{nr}\frac{1}{R_{sgrg}(i,j)}+\sum_{j=1}^{nr}\frac{1}{R_{sgrgp}(i,j)}$$

$$G_{sgp}(i,i)=\frac{1}{\frac{R_{sg\phi}(i)}{2}+\frac{R_{sgp\phi}(i)}{2}}+\frac{1}{\frac{R_{sg\phi}(i+1)}{2}+\frac{R_{sgp\phi}(i)}{2}}+\sum_{j=1}^{nr}\frac{1}{R_{sgprg}(i,j)}+\sum_{j=1}^{nr}\frac{1}{R_{sgprgp}(i,j)}$$

$$\left[G_{sg1}\right]=\begin{bmatrix} \frac{1}{\frac{R_{sg\phi}(1)}{2}+\frac{R_{sgp\phi}(1)}{2}} & \frac{1}{\frac{R_{sg\phi}(2)}{2}+\frac{R_{sgp\phi}(1)}{2}} & & & \\ & \frac{1}{\frac{R_{sg\phi}(2)}{2}+\frac{R_{sgp\phi}(2)}{2}} & \frac{1}{\frac{R_{sg\phi}(3)}{2}+\frac{R_{sgp\phi}(2)}{2}} & & \\ & & \ddots & \ddots & \\ & & & \ddots & \\ \frac{1}{\frac{R_{sg\phi}(1)}{2}+\frac{R_{sgp\phi}(ns)}{2}} & & & & \frac{1}{\frac{R_{sg\phi}(ns)}{2}+\frac{R_{sgp\phi}(ns)}{2}} \end{bmatrix}$$

$$\left[G_{sgp1}\right]=\begin{bmatrix} \frac{1}{\frac{R_{sg\phi}(1)}{2}+\frac{R_{sgp\phi}(1)}{2}} & & & & \frac{1}{\frac{R_{sg\phi}(1)}{2}+\frac{R_{sgp\phi}(ns)}{2}} \\ \frac{1}{\frac{R_{sg\phi}(2)}{2}+\frac{R_{sgp\phi}(1)}{2}} & \frac{1}{\frac{R_{sg\phi}(2)}{2}+\frac{R_{sgp\phi}(2)}{2}} & & & \\ & \ddots & \ddots & & \\ & & \ddots & & \\ & & & \frac{1}{\frac{R_{sg\phi}(ns)}{2}+\frac{R_{sgp\phi}(ns-1)}{2}} & \frac{1}{\frac{R_{sg\phi}(ns)}{2}+\frac{R_{sgp\phi}(ns)}{2}} \end{bmatrix}$$

$$R_{sgr0}(i) = \frac{R_{sgr}(i)}{2}$$

$$R_{sgpr0}(i) = \frac{R_{sgpr}(i)}{2}$$

$$G_{sgprg}(i,j) = \frac{1}{R_{sgprg}(i,j)}$$

$$G_{sgprgp}(i,j) = \frac{1}{R_{sgprgp}(i,j)}$$

$$G_{sgrg}(i,j) = \frac{1}{R_{sgrg}(i,j)}$$

$$G_{sgrgp}(i,j) = \frac{1}{R_{sgrgp}(i,j)}$$

By flux conservation law, all flux going into a closed surface sums to zero. Thus all the stator teeth flux should sum to zero.

$$\begin{bmatrix} 1 & \underset{ns}{\cdots} & \cdots & 1 \end{bmatrix} \{\phi_{st}\} = 0 \tag{62}$$

5.4.2 Rotor Equations

Note the magnetic scalar potential is not an absolute quantity. There should be a zero reference point. For simplicity, set the last rotor side node to zero.

$$\{u_{rgp}\}(nr) = 0 \tag{63}$$

Similar as the stator, a set of equations can be obtained for the rotor side MEC.

$$\{\phi_{rt}\} - \left([I_{nr}] - [A_{r0}]^T \right) \{\phi_{ry}\} = 0 \tag{64}$$

$$\{\phi_{rt}\}-\{\phi_{rt1}\}+\{\phi_{rt2}\}-\{\phi_{rt0}\}=0 \tag{65}$$

$$\{\phi_{rt1}\}-[A_{r0}]\{\phi_{rt2}\}-\{\phi_{rg}\}=0 \tag{66}$$

$$\{\phi_{rt0}\}-[G_{rg1}]\{u_{rg}\}+[G_{rgp}]\{u_{rgp}\}-[G_{sgrgp}]^T\{u_{sg}\}-[G_{sgprgp}]^T\{u_{sgp}\}=0 \tag{67}$$

$$\{\phi_{rg}\}+[G_{rg}]\{u_{rg}\}-[G_{rgp1}]\{u_{rgp}\}-[G_{sgrg}]^T\{u_{sg}\}-[G_{sgprg}]^T\{u_{sgp}\}=0 \tag{68}$$

$$\begin{aligned}&\frac{R_{ro\phi}}{2}\{\phi_{rt1}\}+\frac{R_{ro\phi}}{2}[A_{r0}]\{\phi_{rt2}\}+l_{ry}\{H_{ry}\}+l_{rt}([I_{nr}]-[A_{r0}])\{H_{rt}\}\\&+l_{rt00}([I_{nr}]-[A_{r0}])\{H_{rt00}\}+l_{rt1}\{H_{rt1}\}+l_{rt2}[A_{r0}]H_{rt2}=\{mmfr\}\end{aligned} \tag{69}$$

$$\begin{aligned}&-\left(R_{ror}[I_{nr}]+[R_{rgr0}]\right)\{\phi_{rg}\}-\frac{R_{ro\phi}}{2}\{\phi_{rt1}\}+[R_{rgpr0}]\{\phi_{rt0}\}+\{u_{rg}\}-\{u_{rgp}\}-l_{rt1}\{H_{rt1}\}\\&+l_{rt0}\{H_{rt0}\}=0\end{aligned} \tag{70}$$

$$\begin{aligned}&\{u_{rg}\}-[A_{r0}]\{u_{rgp}\}-\left(R_{ror}[I_{nr}]+[R_{rgr0}]\right)\{\phi_{rg}\}+\frac{R_{ro\phi}}{2}[A_{r0}]\{\phi_{rt2}\}\\&+[A_{r0}][R_{rgpr0}]\{\phi_{rt0}\}+l_{rt2}[A_{r0}]\{H_{rt2}\}+l_{rt0}[A_{r0}]\{H_{rt0}\}=0\end{aligned} \tag{71}$$

$$[1\ \underset{nr}{\cdots}\ \cdots\ 1]\{\phi_{rt}\}=0 \tag{72}$$

where

$$[A_{r0}]=\begin{bmatrix}&&&&1\\1&&&&\\&1&&&\\&&\ddots&&\\&&&1&\end{bmatrix}$$

$$G_{rg}(j,j)=\frac{1}{\frac{R_{rg\phi}(j)}{2}+\frac{R_{rgp\phi}(j)}{2}}+\frac{1}{\frac{R_{rg\phi}(j)}{2}+\frac{R_{rgp\phi}(j-1)}{2}}+\sum_{i=1}^{ns}\frac{1}{R_{sgrg}(i,j)}+\sum_{i=1}^{ns}\frac{1}{R_{sgprg}(i,j)}$$

$$G_{rgp}(j,j)=\frac{1}{\frac{R_{rg\phi}(j)}{2}+\frac{R_{rgp\phi}(j)}{2}}+\frac{1}{\frac{R_{rg\phi}(j+1)}{2}+\frac{R_{rgp\phi}(j)}{2}}+\sum_{i=1}^{ns}\frac{1}{R_{sgrgp}(i,j)}+\sum_{i=1}^{ns}\frac{1}{R_{sgprgp}(i,j)}$$

$$\left[G_{rg1}\right]=\begin{bmatrix}\frac{1}{\frac{R_{rg\phi}(1)}{2}+\frac{R_{rgp\phi}(1)}{2}} & \frac{1}{\frac{R_{rg\phi}(2)}{2}+\frac{R_{rgp\phi}(1)}{2}} & & & \\ & \frac{1}{\frac{R_{rg\phi}(2)}{2}+\frac{R_{rgp\phi}(2)}{2}} & \frac{1}{\frac{R_{rg\phi}(3)}{2}+\frac{R_{rgp\phi}(2)}{2}} & & \\ & & \ddots & \ddots & \\ & & & \ddots & \\ \frac{1}{\frac{R_{rg\phi}(1)}{2}+\frac{R_{rgp\phi}(nr)}{2}} & & & & \frac{1}{\frac{R_{rg\phi}(nr)}{2}+\frac{R_{rgp\phi}(nr)}{2}}\end{bmatrix}$$

$$\left[G_{rgp1}\right]=\begin{bmatrix}\frac{1}{\frac{R_{rg\phi}(1)}{2}+\frac{R_{rgp\phi}(1)}{2}} & & & & \frac{1}{\frac{R_{rg\phi}(1)}{2}+\frac{R_{rgp\phi}(nr)}{2}} \\ \frac{1}{\frac{R_{rg\phi}(2)}{2}+\frac{R_{rgp\phi}(1)}{2}} & \frac{1}{\frac{R_{rg\phi}(2)}{2}+\frac{R_{rgp\phi}(2)}{2}} & & & \\ & \ddots & & & \\ & & \ddots & & \\ & & & \frac{1}{\frac{R_{rg\phi}(nr)}{2}+\frac{R_{rgp\phi}(nr-1)}{2}} & \frac{1}{\frac{R_{rg\phi}(nr)}{2}+\frac{R_{rgp\phi}(nr)}{2}}\end{bmatrix}$$

$$R_{rgr0}(j)=\frac{R_{rgr}(j)}{2}$$

$$R_{rgpr0}(j)=\frac{R_{rgpr}(j)}{2}$$

5.5 Eccentric Force Calculation

There are mainly two ways to calculate the electromagnetic force. One is energy method and the other one is using Maxwell stress tensor. In [50] and [51], energy method is used. In [52], Maxwell stress tensor is used. The energy method requires solve the nonlinear equations a second time to get an energy incensement while changing the target part's position with a small amount or calculate the Jacobian matrix. Due to the large size of the equations and the nonlinearity, Maxwell stress tensor method is preferred in this paper.

The radial and tangential Maxwell stress tensors are given by the following equations. The radial and tangential flux densities are all calculated in the air gap, which are functions of the circumferential coordinate.

$$\sigma_r=\frac{B_r^2}{2\mu_0} \tag{73}$$

$$\sigma_t=\frac{B_rB_t}{\mu_0} \tag{74}$$

The forces in x and y directions are calculated using the stress tensor.

$$F_x=rl\int_0^{2\pi}\left(\sigma_r\cos(\theta)-\sigma_t\sin(\theta)\right)d\theta \tag{75}$$

$$F_y = rl\int_0^{2\pi}\left(\sigma_r \sin(\theta) + \sigma_t \cos(\theta)\right)d\theta \tag{76}$$

5.6 Electric Circuit Model

The electric circuit model for motors is traditional three phase circuit model. Note in motor eccentric case, the current flowing through the parallel connected winding branches can be unbalanced. This requires modeling each stator parallel winding separately, in order to count for the current different in each winding branch. For squirrel cage rotor, each bar should be modeled separately since each bar carries a different current. In this paper, series connected stator windings are considered for simplicity. Using of parallel connected windings can help reduce the eccentric force [26]. More parallel winding effects are studied in [26].

5.6.1 Stator Electric Circuit Model

The following equations describe the stator winding all connected in series. The leakage inductance is ignored since it is small compared to the mutual inductance.

$$\begin{cases} v_a = r_s i_a + \dfrac{d\psi_a}{dt} \\ v_b = r_s i_b + \dfrac{d\psi_b}{dt} \\ v_c = r_s i_c + \dfrac{d\psi_c}{dt} \end{cases} \tag{77}$$

Where V_a , V_b, V_c are the stator phase terminal voltages; i_a, i_b, i_c are the stator phase currents; ψ_a, ψ_b, ψ_c are the stator phase flux linkages; r_s and l_{ls} are stator resistance per phase and leakage inductance per phase, respectively.

Write the stator electric circuit equations in matrix form and use the relationship between flux linkage and teeth flux.

$$\frac{d}{dt}\begin{Bmatrix}\psi_a\\ \psi_b\\ \psi_c\end{Bmatrix}=\begin{Bmatrix}v_a\\ v_b\\ v_c\end{Bmatrix}-R_s\begin{Bmatrix}i_a\\ i_b\\ i_c\end{Bmatrix} \tag{78}$$

where $R_s=\begin{bmatrix}r_s & & \\ & r_s & \\ & & r_s\end{bmatrix}$.

5.6.2 Rotor Electric Circuit Model

For rotor side, the loop currents are used, as shown in Fig. 53, which is the top view of the rotor bar. The loop goes around a rotor tooth. Then the electrical equation can be written for the loop. Note the rotor loop current positive direction is selected to be consistent with the rotor teeth flux direction.

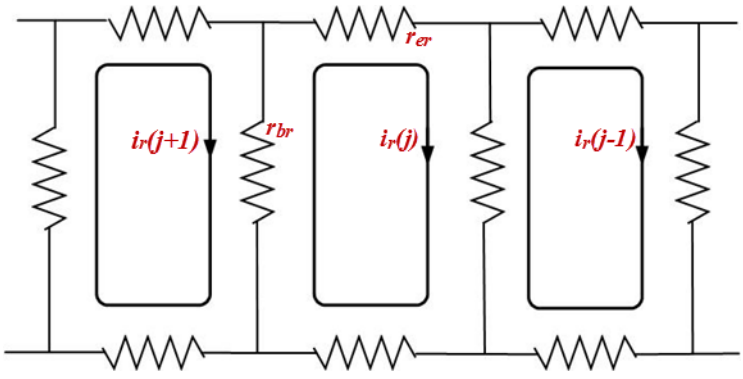

Fig. 53 Rotor loop currents

$$\frac{d\phi_{rt}(j)}{dt} = \left(2r_{br} + 2r_{er}\right) i_r^j - r_{br}\left(i_r^{j+1} + i_r^{j-1}\right) \tag{79}$$

where $\phi_{rt}(j)$ is the flux flowing through the *j*th rotor teeth; r_{br} and r_{er} are the resistance of the each bar and end ring segment of the squirrel cage, respectively.

By flux conservation law, all rotor teeth flux sums to zero, which means all rotor loop currents sum to zero.

$$\begin{Bmatrix} \phi_{rt}(1) \\ \phi_{rt}(2) \\ \vdots \\ \phi_{rt}(nr) \end{Bmatrix} = A_{rt} \begin{Bmatrix} \phi_{rt}(1) \\ \phi_{rt}(2) \\ \vdots \\ \phi_{rt}(nr\text{-}1) \end{Bmatrix} \tag{80}$$

$$\begin{Bmatrix} i_r(1) \\ i_r(2) \\ \vdots \\ i_r(nr) \end{Bmatrix} = A_{rt} \begin{Bmatrix} i_r(1) \\ i_r(2) \\ \vdots \\ i_r(nr\text{-}1) \end{Bmatrix} \tag{81}$$

where $A_{\substack{rt \\ nr\times(nr-1)}} = \begin{bmatrix} 1 & & & \\ & 1 & & \\ & & \ddots & \\ & & & 1 \\ -1 & -1 & -1 & -1 \end{bmatrix}$.

Then only *nr-1* rotor currents are independent variables and only *nr-1* rotor equations are needed. Write the rotor electric circuit equations in matrix form for the first *nr-1* equations.

$$\frac{d}{dt}\begin{Bmatrix} \phi_{rt}(1) \\ \phi_{rt}(2) \\ \vdots \\ \phi_{rt}(nr-1) \end{Bmatrix} = -\underset{(nr-1)\times nr}{R_r}\ \underset{nr\times(nr-1)}{A_{rt}} \begin{Bmatrix} i_r(1) \\ i_r(2) \\ \vdots \\ i_r(nr-1) \end{Bmatrix} \tag{82}$$

where $\underset{(nr-1)\times nr}{R_r} = \begin{bmatrix} 2r_{br}+2r_{er} & -r_{br} & \cdots & -r_{br} \\ -r_{br} & 2r_{br}+2r_{er} & \cdots & 0 \\ \vdots & \ddots & \ddots & 0 \\ 0 & \cdots & 2r_{br}+2r_{er} & -r_{br} \end{bmatrix}$.

5.6.3 Stator and Rotor Electric Circuit

Combine the stator and rotor electric circuit model equations (78) and (82), the following equations can be obtained.

$$\begin{bmatrix} \underset{3\times3}{I} & \underset{3\times(nr-1)}{0} \\ \underset{(nr-1)\times3}{0} & \underset{(nr-1)\times(nr-1)}{I} \end{bmatrix} \frac{d}{dt} \begin{Bmatrix} \psi_a \\ \psi_b \\ \psi_c \\ \phi_{rt}(1) \\ \vdots \\ \phi_{rt}(nr-1) \end{Bmatrix} =$$

$$\begin{bmatrix} 1 & 0 & 0 \\ 0 & 1 & 0 \\ 0 & 0 & 1 \\ 0 & 0 & 0 \\ 0 & 0 & 0 \\ \vdots & \vdots & \vdots \\ 0 & 0 & 0 \end{bmatrix} \begin{Bmatrix} v_a \\ v_b \\ v_c \end{Bmatrix} - \begin{bmatrix} \underset{3\times3}{R_s} & \underset{3\times(nr-1)}{0} \\ \underset{(nr-1)\times3}{0} & \underset{(nr-1)\times nr}{R_r}\ \underset{nr\times(nr-1)}{A_{rt}} \end{bmatrix} \begin{Bmatrix} i_a \\ i_b \\ i_c \\ i_r(1) \\ i_r(2) \\ \vdots \\ i_r(nr-1) \end{Bmatrix} \tag{83}$$

5.7 Coupling of MEC and Electric Circuit Models

In the MEC model, variables are stator and rotor fluxes and MMFs; while in the electric circuit model, variables are stator and rotor currents, stator flux linkages and rotor teeth fluxes. To couple the two field models, the relationships are required between variables of MEC model and electric model. The coupling equations in this section are combined with the MEC model as a set of equations with both linear and nonlinear equations.

5.7.1 Stator Flux Linkages

The stator flux linkages are related to the magnetic field distribution. It is defined as the total flux linked by a coil. Thus, the stator flux linkages are functions of the stator teeth flux. The relationship can be expressed as (84) [39][44][45][52].

$$\begin{cases} \psi_a = W_a \phi_{st} \\ \psi_b = W_b \phi_{st} \\ \psi_c = W_c \phi_{st} \end{cases} \tag{84}$$

Where ϕ_{st} is a vector containing the stator teeth flux; W_a, W_b, W_c are winding function matrices of phase *A*, *B* and *C*.

Winding functions are the integral of winding density and varies with circumferential coordinate.

$$M(\theta) = \int \xi d\theta \tag{85}$$

For concentrated windings, a winding function is defined as the sum of number of coils N_i in all slots whose slot number is less than *n*. It is a function of slot number *n* for each stator phase winding. The average of a winding function is set to be zero.

$$W'(n) = \sum_{1}^{n} N_i \tag{86}$$

$$W(n) = W'(n) - \text{ave}\left(W'(n)\right) \tag{87}$$

Write the (85) in matrix form.

$$\begin{Bmatrix} \psi_a \\ \psi_b \\ \psi_c \end{Bmatrix} = \begin{bmatrix} W_a \\ W_b \\ W_c \end{bmatrix} \begin{Bmatrix} \phi_{st}(1) \\ \phi_{st}(2) \\ \vdots \\ \phi_{st}(ns) \end{Bmatrix} = \underset{3\times ns}{W} \begin{Bmatrix} \phi_{st}(1) \\ \phi_{st}(2) \\ \vdots \\ \phi_{st}(ns) \end{Bmatrix} \tag{88}$$

Similar as the rotor teeth fluxes, based on flux conservation law, all stator teeth flux sums to zero.

$$\begin{Bmatrix} \phi_{st}(1) \\ \phi_{st}(2) \\ \vdots \\ \phi_{st}(ns) \end{Bmatrix} = A_{st} \begin{Bmatrix} \phi_{st}(1) \\ \phi_{st}(2) \\ \vdots \\ \phi_{st}(ns\text{-}1) \end{Bmatrix} \tag{89}$$

Where $\underset{ns\times(ns-1)}{A_{st}} = \begin{bmatrix} 1 & & & \\ & 1 & & \\ & & \ddots & \\ & & & 1 \\ -1 & -1 & -1 & -1 \end{bmatrix}$.

Then,

$$\underset{3\times ns}{W}\ \underset{ns\times(ns-1)}{A_{st}}\begin{Bmatrix}\phi_{st}(1)\\ \phi_{st}(2)\\ \vdots\\ \phi_{st}(ns-1)\end{Bmatrix}-\begin{Bmatrix}\psi_a\\ \psi_b\\ \psi_c\end{Bmatrix}=0 \tag{90}$$

5.7.2 Stator and Rotor MMFs

The stator and rotor MMFs are related to the current flow in the slots of stator and in the rotor bar.

5.7.2.1 Stator MMFs

For stator, the MMFs due to phase *A* current is given as the following equation. For windings with parallel windings, each branch should have a separate equation.

$$mmfs_a = M_a \cdot i_a \tag{91}$$

where $mmfs_a$ is the stator MMF due to phase *A* current; M_a is the winding density function of phase *A*; i_a is the phase current (for series connected winding).

The winding density function is a function of slot number, describing the winding density. For concentrated windings, a winding density function is defined as the number of coils N in the *i*th slot. The winding function defined in (87) is the integral of the winding density function.

$$M(i) = N_i \tag{92}$$

Similar as phase *A* winding, the MMFs due to phase *B* and *C* can be obtained. The total stator MMFs are the sum of the MMFs generated from all three phase winding currents.

$$mmfs = mmfs_a + mmfs_b + mmfs_c = M_a \cdot i_a + M_b \cdot i_b + M_c \cdot i_c \tag{93}$$

$$mmfs = M \begin{Bmatrix} i_a \\ i_b \\ i_c \end{Bmatrix} \tag{94}$$

where $M = \begin{bmatrix} M_a & M_b & M_c \end{bmatrix}$.

5.7.2.2 Rotor MMFs

For squirrel cage rotor, there is no connected winding like stator. The MMFs are just related to each bar current.

$$mmfr(j) = i_r(j) - i_r(j-1) \tag{95}$$

Write the above equation in matric form and use the matrix definition in the rotor MEC model.

$$mmfr = \left(\begin{bmatrix} I_{nr} \end{bmatrix} - \begin{bmatrix} A_{r0} \end{bmatrix} \right) \begin{Bmatrix} i_r(1) \\ i_r(2) \\ \vdots \\ i_r(nr) \end{Bmatrix} \tag{96}$$

Based on (82), (97) can be written as

$$mmfr = \left(\begin{bmatrix} I_{nr} \end{bmatrix} - \begin{bmatrix} A_{r0} \end{bmatrix} \right) \begin{bmatrix} A_{rt} \end{bmatrix} \begin{Bmatrix} i_r(1) \\ i_r(2) \\ \vdots \\ i_r(nr-1) \end{Bmatrix} \tag{97}$$

5.8 Solve Coupled Magnetic and Electric Equations

The system model includes nonlinear MEC model and linear electric circuit model. The electric circuit model is a set of first order differential equations. To solve the transient, the following steps are taken [39][47], as shown in Fig. 54.

The entire system is modeled in Matlab and the nonlinear MEC equations are solved with the *fsolve* command [61]. The initial condition at the first step is obtained by assuming a universal permeability for the stator and rotor core material, and solving the linear equations. For each other step, the initial condition of the *fsolve* command is given by the field solution of the last time step.

Note this model can also be coupled with mechanical system to get a more complex system and simulate for dynamic eccentricity with torque calculation. That will be included in the future work since this paper is focused on eccentric force and its equivalent stiffness.

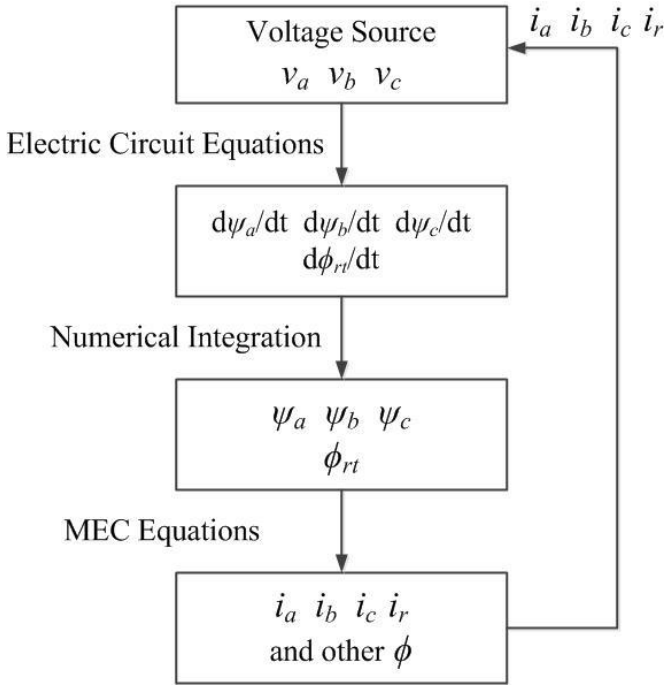

Fig. 54 Steps to solve coupled magnetic and electric equations

CHAPTER VI

INFLUENCE OF MOTOR ECCENTRICITY ON ROTORDYNAMICS

In order to study the influence of the motor eccentricity on mechanical vibrations, an 11 kW example induction motor is used. First, the proposed modeling method is validated by comparing with FEM (Ansys Maxwell). Then, the eccentric force is further studied and applied to a Jeffcott rotor model.

6.1 Example Motor

The example motor used in this dissertation is an 11 kW motor. The stator and rotor slot shapes are simplified as in Fig. 55. The motor parameters are listed in Tab. 12. The stator winding connections are listed in

Tab. 13.

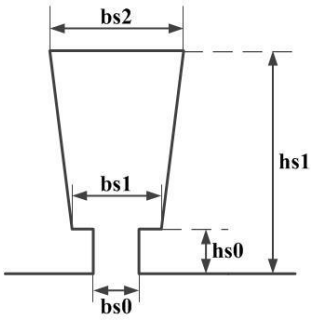

Fig. 55 Simplified slot shape

Tab. 12 Example induction motor parameters

General Information	
Output Power (kW)	11
Rated Voltage (V)	380
Rated Frequency (Hz)	50
Number of Poles	6
Motor Length (mm)	280
Stator Parameters	
Number of Slots	72
Outer Radius (mm)	163.5
Inner Radius (mm)	105
Slot hs0 (mm)	0.8
hs1 (mm)	44.9
bs0 (mm)	3
bs1 (mm)	4.8
bs2 (mm)	8.2
Winding Connection	Wye
Parallel Windings	1
Number of Conductor per Slot	6
Coil Pith	12 (full pitch)
Rotor Parameters	
Number of Slots	58
Air Gap (mm)	0.4
Outer Radius (m)	103.6
Inner Radius (m)	37.5
Slot hs0 (mm)	0.5
hs1 (mm)	17.165
bs0 (mm)	1
bs1 (mm)	3.3
bs2 (mm)	3.3
Per Phase Parameters	
Stator Resistance (Ohm)	0.297292
Stator Leakage Inductance (H)	0.0015428
Rotor Resistance (Ohm)	0.239188
Rotor Leakage Inductance (H)	0.0011368
Magnetizing Inductance (H)	0.030311
Mechanical Parameters	
Rotor Mass (kg)	64.3040

Tab. 13 Stator winding connections

Phase		Slot Number											
A	+	1	2	3	4	25	26	27	28	49	50	51	52
	-	13	14	15	16	37	38	39	40	61	62	63	64
B	+	9	10	11	12	33	34	35	36	57	58	59	60
	-	21	22	23	24	45	46	47	48	69	70	71	72
C	+	17	18	19	20	41	42	43	44	65	66	67	68
	-	29	30	31	32	53	54	55	56	5	6	7	8

6.2 Validation of Proposed Induction Motor Model

First, the proposed model is compared with FEM. Ansys Maxwell is used. The motor rotor is moved away from its center for 0.1 mm toward the x-axis direction, which is 25% eccentricity. The input voltage is the rated voltage 380 V L-L RMS. The FEM model is shown in Fig. 56 and the rotor speed is 977.876 rpm.

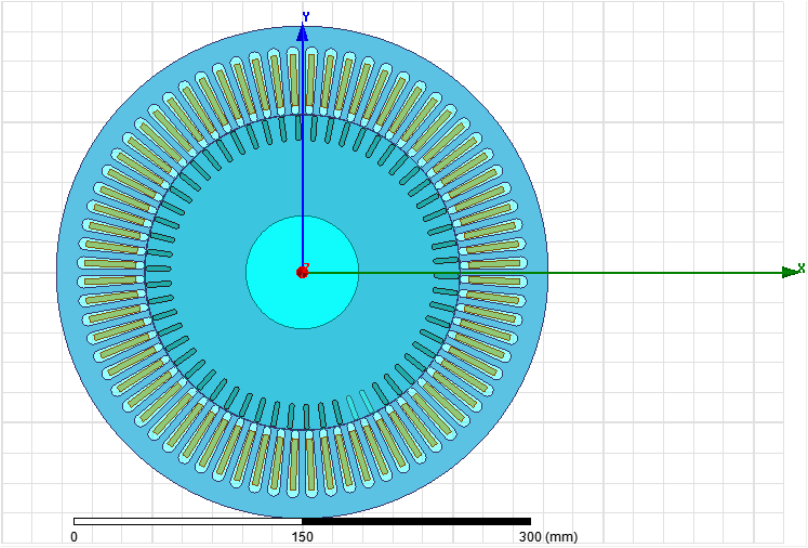

Fig. 56 Model in Ansys Maxwell

The air gap radial and tangential flux densities of the MEC model and the FEM model are compared in Fig. 57 and Fig. 58 at 50 ms. From the comparison, the air gap radial flux density predicted by the MEC model matches well with FEM model. In Fig. 58, FEM result indicates the air gap tangential flux density mainly exits in the slot opening region. However, based on the MEC mesh in Fig. 47 and Fig. 48, the air gap tangential flux density is calculated on an average way between two adjacent nodes with scalar magnetic potentials.

The radial and tangential forces are calculated using Maxwell stress tensor based on the air gap flux density values in Fig. 57 and Fig. 58. The MEC gives 533.2218 N in x-axis direction and 136.5094 N in y-axis direction, compared to FEM results 550 N and 100 N, respectively. Note in the model, the motor is eccentric in x-axis direction. Thus in this model, the radial eccentric force aligns in x-axis direction and the tangential eccentric force aligns in y-direction. The resultant x and y direction forces are just radial and tangential force.

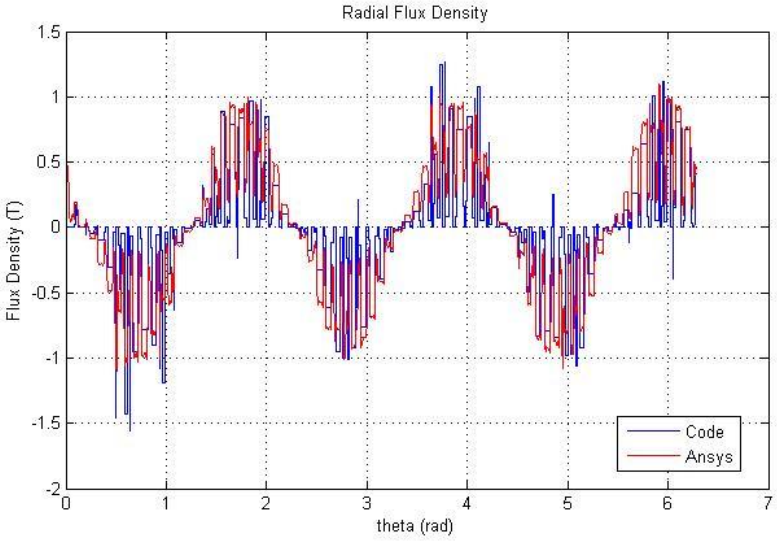

Fig. 57 Comparison of air gap radial flux density at 50 ms

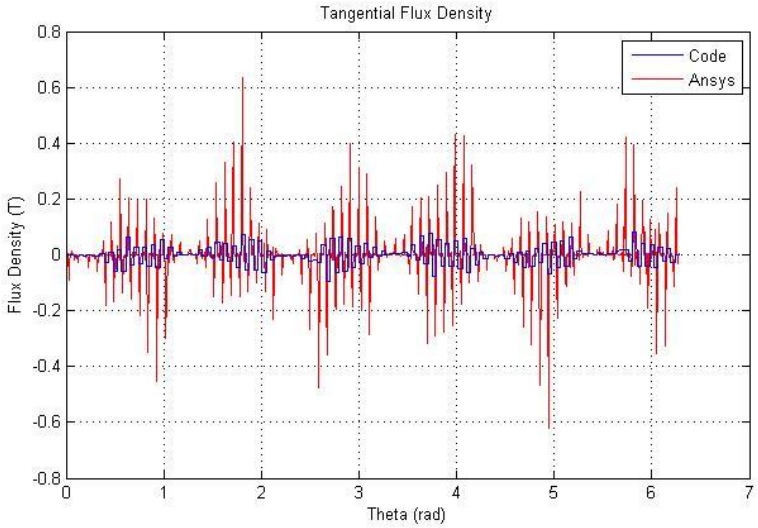

Fig. 58 Comparision of air gap tangential flux density at 50 ms

6.3 Parametric Study of Eccentric Force

Because of the nonlinearity of motors, the motor eccentric force changes with many parameters. In this section, the motor eccentricity, operation current, and designed

motor air gap length are considered. The results indicate the complexity of the eccentric force. Note as stated in the literatures, the eccentric force contains a constant component and time-varying components (harmonics). Only the characteristic of the constant component is discussed here because the time-varying components are relatively small. However, that is important for a dynamic eccentricity simulation for a complete motor-machinery train model.

6.3.1 Eccentricity

First, the motor eccentricity is changed from 0.05 mm (12.5% eccentricity) to 0.39 mm (97.5% eccentricity) for the example motor, while keeping the same supplied voltage (380 V and 50 Hz) and spin speed (977.876 rpm). The radial and tangential eccentric forces are shown in Fig. 59 with cubic curve fit for each curve. The radial stiffness increases with eccentricity with an increased slop, while the tangential force seems increase linearly.

Note this curve can be seen as valid for constant load torque operation even with changing spin speed. This is because the motor magnetic field depends on the stator/rotor current distribution. Under a constant torque operation, the motor almost maintains the same current level and the current distortion induced by eccentricity is relatively small due to the small air gap.

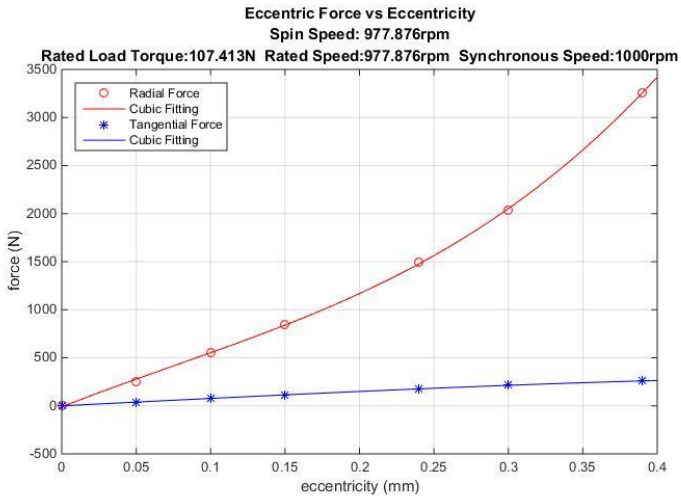

Fig. 59 Eccentric force vs eccenticity with input votlage 380 V L-L RMS and spin speed 977.876 rpm

6.3.2 Motor Input Voltage/Current

As mentioned before, the motor eccentric force varies with the motor operation condition. Since the stator current increases as the input voltage increases, the motor input voltage is varied for simplicity. For the example induction motor, the input voltage (L-L RMS) is changed from 151 V to 607.4735 V. The rotor eccentricity and spin speed are kept the same, which are 0.1 mm (25% eccentricity) and 977.876 rpm, respectively. The motor rated voltage is 380 V. Thus the voltages before that rated value have more practical meaning. A quadratic curve fitting is performed on both radial and tangential forces.

Before reaching the rated voltage, both radial and tangential forces increase with the input voltage and their slop tend to decrease. After the rated voltage, the radial force

continues to increase and approaches saturation. However, the tangential force decreases as the input voltage further increase.

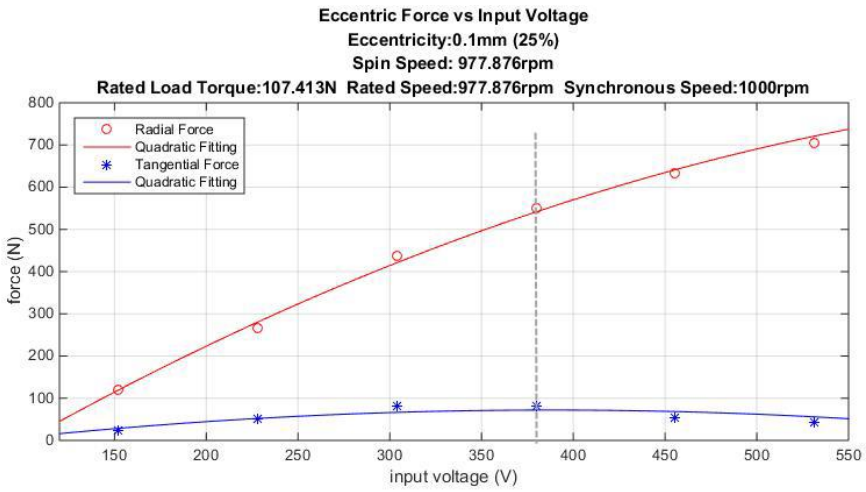

Fig. 60 Eccentric force vs input votage with eccentricity 0.1 mm and spin speed 977.876 rpm

6.3.3 Designed Air Gap

For the example motor, the designed air gap is 0.4 mm. Fig. 61 shows the change of eccentric force while varying the air gap value. The motor stator geometries and rotor slot geometries all stay the same. The only change is the motor original air gap length – the rotor outer radius is changed. The supplied voltage is kept the same (380 V L-L RMS) and so does the eccentricity (0.1 mm).

Based on the results, it indicates that with smaller designed motor air gap, both the radial and tangential forces get larger. This can be explained as with smaller air gap

design, the motor has a higher energy density stored in the air gap. Then the same eccentricity (unbalance) will cause a larger difference in force balance.

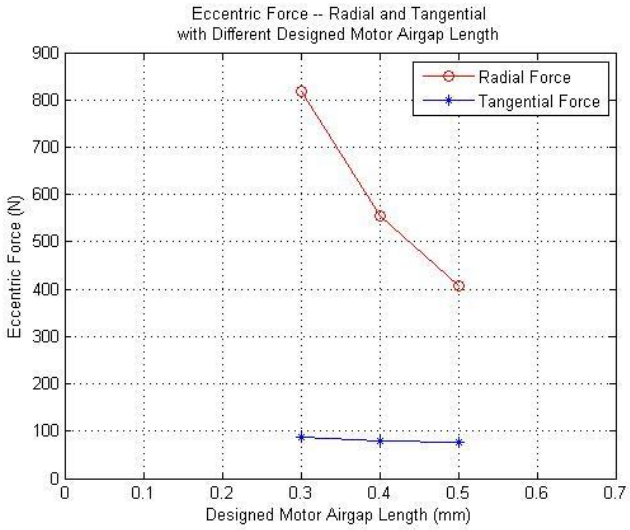

Fig. 61 Eccentric force vs designed motor air gap with input votlage 380 V L-L RMS, eccenticity 0.1 mm and spin speed 977.876 rpm

6.4 Influence of Motor Eccentric Force on System Stability

A simple Jeffcott rotor model (Fig. 62) is used to analysis the stability due to the motor eccentric forces. The bearing has a lateral motion stiffness *k* and a damping *c*. The equations of motions (EOM) of this simple model are as (98).

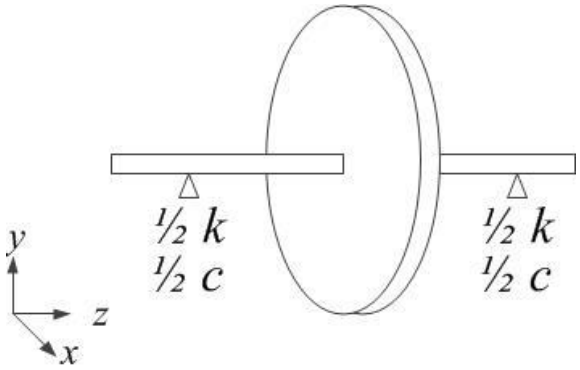

Fig. 62 Simple Jeffcott rotor model

$$\begin{cases} m\ddot{x} + c\dot{x} + kx = me_m\omega^2 \cos(\omega t) + F_x \\ m\ddot{y} + c\dot{y} + ky = me_m\omega^2 \sin(\omega t) + F_y \end{cases} \tag{98}$$

where m is the rotor mass; e_m is the mass unbalance; w is the rotor spin speed; t is time; F_x and F_y are rotor eccentric radial and tangential force, respectively; x and y are rotor lateral motions in x and y direction.

Write the EOM in matrix form.

$$\begin{bmatrix} m & 0 \\ 0 & m \end{bmatrix} \begin{Bmatrix} \ddot{x} \\ \ddot{y} \end{Bmatrix} + \begin{bmatrix} c & 0 \\ 0 & c \end{bmatrix} \begin{Bmatrix} \dot{x} \\ \dot{y} \end{Bmatrix} + \begin{bmatrix} k & 0 \\ 0 & k \end{bmatrix} \begin{Bmatrix} x \\ y \end{Bmatrix} = \begin{Bmatrix} me_m\omega^2 \cos(\omega t) \\ me_m\omega^2 \sin(\omega t) \end{Bmatrix} + \begin{Bmatrix} F_x \\ F_y \end{Bmatrix} \tag{99}$$

The motor eccentric force can be expressed with its equivalent eccentric stiffness, which is an average value among a certain analysis region.

$$\begin{cases} F_r = k_r e \\ F_t = k_t e \end{cases} \tag{100}$$

where k_r and k_t are average equivalent radial and tangential stiffness, respectively; e is the motor eccentricity.

The radial and tangential eccentric forces are in radial coordinate. Using the coordinate transform, the equivalent stiffness matrix in x-y coordinate can be obtained.

$$\begin{cases} F_x = F_r \cos(\theta) - F_t \sin(\theta) \\ F_y = F_r \sin(\theta) + F_t \cos(\theta) \end{cases} \tag{101}$$

$$\begin{cases} \cos(\theta) = \dfrac{x}{\sqrt{x^2 + y^2}} \\ \sin(\theta) = \dfrac{y}{\sqrt{x^2 + y^2}} \end{cases} \tag{102}$$

$$\begin{Bmatrix} F_x \\ F_y \end{Bmatrix} = K_{ec} \begin{Bmatrix} x \\ y \end{Bmatrix} \tag{103}$$

where $K_{ec} = \begin{bmatrix} k_r & -k_t \\ k_t & k_r \end{bmatrix}$.

The EOM becomes

$$M \begin{Bmatrix} \ddot{x} \\ \ddot{y} \end{Bmatrix} + C \begin{Bmatrix} \dot{x} \\ \dot{y} \end{Bmatrix} + K \begin{Bmatrix} x \\ y \end{Bmatrix} = \begin{Bmatrix} me\omega^2 \cos(\omega t) \\ me\omega^2 \sin(\omega t) \end{Bmatrix} \tag{104}$$

where $M = \begin{bmatrix} m & 0 \\ 0 & m \end{bmatrix}$; $C = \begin{bmatrix} c & 0 \\ 0 & c \end{bmatrix}$; $K = \begin{bmatrix} k - k_r & k_t \\ -k_t & k - k_r \end{bmatrix}$

For damped free vibration with no mass unbalance, and write the EOM in the form of first order differential equations. Let $V = \begin{Bmatrix} \dot{x} \\ \dot{y} \end{Bmatrix}$ and $X = \begin{Bmatrix} x \\ y \end{Bmatrix}$.

$$\begin{Bmatrix} \dot{X} \\ \dot{V} \end{Bmatrix} = \begin{bmatrix} 0 & I \\ -M^{-1}K & -M^{-1}C \end{bmatrix} \begin{Bmatrix} X \\ V \end{Bmatrix} \tag{105}$$

The eigenvalues of the above system are calculated as

$$\begin{cases} \lambda_1 = -\dfrac{1}{2m}\left(c + \sqrt{c^2 - 4km + 4k_r m + 4k_t mj}\right) \\ \lambda_2 = -\dfrac{1}{2m}\left(c + \sqrt{c^2 - 4km + 4k_r m - 4k_t mj}\right) \\ \lambda_3 = -\dfrac{1}{2m}\left(c - \sqrt{c^2 - 4km + 4k_r m + 4k_t mj}\right) \\ \lambda_4 = -\dfrac{1}{2m}\left(c - \sqrt{c^2 - 4km + 4k_r m - 4k_t mj}\right) \end{cases} \tag{106}$$

Let $c^2 - 4km + 4k_r m - 4k_t mj = (a - bj)^2$, then $c^2 - 4km + 4k_r m + 4k_t mj = (a + bj)^2$, where *a* and *b* are real positive numbers. Then,

$$\sqrt{c^2 - 4km + 4k_r m - 4k_t mj} = \begin{cases} a - bj \\ -a + bj \end{cases} \tag{107}$$

$$\sqrt{c^2 - 4km + 4k_r m + 4k_t mj} = \begin{cases} a + bj \\ -a - bj \end{cases} \tag{108}$$

The undamped natural frequencies and damping ratios can be calculated.

$$\omega_{n1}^2 = \left(\frac{c-a}{2m}\right)^2 + \left(\frac{b}{2m}\right)^2 \qquad \xi_1 = \left(\frac{c-a}{2m}\right)\frac{1}{\omega_{n1}} \tag{109}$$

$$\omega_{n2}^2 = \left(\frac{c+a}{2m}\right)^2 + \left(\frac{b}{2m}\right)^2 \qquad \xi_2 = \left(\frac{c+a}{2m}\right)\frac{1}{\omega_{n2}} \tag{110}$$

Since *a*, *b* and *c* are real and positive numbers, ξ_2 is guaranteed to be positive. However, ξ_1 can go negative when $c<a$. Thus for stability, it requires $c>a$.

By definition of *a* and *b*,

$$a^2 = \frac{\left(c^2 - 4km + 4k_r m\right) + \sqrt{\left(c^2 - 4km + 4k_r m\right)^2 + 4\left(2k_t m\right)^2}}{2} \tag{111}$$

Then $c>a$ requires

$$c^2 > \frac{\left(c^2 - 4km + 4k_r m\right) + \sqrt{\left(c^2 - 4km + 4k_r m\right)^2 + 4\left(2k_t m\right)^2}}{2} \tag{112}$$

After simplification, the system stability condition becomes

$$c^2 > \frac{mk_t^2}{k - k_r} \tag{113}$$

This can be illustrated in the damping ratio vs bearing damping plot, as shown in Fig. 63. In this plot, the motor is operating at 380 V L-L RMS and 977 rpm spin speed with 0.1 mm eccentricity. For different bearing stiffness, there is different critical bearing damping ratio, below which the system is unstable (negative system damping ratio). As shown in the figure, light damped bearings such as ball bearing are more like to be unstable with motor rotor eccentricity. However, for some cases, even large bearing damping is not enough to make the system stable.

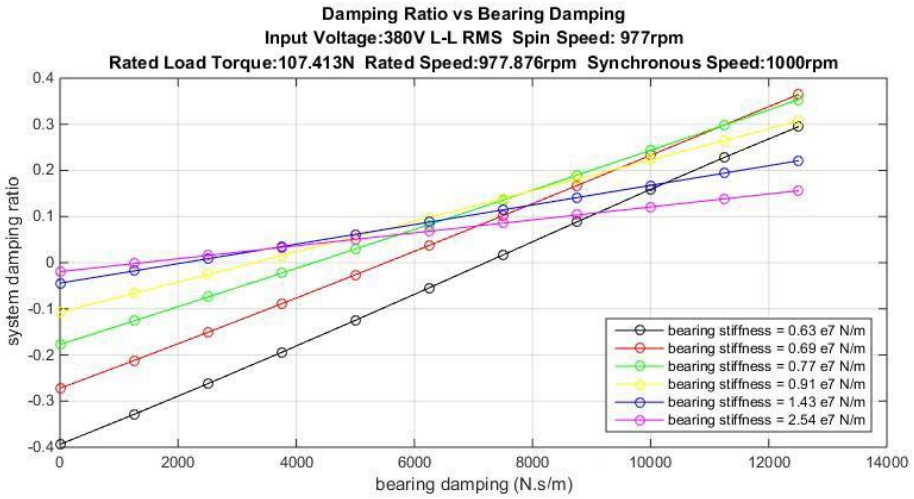

Fig. 63 System damping ratio vs bearing damping

6.5 System Nonlinearity due to Motor Eccentricity

In practice, motor rotor shaft may under dynamic eccentricity. The nonlinearity of the eccentric force induces nonlinear lateral motion in the system. For a motor under constant torque load, the motor eccentric force can be seem as only varying with eccentricity as discussed in Fig. 59. Then the force curves in Fig. 59 are valid for all cases with 107 N.m load torque. Using cubic curve fitting, the motor eccentric radial and tangential forces are approximated as Eqn. 59 with eccentricity e in unit mm. The fitted curve is shown in Fig. 64. This approximated force is used in the Jeffcott rotor model discussed above.

$$\begin{cases} F_r = 35982 \times e^3 - 8161 \times e^2 + 6085 \times e \\ F_t = -769.5175 \times e^3 + 21.172 \times e^2 + 773.4114 \times e \end{cases} \tag{114}$$

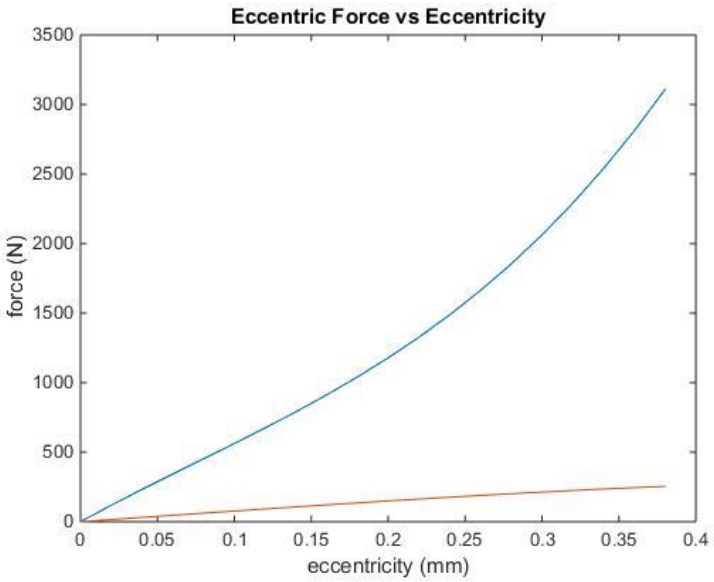

Fig. 64 Curved fitted eccentric force vs eccentricity

The bearing parameters are calculated based on (115). Given system natural frequency f and damping ratio ξ, bearing stiffness k and damping c are obtained. The motor mass is 64.3040 kg.

$$\begin{cases} \omega = 2\pi f \\ k = \omega^2 m \\ c = \xi 2m\omega \end{cases} \tag{115}$$

6.5.1 Limit Cycle (Without Mass Unbalance)

In this case, there is no static eccentricity and no mass unbalance. The system natural frequency is 55 Hz and bearing damping ratio is 0.1. The motor spin frequency is 977 rpm (16.28 Hz). The x and y direction motion at steady state are shown in Fig. 65. The system undergoes a whirling motion. The whirling frequency is about 27.45 Hz (super harmonic) based on the FFT. The maximum x and y direction motion are about 0.056 mm. The whirling orbit and whirling frequency does not change with spin speed. A set of similar orbit can be obtained as the damping ratio changes as Fig. 66. The larger the damping ratio, the smaller the orbit radius.

This is a limit cycle. By inspection, the slope of the unstable force – tangential eccentric force – decreases with eccentricity (Fig. 67). At small motion, the tangential eccentric force tends to make the whirling motion bigger. However, as the whirling motion gets bigger, the force due to the bearing damping dominants and tends to stabilize the system.

This limit cycle can also happen with a bigger bearing damping ratio. In Fig. 68, the bearing damping ratio is 0.2 and the system natural frequency is 50 Hz. In this case, the whirling frequency is about 16 Hz and does not change with spin speed.

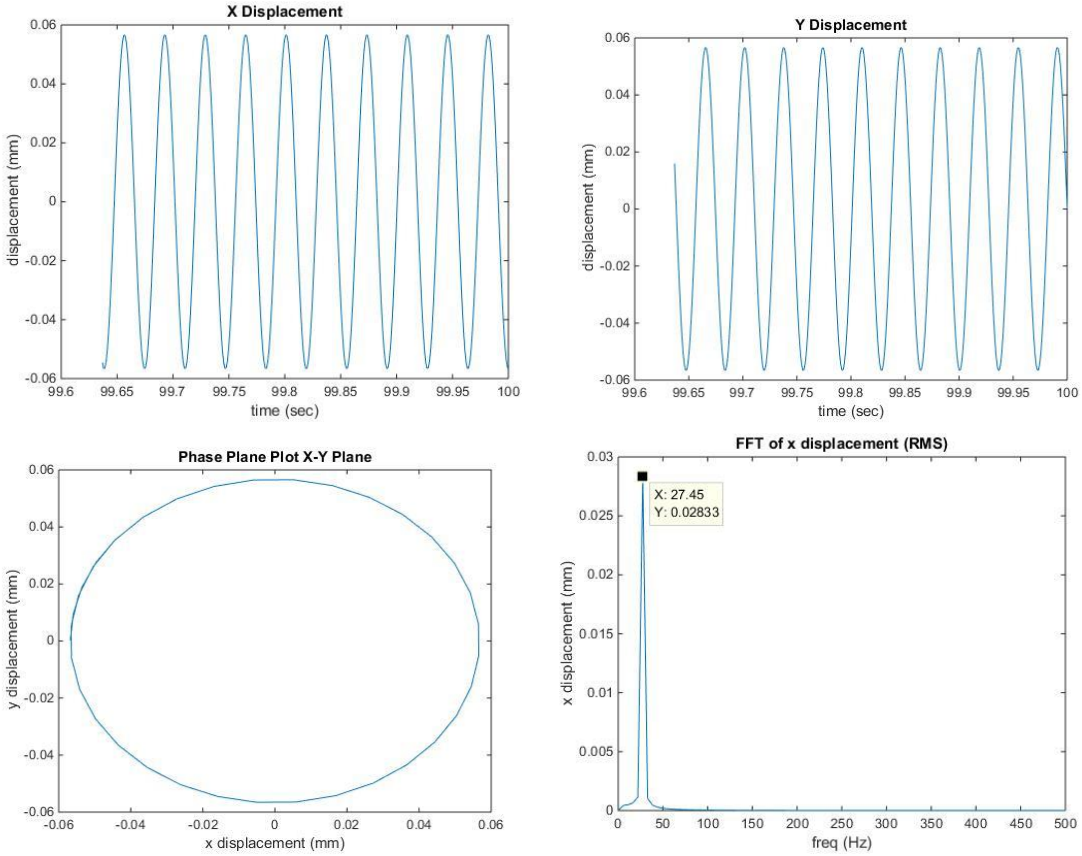

Fig. 65 Limit cycle with natural frequency 55 Hz and bearing damping ratio 0.1

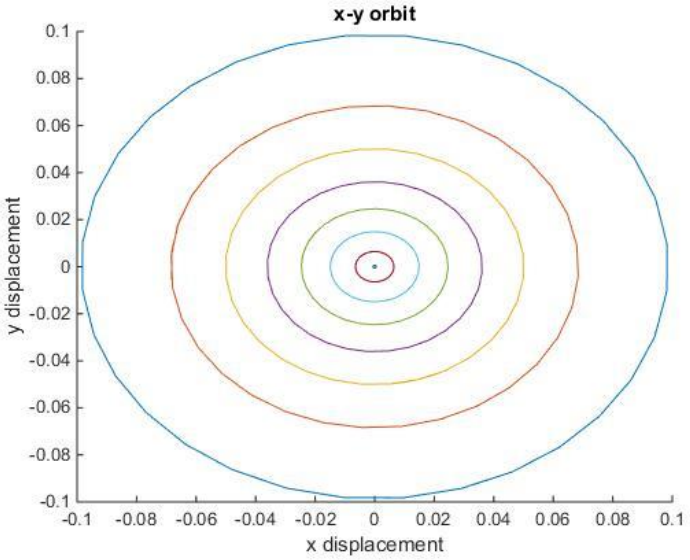

Fig. 66 Limit cycle with natural frequency 55 Hz and varied bearing damping ratio

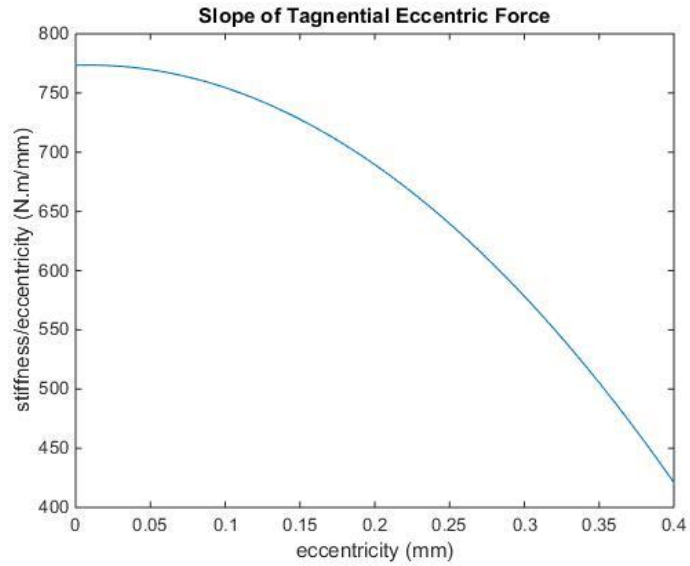

Fig. 67 Slope of tangential eccentric force

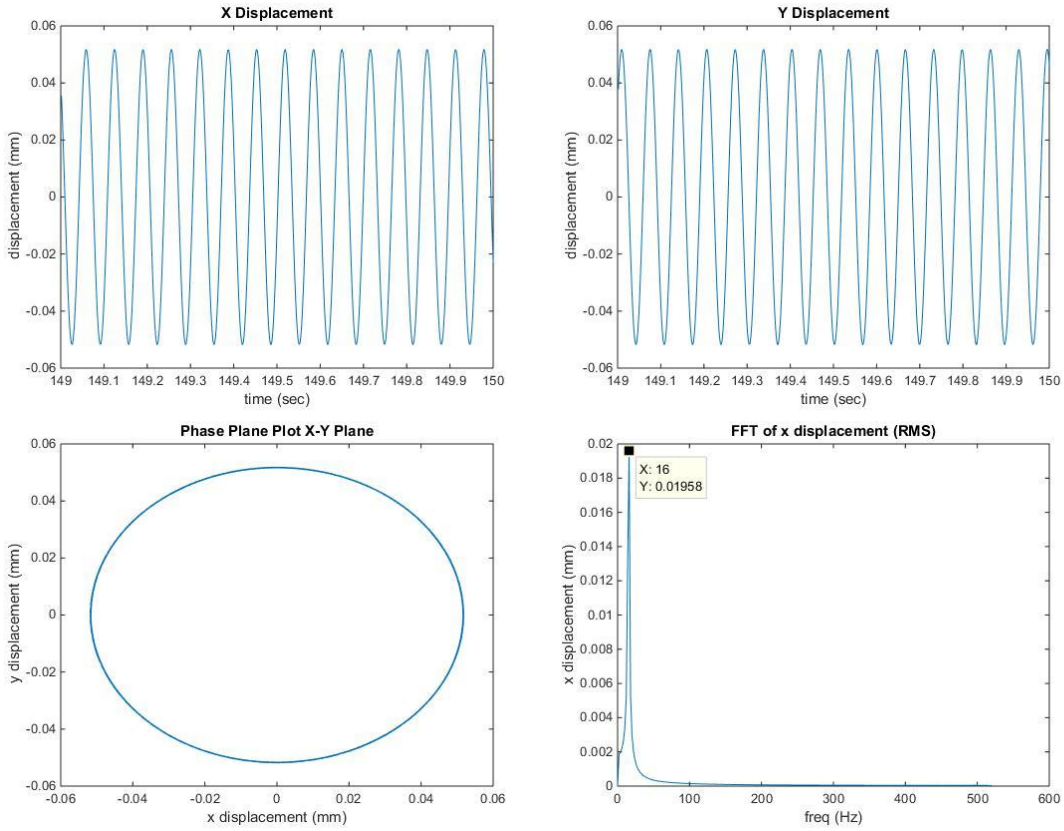

Fig. 68 Limit cycle with natural frequency 50 Hz and bearing damping ratio 0.2

6.5.2 Bounded Limit Cycle (With Mass Unbalance)

In this case, the system natural frequency and damping ratio are kept as 55 Hz and 0.1. And 0.01 mm mass unbalance is added. The motor spin speed is 977 rpm. The rotor whirling orbit has a bounded pattern, as shown in Fig. 69. The FFT of x direction displacement shows two peaks. One is 27.48 Hz. The other is 16.49 Hz, which is quite near the spin frequency (16.28 Hz). The harmonics at 27.48 Hz is quite closed to the 27.45 Hz whirling frequency (Fig. 65) with no mass unbalance. Thus, the motion in this

case can be seen as the combination of the synchronous whirling due to mass unbalance and the whirling due to eccentricity.

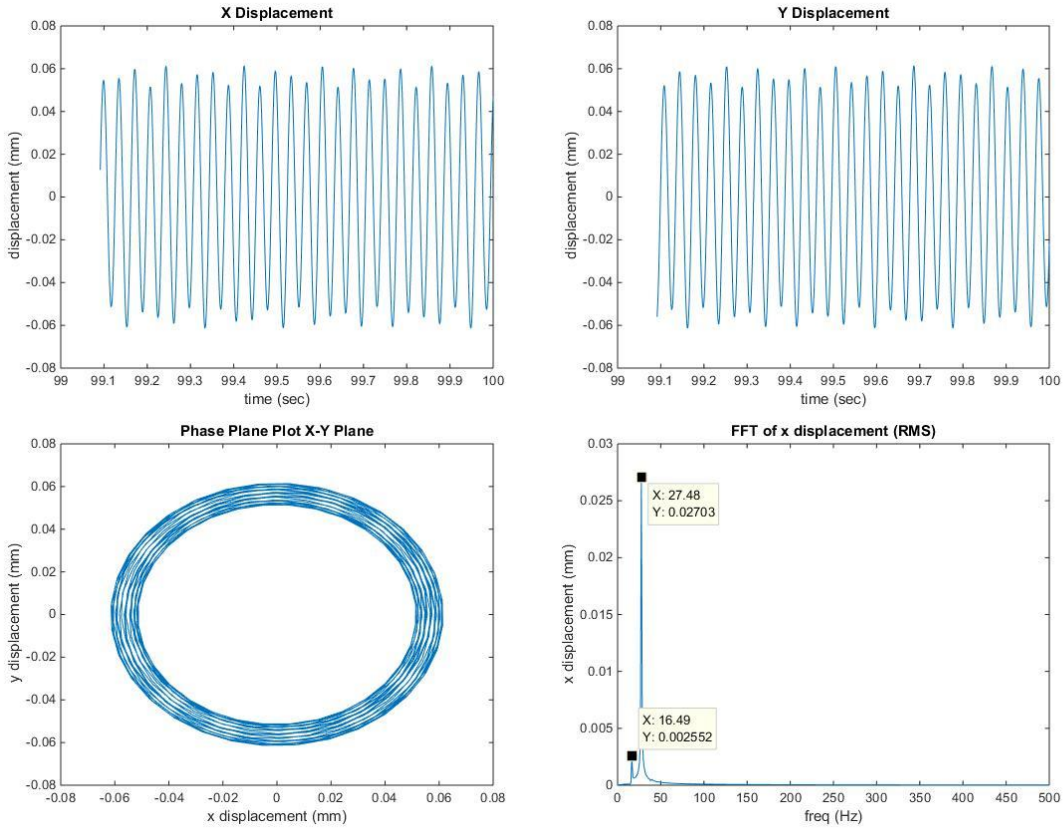

Fig. 69 Bounded limit cycle with natural frequency 55 Hz, bearing damping ratio 0.1 and 0.01 mm mass unbalance

6.5.3 Jumping Phenomena

In this case, the motor spin frequency increases slowly with time with a rate of 1 *rad/s/s.*

$$\omega = k_\omega t\,, \quad k_\omega = 1\ rad/s/s$$

The system natural frequency and damping ratio are kept as 55 Hz and 0.1. And there is 0.01 mm mass unbalance. The simulation results are shown in Fig. 70. The jumping phenomena is observed around 90 sec.

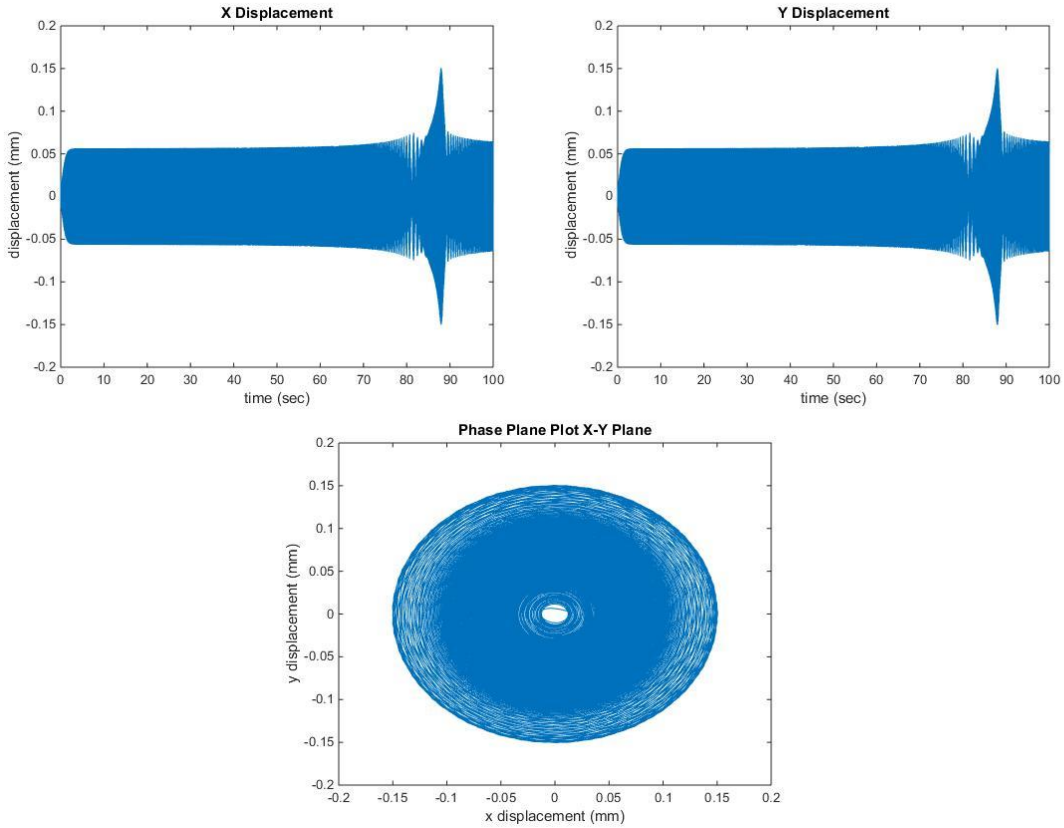

Fig. 70 Jumping phenomena with natural frequency 55 Hz, bearing damping ratio 0.1 and 0.01 mm mass unbalance

With bigger bearing damping ratio, the jumping phenomena can still be observed but the magnitude is compressed. Fig. 71 shows the simulation result with 50 Hz system natural frequency, 0.2 bearing damping ratio and 0.01 mm mass unbalance. The peak

magnitude increases as the mass unbalance increases. Fig. 72 shows the results with 0.03 mm mass unbalance. The jumping phenomena gets more obvious with bigger mass unbalance.

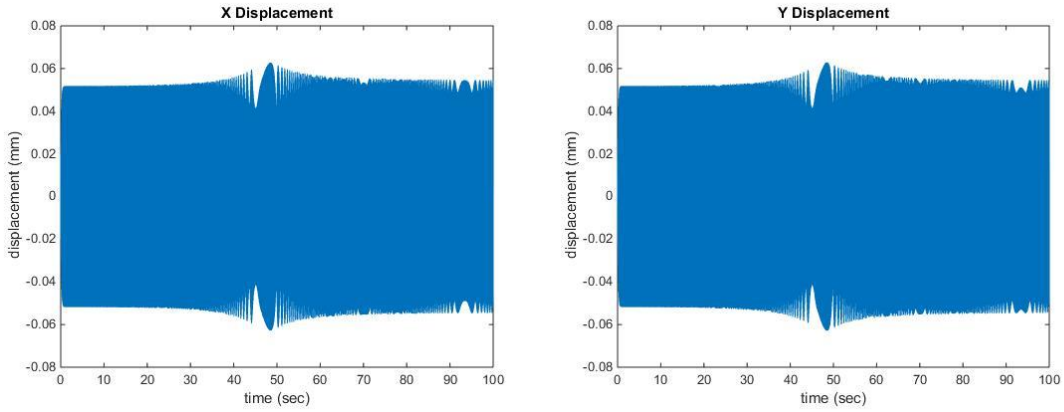

Fig. 71 Jumping phenomena with natural frequency 50 Hz, bearing damping ratio 0.2 and 0.01 mm mass unbalance

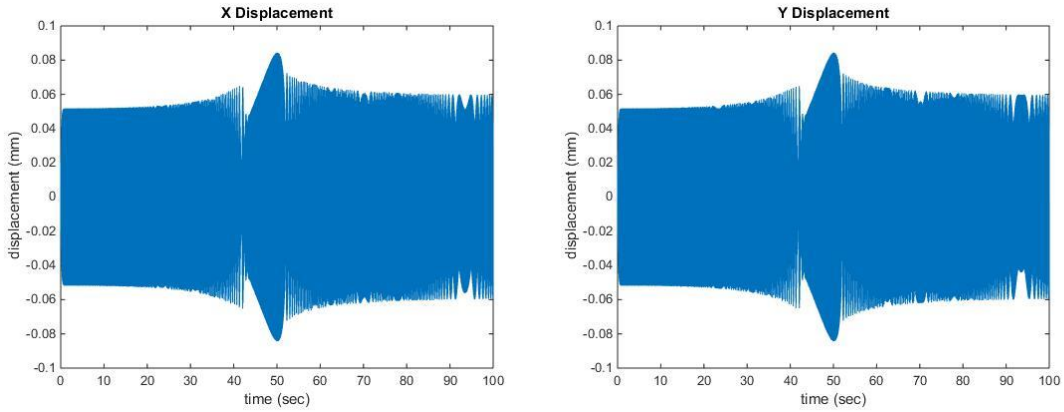

Fig. 72 Jumping phenomena with natural frequency 50 Hz, bearing damping ratio 0.2 and 0.03 mm mass unbalance

CHAPTER VII

CONCLUSIONS AND FUTURE WORK*

7.1 Conclusions

7.1.1 VFDs

(a) A systematic approach for evaluating fatigue life of a complex machinery train powered by a VFD motor and undergoing torsional vibration. A realistic model is utilized including detailed power electronics, motor, gears, couplings and shafts components. Life prediction is based on the Rain-flow approach which is applicable to transient startup events and to sustained, steady state cyclic stress related to resonance. Prior approaches in the literature are too restrictive in assuming that all resonances will cause failure, and also do not provide a means to estimate life.

(b) Demonstration that although utilizing higher level inverters will reduce the total harmonic distortion in the motor torque, individual frequency components near to resonance frequencies may actually increase in amplitude and exacerbate resonance with higher inverter levels. Prior approaches provide a misconception that reducing total harmonic distortion is sufficient to lower all individual torque component amplitudes.

(c) Mitigation of damaging resonance conditions that are not alleviated by utilizing a higher level inverter may be accomplished with a PWM carrier frequency

---

* Part of the data reported in this chapter is reprinted with permission from "VFD Machinery Vibration Fatigue Life and Multi-Level Inverter Effect" by Xu Han, Alan Palazzolo, 2013, *IEEE Transactions on Industry Application*, Volume 49, Issue 6, pp. 2562-2575, Copyright [2013] by IEEE.

interleaving on a four-thread VFD as demonstrated in [16]. The present paper provides the alternative approaches of slight shifting of f_{pwm} or utilizing a coupling with increased damping.

7.1.2 Motor Eccentricity

In this dissertation, the motor is modeled with MEC method, which provides access to both the radial and tangential air gap fluxes. This provides ways to calculate the radial and tangential eccentric forces based on Maxwell stress tensor. The MEC model is also coupled with the motor electric circuit model for whole motor model, which is capable for transient simulation with dynamic eccentricity. This model can be used for different types of motor with series and parallel windings. An induction motor is used as an example to validate the model. By comparing with FEM method (Ansys Maxwell), the proposed model provides a good agreement for both flux density distribution and force calculation.

With the proposed model and example induction motor, a parametric study is performed. The radial and tangential forces are affected by the motor operation condition and eccentricity magnitude. Both of them increase as the eccentricity increases. The radial force increases with the motor supplied voltage/current with a decreased slop. However, the tangential force increases with the supplied voltage/current first and decreases as the motor gets more saturation. Also a motor with a smaller designed air gap tends to have larger eccentric forces with same eccentricity.

The radial and tangential eccentric forces are equivalent to negative stiffnesses in mechanical system. A simple Jeffcott rotor model is used to study the influence of eccentric forces on stability. An analytical criteria of the bearing damping is provided for the system to be stable. Besides the stability problem, the nonlinearity of the motor eccentric forces can also induce nonlinear motion in mechanical system. Limit cycles are obtained with motor eccentric forces even with 0.2 bearing damping ratio. When the mass unbalance is included, a bounded type whirling orbit was observed. Also jumping phenomena is observed by varying the spin speed with time.

7.2 Future Work

7.2.1 VFDs

Areas of future work include: (1) Increasing the fidelity of the modeling components, such as including the dead time voltage due to switching mentioned in [5] and closed-loop drive; (2) Improving the mechanical model with torsional-lateral motion coupling; (3) Correlation of predictions and experimental verification; (4) Modeling entire machinery train with the four-thread VFD as mentioned in [19] to eliminate certain selected torque components in torque spectrum.

7.2.2 Motor Eccentricity

In real practice, a machinery train is complex and can go under both static and dynamic lateral motion. To predict the both torsional and lateral vibration, a coupled torsional and lateral simulation should be performed. Thus, the eccentric motor force

model illustrated in this paper will be combined with a complex machinery train with coupled torsional and lateral motion. The effects of the eccentric motor forces on the system torsional vibration and resonance will be studied.

REFERENCES

[1] T. Feese and R. Maxfield, Torsional Vibration Problem with Motor/ID Fan System Due to PWM Variable Frequency Drive, *37th Turbomachinery Symposium*, 2008, Houston, TX.

[2] J. J. A. Kocur and J. P. Corcoran, VFD Induced Coupling Failure, *37th Turbomachinery Symposium* , 2008, Houston, TX.

[3] A. Arkkio, Unbalanced Magnetic Pull in Cage Induction Motors with Asymmetry in Rotor Structures, *International Conference of Electric Machines*, IET, Sep 1996, Cambridge, U.K..

[4] L. Lundstrom, R. Gustavsson, J.-O. Aidanpaa, N. Dahlback and M. Leijon, Influence on the stability of generator rotors due to radial and tangential magnetic pull force, *IET Electr. Power Appl*., Vol. 1, No. 1, Jan 2007.

[5] J. Wachel and F. Szenasi, Analysis of Torsional Vibrations in Rotating Mahinery, *22nd Turbomachinery Symposium*, 1993, Houston, TX.

[6] S. Y. Jung, A torsional vibration analysis of synchronous motor driven trains by the modal method, Ph.D. Dissertation, Texas A&M University, Aug 1986.

[7] G. L. Godwin, E. F. Merrill, Oscillatory Torques During Synchronous Motor Starting, Transactions of Industry and General Applications, IEEE *Trans. Industry Applications*, Vol. IGA-6 Issue 3, pp. 258 – 265, May 1970.

[8] E.D. Goodman, T. H. Barton, Startup Torques in Synchronous Motor Drives, *IEEE Trans. Industry Applications*, Vol. IA-14, No. 3 , pp.193-198, May/Jun 1978.

[9] D.G. Holmes, A General Analysis Method for Determining the Theoretical Harmonic Components of Carrier Based PWM Strategies, *IEEE Conf. Industry Applications*, Oct 1998, St. Louis, MO.

[10] J. Plotkin, U. Schaefer, R. Hanitsch, Torque Ripple in PWM-VSI-fed drives due to Parasitic Effects in the Inverter Control, *IEEE Conf. Industrial Electronics*, Nov 2009, Porto, Portugal.

[11] D. J. Sheppard, Torsonal Vibration Resulting from Adjustable-Frequency AC Drives, *IEEE Trans. Industry Applications*, Vol. 24, No.5, Sep/Oct 1988.

[12] J. C. Wachel, F. R. Szenasi, Analysis of Torsional Vibrations in Rotating Machinery, *Proc. 22nd Turbomach. Symp.*, pp. 127-151, 1993, Houston, TX.

[13] B. Howes, Perplexing Variable Frequency Drive Vibration Problems, Beta Machinery Analysis Ltd., Calgary, AB, Canada, 2004.

[14] L. De la Roche, B. Howes, Lateral and Torsional Vibration Problems in Systems Equipped with Variable Frequency Drives, Beta Machinery Analysis Ltd., Calgary, AB, Canada, 2005.

[15] R. J. Kerkman, J. Theisen, K. Shah, PWM Inverters Producing Torsional Components in AC Motors, *IEEE 55th PCIC.*, 2008, Cincinnati, OH.

[16] M. Tsukakoshi, M. AI Mamun, K. Hashimuar, H. Hosoda, J. Sakaguchi, L. Ben-Brahim, Novel Torque Ripple Minimization Control for 25MW Variable Speed Drive System Fed by Multilevel Voltage Source Inverter, *Proc. 39th Turbomach. Symp.*, 2010, Houston, TX.

[17] M. Ashari, Practical Implementation of Multilevel Inverter for Reducing Current

on an Induction Motor Bearing, *4th Saudi technical Conference and Exhibition*, Dec 2007, Riyadh, Saudi Arabia.

[18] S. Khomfoi, L. M. Tolbert**,** *Power Electronics Handbook*, 2nd Edition, Chapter 17, Elsevier, 2007, Burlington, MA.

[19] J. Song-Manguelle, S. Schröder, T. Geyer, G. Ekemb, J. Nyobe-Yome, "Prediction of Mechanical Shaft Failures Due to Pulsating Torques of Variable-Frequency Drives", *IEEE Trans. Industry Applications*, Vol. 46, No. 5, Sep/Oct 2010.

[20] R. Belmans, A. Vandenput and W. Geysen, Calculation of the flux density and the unbalanced pull in two pole induction machines, *Electrical Engineering*, Volume 70, Issue 3, pp 151-161, Springer, 1987.

[21] D. Guo, F. Chu and D. Chen, The unbalanced magnetic pull and its effects on vibration in a three-phase generator with eccentric rotor, *Journal of Sound and Vibration*, Volume 254, Issue 2, Pages 297–312, Jul 2002.

[22] P. Pennacchi, Computational model for calculating the dynamical behavior of generators caused by unbalanced magnetic pull and experimental validation, *Journal of Sound and Vibration*, Volume 312, Issues 1–2, Pages 332–353, 2008.

[23] L. Frosini and P. Pennacchi, Analysis of unbalanced magnetic pull calculation in generators with two pole pairs, *Proceedings of IDETC/CIE 2009*, ASME, Aug/Sep, 2009, San Diego, CA.

[24] B. Wu, W. Sun, Z. Li and Z. Li, Circular whirling and stability due to unbalanced

magnetic pull and eccentric force, *Journal of Sound and Vibration*, Volume 330, Issue 21, Pages 4949–4954, Oct 2011.

[25] H. Im, H.Yoo and J. Chung, Dynamic analysis of a BLDC motor with mechanical and electromagnetic interaction due to air gap variation, *Journal of Sound and Vibration*, Volume 330, Issue 8, Pages 1680–1691, April 2011.

[26] D. Dorrell, *Calculation of unbalanced magnetic pull in cage induction machines*, Ph.D dissertation, 1993, University of Cambridge.

[27] A. Smith and D. Dorrell, Calculation and measurement of unbalanced magnetic pull in cage induction motors with eccentric rotors. Part 1: Analytical model, *IEE Proc.-Electr. Power Appl*., Vol. 143, No. 3, May 1996.

[28] D. Dorrell and A. Smith, Calculation and measurement of unbalanced magnetic pull in cage induction motors with eccentric rotors. Part 2: Experimental investigation, *IEE Proc.-Electr. Power Appl*., Vol. 143, No. 3, May 1996.

[29] N. Al-Nuaim and H. Toliyat, A novel method for modeling dynamic air-gap eccentricity in synchronous machines based on modified winding function theory, *IEEE Transactions on Energy Conversion*, Vol. 13, No. 2, Jun 1998.

[30] R. Stoll, Simple computational model for calculating the unbalanced magnetic pull on a two-pole turbogenerator rotor due to eccentricity, IEE Proc.-Electr. Power Appl., Vol. 144, No. 4, May 1997.

[31] S. Swann, Effect of rotor eccentricity on the magnetic pull in the air-gap of a non-salient-pole machine, *Proc. IEE*, 1963, 110, (5), PP. 903-915.

[32] L. Chen and W. Hofmann, Analysis of radial forces based on rotor eccentricity of bearingless switched reluctance motors, *XIX International Conference on Electrical Machines – ICEM 2010,* 2010, Rome.

[33] A. Belahcen, A. Arkkio, P. Klinge, J. Linjama, V. Voutilainen and J. Westerlund, Radial forces calculation in a synchronous generator for noise analysis, *Proc.3rd Chinese International Conference on Electrical Machines*, , pp 199-122, Aug 29-31, 1999, Xi'an, China.

[34] A. Tenhunen, T. Benedetti, T. Holopainen and A. Arkkio, Electromagnetic forces in cage induction motors with rotor eccentricity, *Proc. IEMDC'03*, Vol. 3, pp 1616-1622, Jun 2003, Madison, WI.

[35] P. Rodriguez, A. Belahcen, A. Arkkio, A. Laiho and J. Antonino-Daviu, Air-gap force distribution and vibration pattern of induction motors under dynamic eccentricity, *Electrical Engineering*, Volume 90, Issue 3, pp 209-218, Feb 2008.

[36] Y. Wang, G. Sun and L. Huang, Magnetic field-induction nonlinear vibration of an unbalanced rotor, *Proc. IMECE'03*, ASME, Nov. 15-21, 2003, Washington, D.C..

[37] R. Gusstavsson and J.-O. Aidanpaa, The influence of nonlinear magnetic pull on hydropower generator rotors, *Journal of Sound and Vibration,* Volume 297, Issues 3–5, Pages 551–562, Nov 2006.

[38] Y. Calleecharan and J.-O. Aidanpaa, Dynamics of a hydropower generator subjected to unbalanced magnetic pull, *Proc. IMechE Vol. 225 Part C: J.*

Mechanical Engineering Science, 2011.

[39] J. Jeong, E. Lee and H. Cho, Analysis of transient state of the squirrel cage induction motor by using magnetic equivalent circuit method, *ICEMS 2003*, IEEE, Vol. 2, pp 720-723, Nov. 9-11, 2003, Beijing, China.

[40] S. Sudhoff, B. Kuhn, K. Corzine and B. Branecky, Magnetic equivalent circuit modeling of induction motors, *IEEE Trans. Energy Conversion*, Vol. 22, No. 2, Jun 2007.

[41] M. Zhang, A. Macdonald, K. Tseng and G. Burt, Magnetic equivalent circuit modeling for interior permanent magnet synchronous machine under eccentricity fault, *2013 48th UPEC*, IEEE, Sep. 2-5, 2013, Dublin.

[42] A. Tariq, C. Nino-Baron and E. Strangas, Iron and magnet losses and torque calculation of interior permanent magnet synchronous machines using magnetic equivalent circuit, *IEEE Trans.Magnetics*, Vol. 46, No. 12, Dec 2010.

[43] B. Sheikh-Ghalavand, S. Vaez-Zadeh and A. Isfahani, An improved magnetic equivalent circuit model for iron-core linear permanent-magnet synchronous motors, *IEEE Trans.Magnetics*, Vol. 46, No. 1, Jan 2010.

[44] H. Cho, J. Yu, S. Jang, C. Kim, J. Lee and H. Han, Equivalent magnetic circuit based levitation force computation of controlled permanent magnet levitation system, *IEEE Trans.Magnetics*, Vol. 48, No. 11, Nov 2012.

[45] X. Lu, K. Iyer, K. Mukherjee and N. Kar, Development of a novel magnetic circuit model of design of premium efficiency three-phase line start permanent magnet machines with improved starting performance, *IEEE Trans.Magnetics*,

Vol. 49, No. 7, Jul 2013.

[46] H. Gorginpour, H. Oraee and R. McMahon, A novel modeling approach for design studies of brushless doubly fed induction generator based on magnetic equivalent circuit, *IEEE Trans.Energy Conversion,* Vol. 28, No. 4, Dec 2013.

[47] M. Yilmaz and P. Krein, Capabilities of finite element analysis and magnetic equivalent circuits for electrical machine analysis and design, *2008 PESC, IEEE,* Jun 15-19, 2008, Rhodes, Greek.

[48] G. Sizov, C. Yeh and N. Demerdash, Magnetic equivalent circuit modeling of induction machines under stator and rotor fault conditions, *IEMDC'09*, IEEE, May 03-06, 2009, Miami, FL.

[49] L. Vandevelde and J. Melkebeek, Numerical analysis of vibrations of squirrel-cage induction motors based on magnetic equivalent circuits and structural finite element models, *Industry Application Conference,2001. 36th IAS Annual Meeting, Conference Record of the 2001 IEEE,* Sep 30- Oct. 4, 2001, Chicago, IL.

[50] H. Kelk, A. Eghbali and H. Toliyat, Modeling and analysis of cage induction motors under rotor misalignment and air gap eccentricity, *Industry Applications Conference, 2005. 40th IAS Annual Meeting. Conference Record of the 2005,* Vol.2, pp 1324-1328, Oct 2-6, 2005.

[51] V. Ostovic, *Dynamics of saturated electric machines*, 1989, Springer-Verlag, New York.

[52] J. Perho, *Reluctance network for analyzing induction machines*, Ph.D dissertation, 2002, Helsinki University of Technology.

[53] M. Amrhein, *Induction machine performance improvements – design-oriented approaches*, Ph.D dissertation, 2007, University of Illinois at Urbana-Champaign.

[54] D.W. Novotny, T.A. Lipo, *Vector Control and Dynamics of AC Drives*, 1997, Oxford, New York.

[55] W. J. Chen, E. J. Gunter, *Introduction to Dynamics of Rotor-Bearing Systems*, pp.367 – 398, 2005, Trafford Publishing, Bloomington, IN.

[56] S. Wang, "Mean Shear Stress Effect for a Notch-Free Ductile Material Under Pure Cyclic Torsional Loads", *ASME J. Pressure Vessel Technology*, Vol. 128, pp. 667-669, Nov 2006.

[57] R. G. Budynas, J. K, Nisbett, *Shigley's Mechanical Engineering Design*, 8th Edition, 2008, McGraw-Hill Higher Education, New York, NY.

[58] S. Ariduru, Fatigue Life Calculation by Rainflow Cycle Counting Method , Master Thesis, Texas A&M University, 2004.

[59] Standard Practices for Cycle Counting in Fatigue Analysis, ASTM, 2011.

[60] I. J. Garshelis, R. J. Kari, S. Bitar, Magnetic Means for Determining Torsional Yield Strength, *IEEE Trans. Magnetics*, Vol. 39, No. 5, Sep 2003.

[61] K. Lee, S. F, P.K.Sen, L.G.Polese, M.Alahmad and C.Waters, Estimation of Induction Motor Equivalent Circuit Parameters from Nameplate Data, *North American Power Symposiuym (NAPS), IEEE*, 2012.

[62] MathWorks, *fsolve*-solve system of nonlinear equations, 2015. URL: http://www.mathworks.com/help/optim/ug/fsolve.html.